Mineral deposition and maturation during bone development

Dissertation

To obtain the academic degree

Doctor rerum naturalium (Dr. rer. nat.)

Submitted to the Department of Biology, Chemistry and Pharmacy

of Freie Universität Berlin

by

Claudia Lange

Max Planck Institute of Colloids and Interfaces,

Department of Biomaterials, Potsdam

January 2011

This thesis was prepared from November 2007 to January 2011 at the Max Planck Institute of Colloids and Interfaces, in the Department of Biomaterials, under supervision of Prof. Dr. Peter Fratzl and Prof. Dr. Petra Knaus.

1st Reviewer: Prof. Dr. Peter Fratzl

2nd Reviewer: Prof. Dr. Petra Knaus

Date of defense: 14th April 2011

Abstract

Biomineralization in invertebrates and vertebrates has been intensively investigated over the last decades. One biomineralization strategy often discussed today is mineralization via transient precursor phases. In vertebrate mineralized tissues, the possible formation of an amorphous precursor mineral phase is still an unresolved question. Recent studies suggest the existence of amorphous calcium phosphate (ACP) as the first formed mineral in developing enamel of mice or in zebrafish fin. Whereas the mineralization in zebrafish fin progresses linearly, the mineralization process in mammalian bone is more complex and only little is known about early phases during this process. This motivated us to investigate developing bone in mammals using different techniques such as synchrotron X-ray diffraction experiments and electron microscopy.

In the present doctoral thesis, developing bone in murine long bones has been investigated, especially at the early stages of bone formation. Normal mice were compared to knockout mice with neurofibromatosis type 1 (NF1) based on the same strain, C57BL/6. Furthermore, the development of bone within tissue engineering scaffolds in a pig model has been analyzed. Mineral particle thickness and arrangement were characterized in developing bone by small-angle X-ray scattering (SAXS) combined with wide-angle X-ray diffraction (WAXD), providing mineral length and the amount of hydroxyapatite (HA), as well as X-ray fluorescence (XRF) analysis, revealing the calcium content.

During bone development, SAXS revealed a complete lack of mineral particle orientation at the fetal stages, whereas one day after birth the mineral particles were predominantly aligned parallel to the longitudinal axis of the bone. Strong differences were found in size and orientation of the mineral particles between fetal and postnatal bone, with bulkier (thicker, shorter) and randomly oriented particles at the fetal stage, and highly aligned and much longer crystals after birth. This could indicate the existence of two different types of bone tissue appearing successively during bone growth and coexisting in mature bone.

The inherited disorder NF1 results in a bone and cartilage phenotype, but there were no significant differences in the mineral properties detectable by SAXS between NF1 and normal bone. However, subsequent investigations on the microstructure clearly displayed morphological differences of the osteocyte lacunae: NF1 bone revealed osteocyte lacunae less uniform, frayed and bigger than in normal bone. These results suggest that the osteocytes may be involved in the bone defect in NF1 mice.

Bone development induced by resorbable scaffolds, implanted in a critical sized defect in the porcine calvaria appeared to be quit different. SAXS revealed huge structural differences between tissue engineered bone and the native calvaria. Whereas mineral

particles around cavities in the calvaria showed no preferential orientation, in the tissue engineered bone they were strongly oriented around the struts of the scaffold which seem to guide the bone formation. These results demonstrate that the implanted scaffolds led to long-term regeneration and remodeling of highly organized bone.

In summary, it was shown that during bone growth the formation of highly ordered tissue follows the initial development of a less ordered bony substrate, while it forms directly in a tissue engineered scaffold.

Kurzfassung

Biomineralisation in Invertebraten und Vertebraten wurde in den letzten Jahrzehnten intensiv untersucht. Eine häufig diskutierte Strategie der Biomineralisation ist die Mineralisation ausgehend von einer kurzlebigen Vorläufer-Mineralphase. Für mineralisierte Gewebe in Vertebraten ist die mögliche Bildung einer amorphen Mineral-Vorstufe noch immer eine ungeklärte Frage. Neueste Arbeiten deuten auf die Existenz von amorphem Kalzium Phosphat (ACP) als initial gebildete Mineralphase in der frühen Phase der Bildung von Zahnschmelz in Mäusen oder in Zebrafisch-Flossen hin. Während die Mineralisation in Zebrafisch-Flossen linear verläuft, ist der Mineralisationsprozess im Säugetier-Knochen wesentlich komplizierter und es ist nur wenig zu den frühen Phasen dieses Prozesses bekannt. Dies motivierte uns, die Knochenbildung in Säugetieren mit Hilfe verschiedener Methoden, wie Synchrotron-Röntgen-Experimenten und Elektronenmikroskopie, zu untersuchen.

In der vorliegenden Doktorarbeit wurde die Bildung von Röhrenknochen in Mäusen untersucht, mit besonderem Interesse an den frühen Phasen der Knochenbildung. Wildtyp Mäuse wurden verglichen mit genetisch veränderten Mäusen mit Neurofibromatose Typ 1 (NF1), welche auf dem gleichen Stamm, C57BL/6, basieren. Außerdem wurde die Knochenbildung in „Tissue Engineering“ Konstrukten in der Calvaria von Schweinen untersucht. Mineralpartikeldicke und deren Anordnung wurden mit Hilfe der Röntgen-Kleinwinkel-Streuung (SAXS) charakterisiert, verbunden mit Röntgen-Weitwinkel-Beugung (WAXD) zur Analyse der Mineralpartikellänge und des Gehaltes an Hydroxyapatit (HA), sowie Röntgen-Fluoreszenzanalyse (XRF), zur Bestimmung des Kalzium Gehaltes in der Probe.

Im Verlauf der Knochenbildung zeigte die SAXS Analyse, dass die Mineralpartikel in Knochen der fötalen Stadien der Knochenbildung keine Orientierung aufweisen, wohingegen die Mineralpartikel bereits einen Tag nach der Geburt vorzugsweise parallel zur Längsachse des Knochens ausgerichtet waren. Bemerkenswerte Unterschiede bezüglich Größe und Orientierung der Mineralpartikel zwischen fötalem und postnatalem Knochen wurden aufgezeigt; und zwar dicke, kurze und unorientierte Mineralpartikel im fötalen Knochen und stark orientierte und wesentlich längere Mineralpartikel im postnatalen Knochen. Dies könnte darauf hindeuten, dass es sich um zwei verschiedene Formen von Knochengewebe handelt, welche im Verlauf der Knochenbildung nacheinander auftreten und in entwickeltem Knochen nebeneinander vorliegen.

Bei einer NF1-Erkrankung kommt zur Ausprägung eines Knorpel- und Knochenphänotyps, jedoch zeigten SAXS-Messungen keinen signifikanten Unterschied bezüglich der

Mineralpartikeleigenschaften zwischen NF1- und normalem Knochen. Allerdings zeigten anschließende Untersuchungen der Mikrostruktur morphologische Unterschiede der Osteozytenlakunen. NF1 Knochen wies weniger einheitliche, ausgefranste und größere Osteozytenlakunen auf, als normaler Knochen. Diese Ergebnisse deuten darauf hin, dass die Osteozyten eventuell am Knochendefekt in NF1 Mäusen beteiligt sind.

Die Knochenbildung, induziert durch resorbierbare Konstrukte, implantiert in einen Defekt von kritischer Größe in der Calvaria von Schweinen scheint anders zu verlaufen. SAXS Messungen zeigten deutliche Unterschiede zwischen Knochen, welcher in einem Konstrukt gebildet wurde, und dem nativem Schädelknochen. Während die Mineralpartikel in der Calvaria keine Vorzugsorientierung um Hohlräume (beispielsweise Osteozyten) aufwiesen, waren sie im Konstrukt stark um die Streben des Konstrukts orientiert, welche scheinbar die Knochenbildung leiten. Diese Ergebnisse veranschaulichen, dass implantierte Konstrukte zu Langzeit-Regeneration und Umbau von stark organisiertem Knochengewebe führen.

Zusammenfassend konnte gezeigt werden, dass im Verlauf der Knochenentwicklung die Bildung von hoch organisiertem Knochengewebe auf die Bildung eines wenig geordneten Knochensubstrates folgt, wohingegen in einem Konstrukt direkt hoch geordnetes Knochengewebe gebildet wird.

Contents

Es ist nicht genug zu wissen,
man muss es auch anwenden;
es ist nicht genug zu wollen,
man muss es auch tun.

Johann Wolfgang von Goethe

1 Introduction

Biomineralization describes the process by which living organisms produce minerals forming mineralized tissues. Silicates in algae, carbonates in invertebrates and calcium phosphate in vertebrates are examples for biomineralization [Lowenstam and Weiner, 1989; Mann, 2001; Aichmayer and Fratzl, 2010]. The conception of the first formed mineral during the mineralization process being a transient precursor phase has developed over a long time. Amorphous precursor phases have been detected in different biomineral systems, including ACP in the radular teeth of chitons [Lowenstam and Weiner, 1985] or amorphous calcium carbonate (ACC) in mollusks [Weiss, Tuross et al., 2002]. However, the formation of an amorphous precursor mineral phase as the first formed mineral in vertebrate mineralized tissues is still controversial discussed [Termine and Posner, 1967; Boskey, 1997; Weiner, 2006; Grynpas, 2007]. By using new techniques such as high-resolution transmission electron microscopy (TEM), Raman spectroscopy or synchrotron X-ray diffraction, it could be recently demonstrated that there are indeed amorphous precursor phases formed during the mineralization process in vertebrates. Crane et al. showed by using Raman microspectroscopy that during intramembranous ossification in the cranial suture of a mouse, an octacalcium phosphate (OCP) -like phase builds the first formed mineral prior the transformation into the mature mineral phase, carbonated HA [Crane, Popescu et al., 2006]. The continuously forming fin bony rays of zebrafish describe a simple bone model system in which mineralization is temporally and spatially resolved. An ACP phase could be identified as a possible precursor phase using high resolution TEM, synchrotron microbeam X-ray diffraction and small-angle scattering as well as cryo scanning electron microscopy (SEM) [Mahamid, Sharir et al., 2008; Mahamid, Aichmayer et al., 2010]. Newly formed enamel mineral could be determined as ACP, which subsequently transforms into apatitic crystals using TEM and Fourier transformation infrared spectroscopy (FTIR) [Beniash, Metzler et al., 2009].

Another issue of discussion in the field of biomineralization is the initiation of mineralization. In one hypothesis describing the early stages of mineralization it is assumed that mineralization in tissues of vertebrates is associated with non-crystalline, calcium- and phosphate-containing electron-dense granules. This hypothesis involves that polymers of phosphate ions (polyphosphates $(PO_4^{3-})_n$) are collocated with mineralizing cartilage and resorbing bone [Omelon, Georgiou et al., 2009]. There, polyphosphate formation and hydrolytic degradation constitutes a simple mechanism for phosphate accumulation and enzymatic control of biological apatite saturation. Another hypothesis to explain the intrafibrillar mineralization of collagen in mineralized tissue is the pathway via

polymer-induced liquid precursors (PILP), first proposed by Gower et al. for calcium carbonate formation [Gower and Odom, 2000]. This hypothesis describes the formation of liquid-phase amorphous precursors which are infiltrating the collagen matrix due to capillary action. Recent work of Olszta et al. suggests that the PILP process may also be valid in vertebrate bone and teeth mineralization [Olszta, Cheng et al., 2007].

The mineralization of fish fins progresses linear, easily facilitating the analysis of the mineralization process at different stages of bone development. In contrast, the mineralization process in mammals is very complex, making the analysis of the different developmental stages of mineralization difficult. The gap of knowledge, especially concerning early phases during the mineralization process in mammals, forms the motivation of this thesis to investigate developing bone in mammalian systems. Due to the instability of amorphous precursor phases at the early stages of bone development, as well as the fact that these precursor phases are often coexistent with the crystalline mature phase, different techniques are required to identify them. Thus, the present thesis aims in the analysis of developing bone, in particular the analysis of the early stages of bone development, by applying different techniques to achieve new insights in the mineralization process. Therefore, the mineral formation during (i) bone development of long bones in normal mice, (ii) long bones of genetically modified mice and (iii) the induced bone development in scaffolds during healing are investigated.

(i) The main part of this doctoral thesis comprises the analysis of the mineral formation during natural bone development in mice. Different to human bone, mice bone exhibits no Haversian system. But, the small body size and rapid development of mice are favorable characteristics when designing experimental animal models [Patton and Kaufman, 1995]. Furthermore, there exists the possibility for genetically modifications by knocking out a specific gene, leading to a distinct disease. In this doctoral thesis mice of the strain C57BL/6 are analyzed, a widely used mouse strain in bone research [Brodt, Ellis et al., 1999; Akhter, Fan et al., 2004]. C57BL/6 is therefore very convenient to establish baseline data, for instance comparable with data from genetically modified mice using the same strain [Kolanczyk, Kossler et al., 2007; Kolanczyk, Kuhnisch et al., 2008]. The mineral particle size and orientation of the early mineral phases, especially at fetal stages of bone development, still remains unclear and is thus the motivation of analyzing the structural properties of the mineral particles during bone formation, in particular from fetal to mature bone. There have been studies on postnatal (after birth) bone samples to investigate size and shape of the mineral particles [Grabner, Landis et al., 2001; Roschger, Grabner et al., 2001] or studies on fetal bones but only investigating the thickness of the mineral particles [Fratzl, Fratzl-Zelman et al., 1991] but not the length. However, there are no such studies on a series of samples investigating different mineral properties, such as shape and

arrangement, during bone development at different time points from the fetal to the postnatal state. Furthermore, such data on mineral formation during natural bone development can be used as structural baseline data of mineral particles, helping to better understand the effect of mechanical stimulation due to environmental changes at birth, which might influence the organization and growth of the mineral particles in bone.

(ii) Altered bone formation in genetically modified mice can be influenced on all levels of bone hierarchy. The advantage of having data, determined for a standard mouse strain, as a baseline, is the possibility to compare natural bone development with genetically modified bone development, in particular bones of mice exhibiting neurofibromatosis type 1 (NF1) using the same strain (C57BL/6). NF1 is an inherited disorder caused by one gene, Nf1, encoding for neurofibromin 1. Former studies revealed a specific bone and cartilage phenotype in mice with a knockout of the Nf1 gene, including bowing of the tibia and fusion of joints. It could be demonstrated that neurofibromin 1 plays an essential role in skeletal development and growth, influencing joint formation, osteoblast differentiation and growth plate function [Kolanczyk, Kossler et al., 2007; Kolanczyk, Kuhnisch et al., 2008]. The lowest level of hierarchy in bone, namely the mineral particle properties size and orientation in the collagen/mineral composite, may be influenced by this disease, motivating the analysis of the mineral properties in NF1 bone compared to normal bone. Besides the nanometer scale, the influence of NF1 on the micrometer scale, in particular on the osteocytes, is investigated in this dissertation.

(iii) Artificially induced bone development describes the bone formation induced by resorbable composite scaffolds implanted in the porcine calvaria. For mineral arrangement in flat bones such as the calvaria it is reported that the mineral particles are arranged in plane, but showing no preferential orientation within the plane [Fratzl, Fratzl-Zelman et al., 1991]. Hence, this part of the thesis focuses on how mineral particles are formed and arranged in tissue engineered bone compared to native calvaria. There have been series of *in vitro* and small animal studies, reviewed by Woodruff and Hutmacher [Woodruff and Hutmacher, 2010], but only little is known on long-term *in vivo* studies using a large animal model. This is the motivation to establish a preclinical study to investigate regenerated bone in a critical sized skull defect after a long period of time using a large animal model. Scaffolds composed of a mixture of polycaprolacton (PCL) and tricalcium phosphate (TCP) are implanted for 2 years in a defect area in the porcine calvaria to establish a long-term *in vivo* study on bone regeneration in tissue engineered constructs. The vision of the so-called early pioneers of the field of tissue engineering, Langer and Vacanti, led to the birth of this interdisciplinary field [Langer and Vacanti, 1993]. The fundamental concept underlying tissue engineering is to combine a scaffold with living cells, and/or biologically active molecules to promote the regeneration of tissues. The

scaffold is expected to fulfill various functions such as the support of cell migration, growth and differentiation while being biocompatible and biodegradable [Hutmacher, 2000]. It is very important to control and understand the degradation process of a scaffold to lead to successful tissue formation, remodeling, and maturation of the tissue. The bone formation in three-dimensional (3D) composite scaffolds with and without bone marrow stem cells (BMSCs) are investigated concerning the structural properties of mineral particles in the regenerated bone tissue and compared to native bone.

To understand the mineral formation process and to investigate the structural organization of mineral particles in bone at different length scales, specific non-destructive methods are used. Optical microscopy and histology enable the analysis of the tissue level during bone development, whereas environmental scanning electron microscopy (ESEM) in backscattered electron (BSE) mode depicts the mineral density distribution. Both approaches reveal information on the micrometer scale. The main technique of this study is scanning small-angle X-ray scattering (sSAXS). When structures within a hierarchical architecture such as bone are exposed to X-rays, they give specific scattering and diffraction patterns revealing structural information [Roschger, Grabner et al., 2001]. Thus, SAXS provides quantitative information about the crystal thickness and orientation, for detecting local structural changes in bone material during bone development. sSAXS includes information on the nanometer scale of the bone hierarchy. Furthermore, synchrotron measurements of SAXS and wide-angle X-ray diffraction (WAXD) at the μ-Spot beam line at BESSY II are performed. Due to the small beam size of 30 μm, resulting in a higher resolution, this beam line is a dedicated facility to measure very low amounts of mineral as in fetal bone. Additional parameters such as the mineral particle length, the amount of HA and the calcium content can be determined at distinct positions in the developing bone. The possibility to simultaneously measure SAXS, WAXD and the X-ray fluorescence (XRF) of calcium, which enables the direct correlation of different data at a distinct position in the sample, describes a very new approach, facilitating new insights in the mineralization process.

In summary, there are three main objectives of the work reported in the present thesis.

(1) The main aim of this study is to analyze and understand the mineral formation and growth during fetal bone development and with age, since only little is known about early mineral particle deposition and maturation in bone from fetal to mature stages of developing bone in mammalian systems.

(2) Furthermore, this dissertation aims in the analysis of bone development in NF1 mice compared to normal bone, since the hierarchical level of influence of NF1 remains unclear.

(3) Additionally, the present doctoral thesis focuses on the development of tissue engineered bone during healing, formed in resorbable composite scaffolds implanted in porcine calvaria compared to native calvaria, to understand the bone remodeling and regeneration guided by a tissue engineered construct.

2 State of the art

The following chapter provides a literature overview about what is known and what is still unknown in the different fields of bone studies, as natural bone development, different aspects and theories concerning biomineralization, especially in vertebrates, the effects of genetically modifications on bone development and tissue engineering. Furthermore, the theoretical background concerning X-ray characterization of bone is described, as this is the main technique of the presented study.

2.1 Natural bone development

The chapter natural bone development describes the "normal" bone development of the skeleton of vertebrates, including information on the composition and structure (see chapter 2.1.1), formation (see chapter 2.1.2) and remodeling of bone (see chapter 2.1.3).

Bone is a specialized connective tissue which forms the skeleton of all vertebrates. Bone tissue is essentially composed of three major components, collagen fibrils, mineral particles, in particular carbonated hydoxyapatite (HA), and water. The basic building block of bone is the mineralized collagen fibril [Rho, Kuhn-Spearing et al., 1998; Weiner and Wagner, 1998; Fratzl, Gupta et al., 2004]. The major functions of bones are: providing mechanical stability, protecting the inner organs and the bone marrow, and forming attachment points for muscles, thus enabling movement of the muscoskeletal system [Baron, 1993]. Furthermore, bone tissue is involved in the mineral homeostasis serving as a reservoir for calcium and phosphate ions, thus having a metabolic function [Baron, 1993], releasing these ions according to the physiological needs of the body [Cashman, 2002]. Additionally, the bone matrix contains many growth factors and cytokines that are released locally and systemically during the process of bone resorption. Moreover, the red marrow in the cavities of bones acts as a formation site for blood and immune cells. Despite its compact structure, bone is a dynamic tissue, which is characterized by continuous bone formation and resorption, called bone remodeling. Bone remodeling is a coupled process between the resorption of old bone and the formation of new bone [Hill, 1998] (see chapter 2.1.3 Bone remodeling).

2.1.1 Bone composition and structure

By weight bone tissue consists of approximately 70% mineral or inorganic matrix, 22-25% organic matrix and 5-8% water. The mineral is built up of calcium phosphate, in vertebrate bones particularly carbonated HA. The organic matrix of bone consists of collagen and a series of non-collagenous proteins (NCPs), such as osteocalcin (OCN), osteopontin (OPN) and alkaline phosphatase (ALP). Around 85-90% of the total bone protein consist of collagen fibrils [Termine and Robey, 1996].

In the following the hierarchical structure of bone ordered from the molecular level to the macroscopic level of hierarchy is described in detail. On the molecular level the essential components collagen, mineral and water are specified. On the microscopic level the bone cells and the structural organization of collagen in fibril patterns is explained and on the macroscopic level differences in bone types and shapes are described.

The organic matrix of bone is mainly built up of collagen, namely collagen type I. The repetitive nature of the amino acid sequences of collagen, which consists of –(Gly-X-Y)n– where X and Y are frequently proline and hydroxyproline residues, allows the protein to assemble into triple helical structures referred to as tropocollagen molecules. The tropocollagen molecules of collagen type I consist of one α2 and two α1 chains. Secondary bonding interactions between tropocollagen units in the extracellular area lead to self-organization of the triple helical proteins into fibrillar structures [Hodge and Petruska, 1963; Orgel, Irving et al., 2006; Olszta, Cheng et al., 2007]. A triple helical collagen molecule is about 300 nm in length and about 1.5 nm in width [Fratzl, 2008]. The collagen type I molecules building up the collagen fibrils in bone are staggered from each other along the axial direction [Miller, 1984; Hodge, 1989; Weiner and Wagner, 1998] by about 64-67 nm, depending on the state of hydration and mineralization [Bonar, Lees et al., 1985; Price, Lees et al., 1997], thus generating a characteristic pattern of gap-zones and overlap-zones within the fibril. The ends of the collagen molecules are separated by holes of about 35 nm in wet unmineralized collagen fibrils and about 20 nm in wet mineralized collagen. These holes are called gap-zones and supposed to be the nucleation sites for the mineralization [Landis, Song et al., 1993; Landis, 1995]. However, recent work of Nudelman et al. suggests that positive charges at the end of the collagen molecules form nucleation sites for mineralization, present in both gap- and overlap-zones [Nudelman, Pieterse et al., 2010]. Collagen fibrils almost never exist alone in biological tissues. They associate with each other to form arrays of aligned fibrils that make up a larger structure called the fiber [Weiner and Wagner, 1998]. Collagen is mainly in charge of the elasticity of bone.

The mineral particles in bone are built up of calcium phosphate, existent as carbonated apatite ($Ca_5(PO_4,CO_3)_3(OH)$) in vertebrates [Weiner and Wagner, 1998]. The Mineral particles in bone are plate shaped crystals of carbonated HA [Weiner and Traub, 1986; Landis, Hodgens et al., 1996], which are embedded in the collagen matrix, mostly arranged parallel to each other and to the long axis of the collagen fibrils [Fratzl and Weinkamer, 2007]. Furthermore, the mineral platelets are arranged predominantly parallel to the longitudinal direction of the bone [Fratzl, Gupta 2004]. Bone mineral particles possess thicknesses depending on the species ranging from 1.5 to 4.5 nm [Glimcher, 1984; Fratzl, Fratzl-Zelman et al., 1991; Fratzl, Gupta et al., 2004]. The mechanical properties of the bone are defined by the amount of calcium phosphate in bone. Size and shape of mineral particles in bone tissue can be mainly analyzed by transmission electron microscopy (TEM) [Traub, Arad et al., 1992; Weiner and Traub, 1992; Landis, Hodgens et al., 1996] and small-angle X-ray scattering (SAXS) [Fratzl, Fratzl-Zelman et al., 1991; Fratzl, Groschner et al., 1992; Rinnerthaler, Roschger et al., 1999; Paris, Zizak et al., 2000].

The third major component of bone is water, which is located within the collagen fibril. In particular, the water molecules are localized in the gap-zones and between the triple helical molecules. It is also present between fibrils and fibers [Weiner and Wagner, 1998].

On the microscopic level of hierarchy, bone is composed of intercellular calcified material called bone matrix, and different types of cells, namely osteoprogenitor cells, osteoblasts, osteocytes, bone lining cells and osteoclasts (see **Figure 2-1**) [Boskey and Posner, 1984; Freemont, 1993]. The functions of each of these cells are discussed in the following.

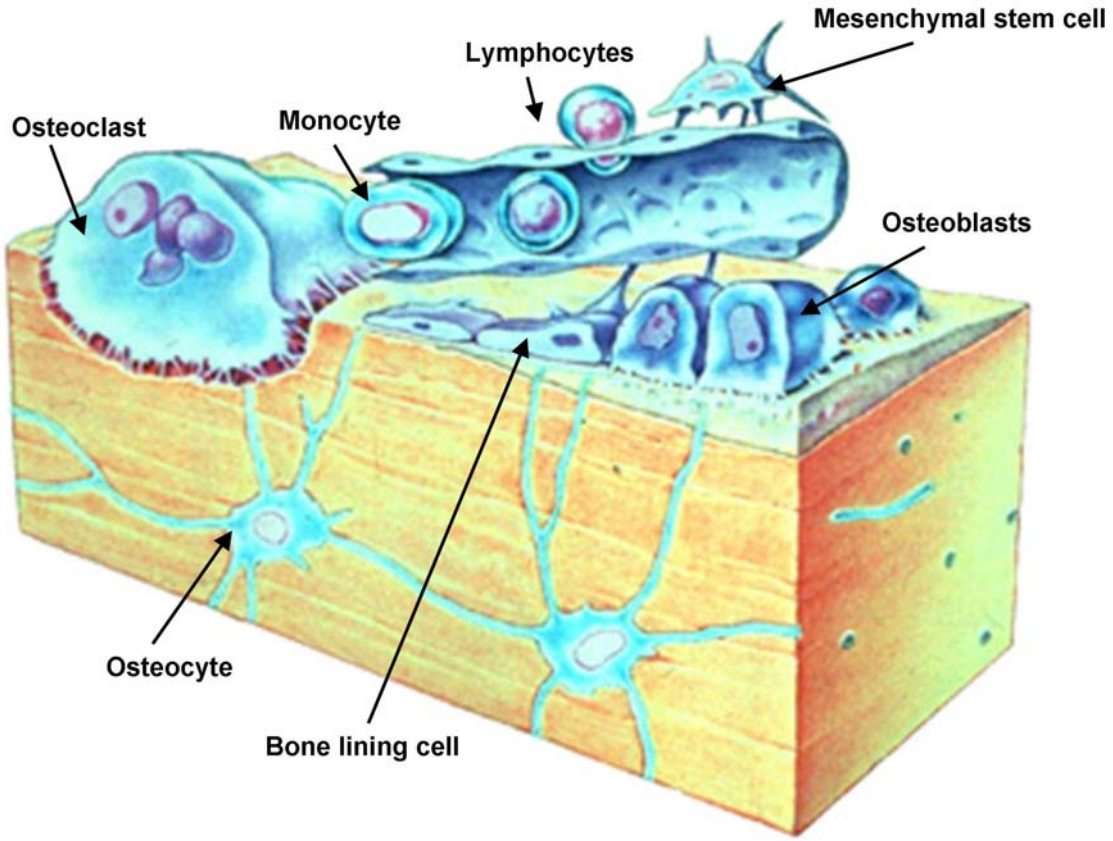

Figure 2-1: Overview of different types of bone cells. Various cells of the bone tissue are depicted, including osteoblasts, bone forming cells, originating from mesenchymal stem cells as well as osteoclasts, bone resorbing cells, originating from monocytes. Furthermore, osteocytes, being originally osteoblasts embedded in the bone matrix, are presented as well as flattened osteoblasts, called bone lining cells [Bartl].

Osteoprogenitor cells are found on or near all surfaces of bone. These cells have the potential to differentiate into chondroblasts, cells forming cartilage, or into osteoblasts, cells forming bone. Osteoprogenitor cells are most active in the postnatal period during the growth of bones, but are also active in adult life during repair of bone injury [Zoetis, Tassinari et al., 2003]. Osteoprogenitor cells are mononuclear cells originating from mesenchymal stem cells (MSCs). MSCs exhibit the potential to undergo differentiation into various types of cells. The differentiation of MSCs can be influenced by constituents of the extracellular matrix (ECM). Especially the transforming growth factor β (TGF-β) and bone morphogenetic proteins (BMPs) play an important role, being strong regulators of proliferation, differentiation and matrix synthesis of cells [Brodt, Ellis et al., 1999]. The regulation of BMP signalling via the BMP-receptors and the related TGF-β signalling cascades have been intensively studied over the last years [Lutz and Knaus, 2002; Nohe, Keating et al., 2004]. Investigations on human MSCs demonstrated that these kinds of cells are multipotent cells in the bone marrow, which exhibit the potential to undergo differentiation in the direction of adipocytes, chondrocytes or osteoblasts [Pittenger, Mackay et al., 1999; Gronthos, Zannettino et al., 2003; Tuli, Tuli et al., 2003].

Osteoblasts are the cells responsible for bone formation. Mature osteoblasts are expressing a range of genetic markers such as OPN, OCN or ALP. During the differentiation process osteoblasts pass through different developmental stages. The following stages of the osteoblast development are distinguished *in vivo*: the proliferation of the pre-osteoblast, the differentiation into matrix producing osteoblasts and subsequently the bone mineralization by mature osteoblasts [Quarles, Yohay et al., 1992].

On bone surfaces, which are not remodeled, resting osteoblasts can be found, called bone lining cells [Baron, 1993]. These are flat and elongated cells. Although the primary function of osteoblasts is the production of bone, these cells have been shown to have a variety of other roles. For example, osteoblasts are involved in aiding bone resorption, organizing collagen fibrils and synthesizing matrix components such as type I collagen, proteoglycans and glycoproteins [Freemont, 1993].

In the course of bone formation several osteoblasts are embedded in the bone matrix and thus become osteocytes. Osteocytes are distributed in the whole bone and connected to each other via cytoplasmatic extensions forming a communicative network. Osteocytes are located in lacunae and their cytoplasmatic extensions occupying tiny cannels called canaliculi [Burger and Klein-Nulend, 1999]. Furthermore, canaliculi link osteocytes and blood vessels extensively [Shapiro, 2008]. There is the assumption that osteocytes play an important role in sensing mechanical forces applied to the bone. Investigations of Burger and Klein-Nulend demonstrated that osteocytes indeed are acting as mechano-sensitive cells which assimilate mechanical information and transmit them to effector cells such as osteoblasts and osteoclasts [Burger and Klein-Nulend, 1999]. The exact function of osteocytes is still not completely understood.

The antagonists of the bone forming osteoblasts are the bone resorbing osteoclasts. These multinucleated cells descend, different than the osteoblasts, from hematopoietic stem cells of the bone marrow, specifically from the monocytes/macrophages [Roodman, 1999]. The proliferation and activation of osteoclasts is dependent on cell-to-cell contacts to osteoblasts [Fuller, Gallagher et al., 1991]. Furthermore, there is the regulation of their activity by systemic factors [Yasuda, Shima et al., 1998]. The functional organelle of the osteoclasts concerning bone resorption is called ruffled border. Osteoclasts synthesize acids and hydrolases digesting the underlying bone matrix which is subsequently removed via endocytosis. As a result of the osteoclasts bone resorption activity so-called howship's lacunae are formed. After bone resorption osteoclasts undergo apoptosis.

The next higher hierarchical level comprises the arrangement of the major bone components, collagen type I and the mineral particles. Although there are different categories describing the hierarchical structure of bone, its basic building block, the mineralized collagen fibril, is rather universal [Rho, Kuhn-Spearing et al., 1998; Weiner and Wagner, 1998; Fratzl, Gupta et al., 2004]. Thus, on the nanometer scale, bone can be described as a collagen/mineral composite consisting of mineral particles embedded in the collagen matrix. Mineralized collagen fibrils are almost always present in bundles or arrays. There are four common patterns concerning fibril arrays (see **Figure 2-2**), (1) Arrays of parallel fibrils, (2) woven fiber structure, (3) plywood-like structure, and (4) radial fibril array [Weiner and Wagner, 1998]. Based on the different arrangement of the fibrils various types of bone are distinguished.

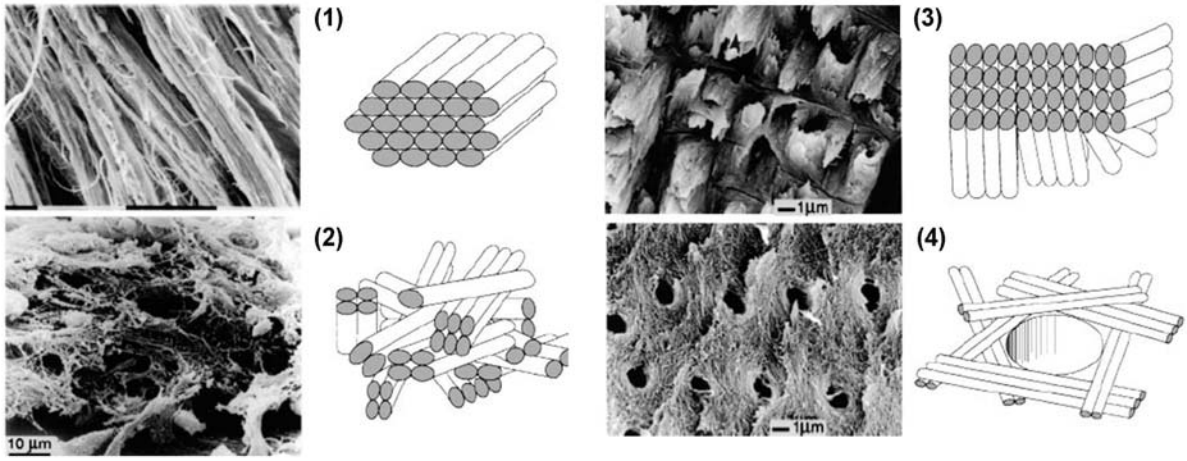

Figure 2-2: Fibril array patterns. Different array patterns of collagen fibrils are formed in bone tissue. (1) array of parallel fibrils, (2) woven fiber structure, (3) plywood-like structure and (4) radial fibril array; adapted from [Weiner and Wagner, 1998].

(1) The collagen fibrils in arrays of parallel fibrils are aligned along their longitudinal axis as in parallel-fibered bone. This type of bone is typically found in the bovid family and is formed very rapidly during early development.

(2) Fibrils in the woven fiber structure are arranged in bundles of different diameter. These fibril bundles are loosely packed and randomly oriented. This fibril array can be found in woven bone, characteristically present in the skeletons of amphibians and reptiles as well as in the skeleton of the mammalian embryo. Woven bone is a primary bone, formed whenever bone formation needs to proceed rapidly as in case of early bone development and healing [Shapiro, 2008]. During normal maturation woven bone is gradually replaced by lamellar bone.

(3) The plywood-like structures are described by sets of parallel fibrils and/or fiber bundles present in discrete layers with a different fibril orientation in each layer. The plywood-like

structure is characteristically for lamellar bone. Simple lamellar bone is often found in large blocks in reptiles or as circumferential lamellae in birds and mammals [Currey, 2002]. In the mammalian lamellar bone various separated bone lamellae are concentrically arranged around a central canal containing a blood vessel. The unit of the central blood canal and bone lamellae is named osteon. Osteons are a special type of lamellar bone. There are two kinds of osteons, primary and secondary. Primary osteons are structures around blood vessels that are formed when the bone is initially formed. Secondary osteons replace existing bone by a process in which osteoclasts first resorb a tubular path, and then osteoblasts build up the osteon layer by layer. The outer limits of secondary osteons are defined by distinct borders called cement lines. The central blood canal in secondary osteons is called Haversian canal.

(4) The radial fibril array is characteristic of the bulk of dentin, forming the inner layer of teeth. The fibrils are aligned in plane parallel to the surface. However, within that plane the bundles are rather randomly oriented.

On the next higher level of hierarchy two types of bone are morphologically distinguished, compact bone and trabecular bone (see **Figure 2-3**).

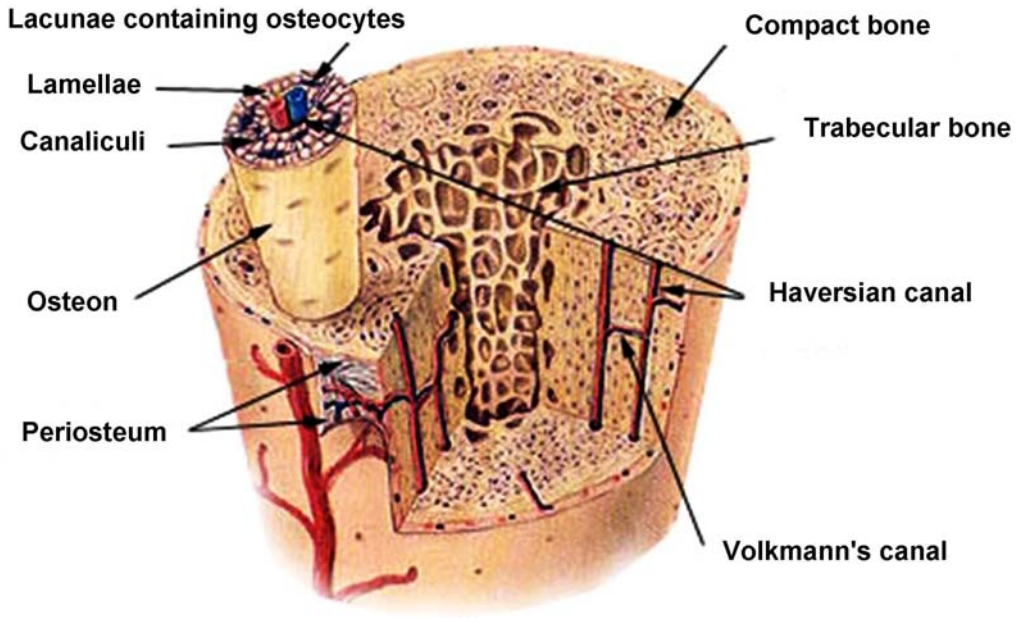

Figure 2-3: Schematic drawing of a piece of a long bone. The constituent parts are represented, including the outer part of the bone made up of compact bone with osteons and the inner part of the bone built up of trabecular bone. The big blood vessels supplying the bone tissue with nutrient are the vertically aligned Haversian canals and the horizontally aligned Volkmann's canals [SEER].

Compact bone forms the outer shell, called the cortex, of most bones in the skeleton. It shows varying architecture for different bones and different species. In human long bones for instance the compact bone is built up of lamellar bone consisting of lamellae and osteons (see **Figure 2-3**). Besides the Haversian canals there are transverse canals to be found called Volkmann's canals, providing blood supply of the marrow space from the periosteum. The cortical bone shell at the outer surface of each bone can reach a thickness between several hundred micrometers (in vertebra) to several millimeters or even centimeters (in the midshaft of long bones) [Fratzl and Weinkamer, 2007]. In the adult human skeleton, compact bone makes up about 80% of the total bone mass. Mineral particles in compact bone are predominantly oriented parallel to the long axis of the bone [Fratzl, Gupta et al., 2004], oriented in the same direction as the collagen fibrils [Tesch, Vandenbos et al., 2003; Fratzl and Weinkamer, 2007].

Trabecular bone is composed of a network of thin bone rods, plates and arches. The spaces between are occupied by bone marrow and cells. Trabecular bone has a porosity of about 80% and can thus be considered as a foam-like network of bone trabeculae, therefore often called spongy bone. The thickness of the struts in the trabecular bone is fairly constant between one and three hundred micrometers [Fratzl and Weinkamer, 2007]. This kind of bone tissue typically comprises the internal structure of bones such as flat bones, short bones or the ends of long bones (for more details see paragraph on bone shapes later in this chapter 2.1.1). The material of a bone lamella in trabecular bone is similar to cortical bone, not organized in cylindrical sheets but in a similar layered structure. On the level of the nanocomposite of collagen fibrils and mineral particles it is known that the main orientation of both the collagen fibrils and the mineral particles follows quite closely the trabecular orientation [Rinnerthaler, Roschger et al., 1999; Roschger, Grabner et al., 2001; Jaschouz, Paris et al., 2003]. Trabecular bone is mainly responsible for the metabolic function of the bone due to its high surface-to-volume ratio [Fratzl and Weinkamer, 2007].

Mature compact bone and trabecular bone are both made up of lamellae, or stacks of parallel or concentrically curved sheets of bone. Each lamella is about 3 to 7 μm thick, composed of highly organized and densely packed collagen fibers [Zoetis, Tassinari et al., 2003]. Both compact and trabecular bone contain regularly spaced small cavities called lacunae that each contain an osteocyte (see paragraph on osteocytes beforehand in this chapter 2.1.1).

On the macroscopic level of hierarchy bones are distinguished into five bone types according to their outer shape: (1) long bones, (2) flat bones, (3) short bones, (4) irregular bones and (5) sesamoid bones (see **Figure 2-4**).

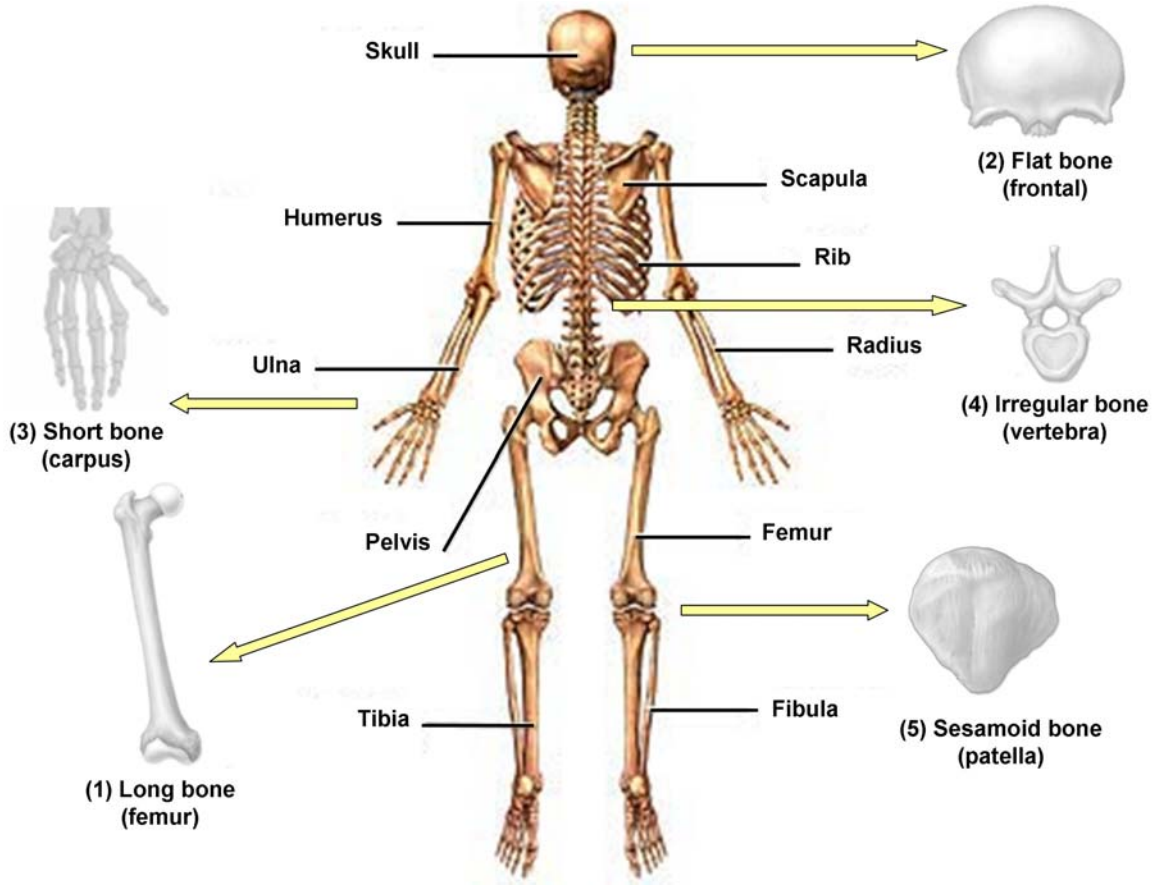

Figure 2-4: Overview drawing of the different bone types and their location in the skeleton. Different bone shapes leading to the names of different bone types. (1) femur of the leg as an example of a long bone, (2) frontal bone of the skull as an example of a flat bone, (3) carpus of the hand representing a short bone, (4) vertebra as an example of an irregular bone and (5) patella of the knee representing a sesamoid bone.

(1) Long bones are typically found in the extremities characterized by their high aspect ratio, length versus thickness. Their overall structure includes different regions exhibiting different functions and morphologies. The functional parts on both ends of a long bone are called epiphyses while the tubular midshaft of the bone is referred to as diaphysis. During postnatal growth, the epiphyses are separated from the diaphysis by a cartilaginous epiphyseal plate that is connected to the diaphysis by an area of spongy bone called the metaphysis. The outer shell of long bones consists of compact bone, whereas the epiphyses are filled with trabecular bone. Spaces in the bone material are filled with bone marrow. Long bones include the upper bone of the leg, called femur, the lower bone of the leg, the tibia, and the small bone of the lower leg, named fibula (see **Figure 2-4**). Furthermore, the upper bone of the arm, called humerus, the lower bone of the arm, named radius, and the small bone of the lower arm, the ulna, are counted among the long bones (see **Figure 2-4**).

(2) Flat bones are thin bones, typically found where extensive protection or broad surfaces for muscular attachment are required. These bones are broad flat plates composed of two

thin layers of compact bone enclosing trabecular bone. Flat bones include the cranium of the skull, the ilium of the pelvis and the rib cage (see **Figure 2-4**).

(3) Short bones have an almost cubic shape and are typically found where the skeleton is intended for strength and compactness in combination with limited movement. These bones are built up of thin layers of compact bone enclosing trabecular bone tissue. Short bones include the carpus in the wrist and the tarsus in the ankle (see **Figure 2-4**).

(4) Irregular bones are bones that due to their shape cannot be grouped as long, short, flat or sesamoid bones. These bones exhibit a complex shape according to their function such as protection of nervous tissue, forming anchor points for skeletal muscle attachment or maintaining pharynx and trachea support. Irregular bones consist as well of trabecular bone encircled by a thin layer of compact bone. These bones include vertebrae, sacrum and mandible (see **Figure 2-4**).

(5) Sesamoid bones are small bones embedded in tendon. These bones are found in joints such as the hand, knee or foot to protect the tendon and to increase its mechanical properties. An example of a sesamoid bone is the patella in the knee (see **Figure 2-4**).

In general, the external surfaces of bones are covered by a layer of fibrous connective tissue called periosteum that has the ability to produce bone. The periosteum is built up of two layers, an outer dense fibrous layer and an inner vascular cellular layer containing osteoblasts and osteoclasts [Zoetis, Tassinari et al., 2003]. The inner cavities of bone are lined with a layer of osteogenic connective tissue called endosteum. The endosteum is made up of a single layer of flattened osteoprogenitor cells and vascular connective tissue. All of the cavities of bone, including Haversian canals, are lined with endosteum.

2.1.2 Bone formation

The development of the vertebrate skeleton is achieved by two mechanisms, intramembranous bone formation and endochondral bone formation [Karsenty, 2003; Zoetis, Tassinari et al., 2003; Forriol and Shapiro, 2005; Shapiro, 2008]. Bone development starts with a differentiation of cells into chondrocytes or osteoblasts, which form cartilage and bone, respectively [Olsen, Reginato et al., 2000]. In the following paragraph intramembranous and endochondral ossification are shortly described.

Intramembranous ossification is mediated by the inner periosteal osteogenic layer. During intramembranous ossification mesenchymal cells differentiate along a preosteoblast to osteoblast line [Shapiro, 2008]. Osteoblasts produce unmineralized bone matrix, called osteoid, which is subsequently mineralized. Most flat bones of the human skeleton are

formed by intramembranous ossification. Additionally, phases of short bone formation are characterized by intramembranous bone formation as well as the thickening of long bones.

Endochondral ossification is characterized by the initial synthesis of cartilage followed by bone formation occurring for instance during embryonic long bone formation. It starts with the formation of a cartilage model which resembles the shape of the developing bone. This cartilage model degenerates, and parts of the cartilage mineralize forming a network made up of the calcified cartilage remnants. Osteoblasts subsequently deposit continuous layers of bone onto the calcified cartilage remnants. However, there are two regions where the cartilage remains, specifically the joint region and the region of the growth plate (epiphyseal plate) [Shapiro, 2008].

The following paragraph describes both processes of bone formation in detail using the example of long bone development in rodents since this is the essential element of this study as natural bone development is studied on mice. When compared to the rat or human, ossification in the rodent skeleton occurs over a relatively short period of time, in particular in mice [Patton and Kaufman, 1995]. Mice are thus a convenient model system to study bone formation. Unlike the skeleton of large mammals, the rodent skeleton lacks Haversian systems.

The process of long bone development involves both endochondral and intramembranous ossification. Long bone development starts with the formation of a cartilage model which resembles the shape of the developing long bone (see **Figure 2-5**). The first parts mineralized in the developing long bones are the bone shell, named bone collar, and small spots in the midshaft region (see **Figure 2-5**). The bone collar is formed by intramembranous ossification in the central region of the cartilage model of the bone. The region of the first mineralization in the midshaft of the diaphysis, consisting of islands of newly formed bone, is called primary ossification center (see **Figure 2-5**). Patton et al. found the first ossification center in few of the investigated murine femora at day 15 of pregnancy and at fetal stage day 16 it was visible in all animals analyzed, representing that mineralization starts after fetal day 15 [Patton and Kaufman, 1995; Miller, Little et al., 2007]. Subsequently, the cartilage model degenerates, beginning in the midshaft. The primary ossification center is further developing by processes such as cell enlargement of the chondrocytes, cartilage mineralization and cell death resulting in a network made of the calcified cartilage islands. With invasion of blood vessels into the primary ossification center, osteoprogenitor cells are attracted to this region and differentiate into bone forming osteoblasts [Shapiro, 2008]. The osteoblasts deposit continuous layers of bone onto the calcified cartilage remnants. Afterwards, secondary ossification centers arise in the distal ends (pointing away from the body center) and proximal ends (pointing to the body center)

of the cartilage model, called epiphyses (see **Figure 2-5**). Between these epiphyseal ossification centers and the diaphysis, the midshaft of the long bone, a thin disk of cartilage remains, called the epiphyseal growth plate (see **Figure 2-5**). The growth plate facilitates lengthening of long bones and creates a barrier between the epiphysis and diaphysis. As bone is formed at the growth plate, the epiphysis moves away from the diaphysis and bone is deposited in the transitional region called the metaphysis located directly below the epiphyseal growth plate. At the growth plate, endochondral bone formation occurs, meaning that layers of cartilage are replaced by layers of bone. During postnatal bone development in mice, describing bone development after birth, a secondary ossification center in the femur can be observed in the head of the femur, 15 days after birth [Zoetis, Tassinari et al., 2003]. In the process of postnatal development, the trabecular bone of the metaphysis is divided into two different regions, the primary spongiosa and the secondary spongiosa. During long bone growth in length, the primary spongiosa fills the areas that were previously occupied by the growth plate followed by the secondary spongiosa. As bone formation proceeds at the growth plate, most of the primary spongiosa is converted into secondary spongiosa [Zoetis, Tassinari et al., 2003]. When long bones have reached their adult length the epiphyseal growth plate fuses with the diaphysis, thus removing the barrier between the epiphyses and the diaphysis. Once fusion of the epiphyseal growth plate occurs, longitudinal bone growth can no longer occur. Besides lengthening of long bones, thickening is necessary to support increased load. Diametric increase in bone arises from periosteal apposition. Unlike longitudinal bone growth, periosteal apposition can occur at any time during development and is a form of intramembranous bone formation. During appositional growth osteoblasts from the inner layer of the periosteum secrete matrix on the outside surface of bone. While bone is deposited on the periosteal surface, osteoclastic resorption on the endosteal surface regulates the thickness of the diaphyseal cortex. The amount of bone in the cortex remains fairly constant throughout growth due to this coupled deposition and resorption. The overall diameter of the diaphysis increases rapidly, whereas the thickness of the cortex increases slowly. During postnatal growth the shape of a growing bone is maintained by continuous remodeling of the bone surface involving bone deposition on some periosteal surfaces and resorption on other periosteal surfaces [Zoetis, Tassinari et al., 2003; Shapiro, 2008].

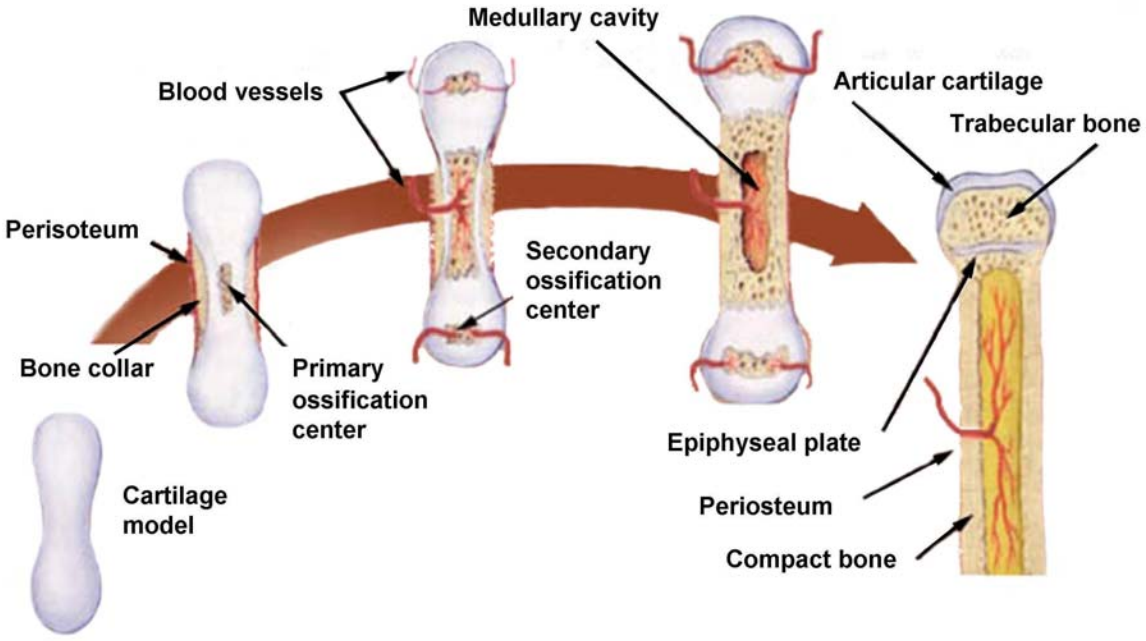

Figure 2-5: Bone formation. Schematic drawing of the events involved in long bone formation, including the formation of the periosteal bone collar, the primary and the secondary ossification centers and the invasion of blood vessels as well as the developing marrow space. On the right, the fully developed long bone is schematically illustrated with persistent cartilage at the joint (articular cartilage) and at the growth plate (epiphyseal plate), the bone shell of compact bone and the epiphysis filled with trabecular bone [SEER].

Concerning bone development it could be demonstrated that muscle function is necessary and plays thus a critical role for successful development of the skeleton besides its important role in mediating bone health throughout life [Gross, Poliachik et al., 2010]. Moreover, there are investigations emphasizing the regulating role of mechanical stimuli on the skeletal development by demonstrating that the mineralization process starts just when the first muscle contraction occurs, suggesting that the mineralization is stimulated by mechanical loads [Burger, Klein-Nulend et al., 1991; Tanck, Van Donkelaar et al., 2004]. Thus, mechanical loading seems to be important not only for maintenance but also during development of the fetal skeleton.

2.1.3 Bone remodeling

Bone is a highly dynamic tissue, which is remodeled continuously. Bone remodeling is a complex process comprised of bone resorption by osteoclasts and bone formation by osteoblasts (see **Figure 2-6**). Due to the controlled interaction of osteoblasts and osteoclasts bone has the ability to adapt to changing biomechanical needs.

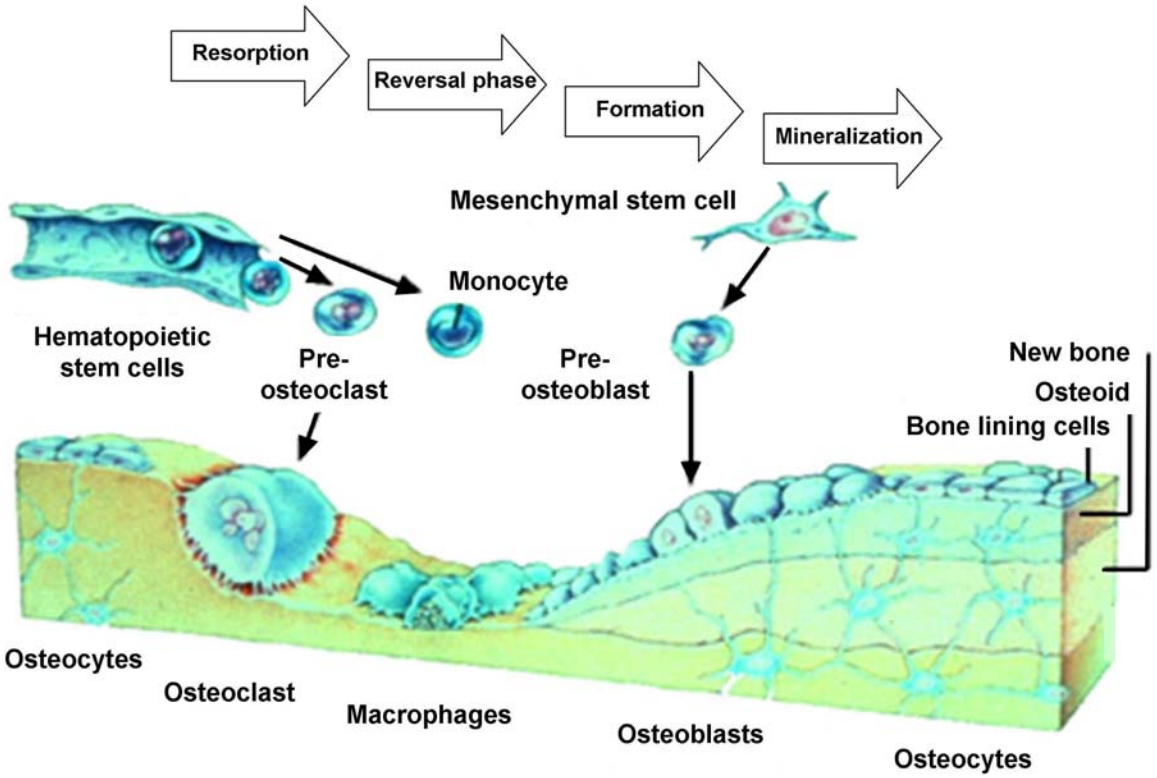

Figure 2-6: Bone remodeling. Bone resorption by osteoclasts is followed by a reversal phase and subsequently bone formation by osteoblasts occurs. Various types of bone cells are illustrated [Bartl].

During growth, biological structures and materials such as bone are able to adapt their architecture to improve their functionality according to external constraints. Later on, after growth has finished, biological systems can adapt to changes in the environment. The ability of bone to adapt to a changing mechanical environment is based on a permanent remodeling of the material. Bone remodeling describes all processes involving resorption and deposition of bone. The newly deposited matrix, initially unmineralized, is then mineralized by osteoblasts. Trabecular bone therefore can be described as a patchwork of bone packets of different mineral content as a result of ongoing remodeling. While resorption takes place in 1 to 3 weeks, bone formation is about several months [Fratzl and Weinkamer, 2007]. In cortical bone the outer surface accessible to osteoclasts is strongly reduced, therefore remodeling takes place by forming new osteons. Bone remodeling is not random but a mechanically controlled process. The so-called Wolf-Roux law states that bone is deposited wherever mechanically needed and is resorbed wherever there is no mechanical need. This idea was further developed by Frost who proposed that a mechanically controlled feedback loop is active in bone and regulating bone mass and architecture as an adaptive response to needs of external mechanical loading by simultaneous bone resorption and formation at different sites [Frost, 1987].

Bone remodeling is controlled by hormones and local factors and is organized in different phases [Baron, 1993; Hill, 1998]. Resorption of old bone describes the first phase of bone

remodeling, where osteoclasts resorb a distinct area of the mineralized bone matrix (see **Figure 2-6**). For that purpose the differentiation of the osteoclast progenitor cells into osteoclasts is essential. The unmineralized osteoid is removed by bone lining cells, producing various proteolytic enzymes, such as matrix metalloproteinases (collagenase, gelatinase) [Meikle, Bord et al., 1992]. Thus, bone lining cells make the mineralized matrix accessible to osteoclasts, since osteoclasts are able to recognize matrix proteins via members of the integrin family. Activated osteoclasts are first dissolving the mineralized bone matrix by producing an acidic milieu and subsequently degrading the organic matrix with the help of proteolytic enzymes. The following cessation of the activity of osteoclasts is named reversal phase (see **Figure 2-6**). The mechanisms leading to the reversal phase are still unknown [Hill, 1998]. Afterwards MSCs and pre-osteoblastic cells start to proliferate and differentiate and the phase of bone formation starts (see **Figure 2-6**). Due to matrix degradation by osteoclasts growth factors from the matrix are released influencing the differentiation of osteoblasts. The differentiation of progenitor cells into osteoblasts is stimulated by constituents of the ECM, in particular BMPs or TGF-β [Alberts, 1995]. Mature osteoblasts fill the resorption lacunae with osteoid, which is subsequently mineralized (see **Figure 2-6**). Several of the osteoblasts are trapped in the bone matrix and become osteocytes. After filling the resorption lacunae osteoblasts flatten increasingly and become bone lining cells. The initiation of that phase occurs due to local factors.

2.2 Biomineralization

Minerals formed by biomineralization develop under controlled conditions of a biological system. Biominerals are typically connected to organic components, thus forming a composite material, such as the collagen/mineral composite in bone [Weiner and Dove, 2003]. There are two types of biomineralization, biological induced and biological controlled mineralization [Lowenstam and Weiner, 1989; Mann, 2001]. Biological induced means that the minerals are produced by interaction of the metabolism and the environment of the organism. During the biological induced mineralization the cell surface often act as nucleation site and agent for mineral growth [Weiner and Dove, 2003]. The minerals formed by that process are very heterogeneous concerning their external morphology, water content, structure and particle size. The second type of biomineralization, biological controlled mineralization, describes a highly regulated process to form mineral particles such as these of bone and teeth. During the process of biological controlled mineralization the organism uses cellular activities to control nucleation, growth, morphology and the location of the minerals formed [Weiner and

Dove, 2003]. These processes may occur extra-, inter- or intracellular. Mineral particles formed via biological controlled mineralization exhibit a homogeneous particle size, definite structure and composition as well as a high level of spatial organization. Bones and teeth are believed to mineralize by extracellular biological controlled mineralization [Lowenstam and Weiner, 1989; Veis, 2003].

2.2.1 Calcium phosphates

As an example of biominerals calcium phosphates are described in the following since these are the minerals formed during bone development in vertebrates. Calcium phosphates are formed via biological controlled mineralization. Phosphates in general account for 25% of the biogenic mineral particles. Due to different stoichiometric composition, there are different types of calcium phosphates such as HA, octacalcium phosphate (OCP) or amorphous calcium phosphate (ACP). The minerals in vertebrate bones and teeth consist of carbonated HA, termed dahllite [Lowenstam and Weiner, 1989; Veis, 2003]. Apatites, such as HA, are the most stable phases among the calcium phosphates and can be considered as the probable end-product in many reactions [Chow, 2001]. OCP has a remarkable structural similarity to HA due to its layered structure involving apatitic and hydrated layers [Wang and Nancollas, 2008]. OCP crystals are typically small and extremely platy. OCP has a significant biological relevance due to its role as possible precursor during the formation of carbonated apatite in the hard tissues of vertebrates [Crane, Popescu et al., 2006; Wang and Nancollas, 2008]. It was first proposed by Brown et al. that OCP forms the first mineral phase in enamel mineralization [Brown, 1962]. Under physiological conditions OCP is thermodynamically a metastable phase and tends to hydrolyze to HA [Chow, 2001; Wang and Nancollas, 2008]. ACP appears to have a relatively constant composition, despite the absence of a long-range periodic order [Chow, 2001]. ACP has an apatitic short-range structure, but with a crystal size so small that it appears to be amorphous by X-ray analysis [Wang and Nancollas, 2008]. ACP minerals are spherical particles. In general ACP is a highly unstable phase that hydrolyzes almost instantaneously to more stable phases such as OCP or apatite [Chow, 2001; Wang and Nancollas, 2008]. ACP as well as OCP plays an important role as possible precursor mineral phase in vertebrates [Crane, Popescu et al., 2006; Mahamid, Sharir et al., 2008; Beniash, Metzler et al., 2009; Mahamid, Aichmayer et al., 2010].

2.2.2 Precursor in biomineralization

Since decades a fundamental question in understanding the mineralization process in vertebrates is the nature of the first formed mineral phase [Betts, Blumenthal et al., 1981; Boskey, 1997; Weiner, 2006; Grynpas, 2007]. The initial stage of biological mineralization remains controversial but there is strong evidence that the transient precursor strategy also occurs in vertebrates [Weiner, 2006; Grynpas, 2007]. Many theories of bone mineral formation have been postulated over the last few decades. The main theory on bone mineral formation is that the mineral is initially deposited as ACP. The strategy of a transient mineral phase has been investigated since the 1960s. Termine and Posner proposed that ACP may be a precursor phase in bone formation [Termine and Posner, 1967]. It was further argued by Betts et al. that the initial ACP precursor underwent a solid-state transformation to poorly crystalline apatite but can be stabilized by a number of chemical species in solution. Examples of such stabilizers are: magnesium ions, adenosine triphosphate (ATP), pyrophosphate and proteoglycans. Betts et al. suggest that magnesium enters the prenuclei structures preventing further HA development by creating a structural mismatch [Betts, Blumenthal et al., 1981]. Bonar et al. could demonstrate that there is the formation of ACP during embryonic chick bone development [Bonar, Roufosse et al., 1983]. Wuthier et al. reported that extracellular matrix vesicles, believed to be the sites of initial calcification, contained ACP [Wuthier, Rice et al., 1985]. Magnesium and ATP, which are highly concentrated in the vesicles, were earlier postulated to stabilize ACP [Landis and Glimcher, 1978]. Lowenstam and Weiner revealed evidence that in many invertebrates the initial mineral is amorphous and that these amorphous minerals also transform to crystalline phases as the animals mature [Lowenstam and Weiner, 1985; Lowenstam and Weiner, 1989]. Recently, ACP precursor phases have been reported to be deposited first during the formation of enamel [Beniash 2009] and zebra fish bone [Mahamid, Sharir et al., 2008; Mahamid, Aichmayer et al., 2010], before the mineral is transformed into carbonated HA. But this is still an elementary question in mammalian systems. Besides ACP as a precursor mineral phase in biomineralization it could be demonstrated that OCP acts as a transient precursor of biological apatite [Brown, 1962]. OCP is less thermodynamically stable than apatite under physiological conditions and shares similar crystallographic planes with HA [Grynpas, 2007]. One proposed explanation of the plate shaped mineral particles in mature bone assumes that they grow via an OCP transition phase. OCP crystals are plate-shaped and have a structure very similar to apatite, except for the presence of a hydrated layer [Weiner and Wagner, 1998]. Raman spectroscopic data obtained from murine intramembranous mineralization model confirms

the OCP, and possibly the ACP transient precursor strategy for vertebrate biomineralization [Crane, Popescu et al., 2006].

Amorphous biominerals are minerals with atoms having no ordered structure, showing irregular patterns and mostly exhibiting a lower density than crystalline materials. As precursor stages of crystalline mineral often hydrated forms of mineral particles, such as OCP, are found. These hydrated mineral particles exhibit a low energy barrier for nucleation and growth in an aqueous phase and are thus favored [Weiner and Dove, 2003].

Besides the question of the first formed mineral in biomineralization of vertebrates the question of how the mineral is delivered to the crystallization site is an issue of discussion. There are different mechanisms described in literature, represented in the following.

Although the initiation of the mineralization process is not yet fully understood, it is widely accepted that it starts in the gap-zones of the periodically staggered collagen molecules in the collagen fibrils [Landis, Song et al., 1993] since studies of crystal growth in fibrils showed that the first formed mineral particles are indeed in the gap-zones [Nylen, Scott et al., 1960; Weiner and Wagner, 1998]. With proceeding mineralization the mineral particles grow and extend into the overlap-zones with their crystallographic c-axes parallel to the collagen long axis. However, it could be recently demonstrated that positive charges at the C-terminal end of collagen molecules promote mineral infiltration of the collagen fibrils [Nudelman, Pieterse et al., 2010]. Clusters of amino acids, leading to the positive charge at the end of the collagen molecules, form nucleation sites of mineralization and are present in both gap- and overlap-zones. A model to explain how intrafibrillar mineralization of collagen can be achieved during bone formation is the pathway via liquid precursors. Gower et al. first proposed the term polymer-induced liquid precursor (PILP) process for the formation process of liquid precursors during calcium carbonate development [Gower and Odom, 2000]. Olszta et al. revealed evidence, based on an *in vitro* model system, that the PILP process may also play a fundamental role in the biomineralization of bones and teeth in vertebrates [Olszta, Cheng et al., 2007]. They propose that HA mineral particles in mineralized collagenous tissue, such as bone and teeth, do not initially nucleate within the gap-zones, but rather a liquid-phase amorphous precursor is drawn into the collagen fibrils via capillary action, and upon solidification, the precursor crystallizes, leaving the collagen fibrils embedded with nanoscopic platelets of HA. This liquid-phase precursor could be induced by polyanionic proteins, which they assume would be one or some combination of the polyanionic NCPs found associated with bone.

Another suggestion on the initiation of mineralization in vertebrates is the control of the mineralization via polyphosphates. Polyphosphates are inhibitors of the apatite crystal growth and they form strong complexes with divalent cations such as calcium [Omelon, Georgiou et al., 2009]. Omelon et al. found polyphosphates collocated with calcifying cartilage and resorbing bone indicating that they play a role in the mineralization process. Calcium-polyphosphate complexes are believed to serve as calcium and orthophosphate stores when apatite formation is not desired. In the case of desired apatite formation, tissue non-specific alkaline phosphatase cleaves orthophosphates from the calcium-polyphosphate complexes, resulting in an increased orthophosphate concentration and the release of calcium which promotes the apatite mineral formation [Omelon, Georgiou et al., 2009]. Thus, the mineralization can be controlled by enzymatic formation, namely condensation, and destruction, namely hydrolytic degradation, of polyphosphates, displaying a simple mechanism for controlling phosphate and calcium accumulation.

2.3 Bone development in NF1 mice

Neurofibromatosis type I (NF1), formerly known as Morbus Recklinghausen, is a common inherited disorder caused by a single gene. NF1 is a tumor disorder that is caused by the malfunction of the gene Nf1, encoding for neurofibromin 1, that is responsible for the control of cell division [Wu, Estwick et al., 2006]. NF1 is primarily characterized by the formation of tumors (neurofibromas) along peripheral and optical nerves that are derived from Schwann cells, café-au-lait spots, freckling and is interestingly often associated with a bone and cartilage phenotype, such as bowing of the tibia and fusion of joints [Wu, Estwick et al., 2006; Kolanczyk, Kossler et al., 2007; Kolanczyk, Kuhnisch et al., 2008; Schindeler and Little, 2008]. Thus, there seems to be a relation between the functioning of Nf1 and bone formation as Kolanczyk et al. could demonstrate that the Nf1 knockout leads to dysfunctional and malformed limbs in mice, including abnormal joint cartilage and bones [Kolanczyk, Kossler et al., 2007].

Neurofibromin 1 is robustly expressed during fetal development throughout a wide range of mesenchymal and neural crest derived tissue. Osteoblasts, osteoclasts, chondrocytes, fibroblasts and vascular endothelial cells all express the Nf1 gene product, neurofibromin 1, and may be functionally compromised when levels are decreased or absent [Schindeler and Little, 2008]. Neurofibromin 1 is a negative regulator of the Ras signal transduction pathway. Ras is an enzyme, in particular a small guanosine triphosphate phosphatase (GTPase), involved in cellular signal transduction [Wu, Estwick et al., 2006]. Binding the domain of GTPase activating proteins (GAP) of neurofibromin 1 by Ras proteins

stimulates the GTPase activity of Ras resulting in the hydrolysis of the active Ras-guanosine triphosphate (GTP) state to the inactive Ras-guanosine diphosphate (GDP) state. Ras is at the apex of multiple signaling pathways, including for instance the mitogen-activated protein kinase (MAPK) pathway [Wu, Estwick et al., 2006]. This pathway is involved in the modulation of multiple cellular functions, such as cell proliferation, differentiation and survival. NF1 deficiency results in an increase in Ras activity, which leads to a missing inhibition of the signaling pathway causing increased cell proliferation [Wu, Estwick et al., 2006].

To analyze the function of the Nf1 gene, it can be switched off in a so called knockout mouse. Knockout mice are genetically engineered mice in which one or more genes have been turned off. Knockout mice are important animal models for studying the role of genes which have been sequenced but whose functions have not been determined. To investigate the function of neurofibromin 1 in skeletal development, the gene Nf1 can be inactivated during early mouse limb development using the transgenic mouse line Prx1Cre strain C57BL/6 [Kolanczyk, Kossler et al., 2007]. When $Nf1^{flox/flox}$ mice are crossed with Prx1Cre transgenic mice the resulting $Nf1_{limb}^{-/-}$ mice exhibit an absent Nf1 gene expression in all mesenchymal cells of the developing limb [Kolanczyk, Kossler et al., 2007].

It was reported that $Nf1_{limb}^{-/-}$ knockout mice develop dysfunctional and malformed limbs, including abnormal joint cartilage and bones [Schindeler and Little, 2008]. These mice show a bone phenotype, including bowing of the tibia and fusion of joints. Tibial bowing is assumed to be caused by decreased stability of the cortical bone due to a high degree of porosity, decreased stiffness and reduction in the mineral content [Kolanczyk, Kossler et al., 2007]. Osteoblasts show an increase in proliferation and a decrease in the ability to differentiate and mineralize *in vitro*. The reduction in growth of $Nf1_{limb}^{-/-}$ mice is due to lower proliferation rates and a differentiation defect of chondrocytes. Thus, Nf1 has multiple roles in skeletal development including joint formation, growth plate function, osteoblasts differentiation and control of vessel growth [Kolanczyk, Kossler et al., 2007].

2.4 Artificially induced bone development – Tissue engineering

In the field of tissue engineering, the principles of engineering and life science concerning the development of biological substitutes that restore, maintain or improve tissue function, are applied [Langer and Vacanti, 1993]. There are three common possibilities to generate new tissue: (i) isolated cells or cell substitutes, (ii) tissue-induced substances, and (iii) cells placed on or within matrices [Langer and Vacanti, 1993]. Following the tissue engineering paradigm, the materials used for artificially induced tissue development will be resorbed

and replaced over time by, and in tune with the body's own, newly regenerated biological tissue [Langer and Vacanti, 1993].

The field of application in engineering tissues is very broad. It ranges from hard tissues (such as bone) to softer tissues (such as vocal cords), and furthermore, includes metabolically active tissues (such as the liver) and electrically functional tissues (such as the heart). Currently the "gold standard treatment" in tissue engineering of bone is a process called autografting, meaning the harvest of donor bone from a non-bearing site in the patient (such as the iliac crest) and the transplantation into the defect site [Stevens, 2008]. This transplantation of autologous bone has the best clinical outcome as it integrates reliably with host bone, not causing immune- and disease-related complications as do allogeneic bone, for instance from a human cadaver, or xenogeneic bone, for example from an animal source. But due to limitation in supply the search for new regenerative strategies is an important challenge.

On the one hand there are natural materials with the advantage that they contain information that facilitates cell attachment or maintenance of differentiated functions. On the other hand there are synthetic polymers, which allow precise control of molecular weight, degradation time, hydrophobicity and other attributes. However, many implants are made of composite materials, containing an organic phase and an inorganic component, and they are mostly highly porous three-dimensional (3D) structures [Langer and Vacanti, 1993]. Inorganic-organic composites aiming to "mimic" the composite nature of bone combine the toughness of a polymer phase with the compressive strength of an inorganic one to generate bioactive materials with improved mechanical properties and degradation profiles [Stevens, 2008]. The incorporation of a tricalcium phosphate (TCP), HA and basic salts into a polymer matrix produces a composite material.

A critical aspect of designing a material/scaffold for tissue engineering is to determine the appropriate composition, microstructure, pore size, porosity and surface chemistry to match the specific biological and metabolic requirements of tissues and disease states [Langer and Vacanti, 1993]. There are four characteristics how a material acting as a bone replacement material should be: (i) 3D and highly porous with an interconnected pore network for cell growth and flow transport of nutrients and metabolic waste, (ii) biocompatible and bioresorbable with a controllable degradation and resorption rate to match cell/tissue growth *in vitro* and/or *in vivo*, (iii) suitable surface chemistry for cell attachment, proliferation, and differentiation, and (iv) mechanical properties to match those of the tissue at the site of implantation [Hutmacher, 2000]. The scaffold or 3D construct needs to provide the necessary support for cells to proliferate and maintain their differentiated function, and its architecture defines the ultimate shape of the new bone and

cartilage [Hutmacher, 2000]. Porous materials with pore sizes higher than 100 µm allow bone to grow into the pores, which strengthens the union between the implant and the bone [Langer and Vacanti, 1993]. The scaffold should be fabricated from a highly biocompatible material, which does not have the potential to elicit an immunological body reaction [Hutmacher, Kirsch et al., 1998]. A polymer scaffold material needs to degrade and resorb at a controlled rate at the same time as the specific tissue cells seeded onto the 3D construct attach, spread and increase in quantity [Hutmacher, 2000].

While materials intended for implantation were in the past designed to be "bio-inert", they should be designed now to be "bioactive" materials that integrate with biological molecules or cells and regenerate tissue [Langer and Vacanti, 1993]. In the case of bone, materials should preferably be osteoinductive, promoting the differentiation of progenitor cells down an osteoblastic lineage, osteoconductive, supporting bone growth and encouraging the ingrowth of surrounding bone. Furthermore, these materials have to be capable of osteointegration, integrating into surrounding bone [Stevens, 2008]. Engineered materials can now be fabricated with unique biochemical and biophysical properties, that can be used to direct the interaction of biological systems with the engineered materials through the activation of specific biological signaling mechanisms [Stevens and Khademhosseini, 2010]. BMPs and TGF-β are promising strategies in stimulating bone growth [Langer and Vacanti, 1993]. The former induce both cartilage and bone formation, the latter augment bone growth. Bone growth can also be induced when cells are grown on synthetic polymers or ceramics [Langer and Vacanti, 1993].

Bone tissue engineering, using biomaterials and cells ranging from primary adult osteoblasts to bone marrow stem cells, has found a number of successes in animal models. However, the majority of studies are in rodents and only few report orthopedic applications in larger animals. This is understandable given the much smaller size of defects in rodents, higher bone remodeling rates, and lack of vascular supply in larger human defects [Stevens, 2008].

2.5 X-ray scattering characterization of bone

X-rays are electromagnetic waves. There are two distinct effects of X-rays interacting with the sample distinguished. On the one hand X-rays are absorbed by the sample, which is used to produce an X-ray image of the sample, called radiography. On the other hand there is scattering and diffraction of X-rays by the sample. If the scattered/diffracted radiation has the same wavelength as the incident radiation, it is called elastic scattering. The scattering process can be understood as such that electrons in the sample resonate with the

frequency of the X-rays passing through the object and emit coherent secondary waves, which interfere with each other [Glatter and Kratky, 1982]. Both X-ray scattering and diffraction describe the redirection of X-rays due to the interaction with electrons in the sample. X-ray scattering and diffraction techniques are non-destructive analytical methods which reveal information about the crystallographic structure, chemical composition, and physical properties of the analyzed material on the scale below 100 nm. Scattering and diffraction methods that rely on elastic scattering of monochromatic X-rays are small-angle X-ray scattering (SAXS) and wide-angle X-ray diffraction (WAXD). SAXS is measuring scattering intensities at scattering angles close to 0°, whereas WAXD describes diffraction on scattering angles larger than 5°.

X-ray scattering and diffraction on bone reveals information on the mineral particle size and arrangement (for more details see 2.5.4 Determination of parameters – T-, Rho- and L-parameter).

Figure 2-7 shows a scheme of the elastic scattering principle where the incident X-ray beam is elastically scattered from the bone sample in an angle of 2θ.

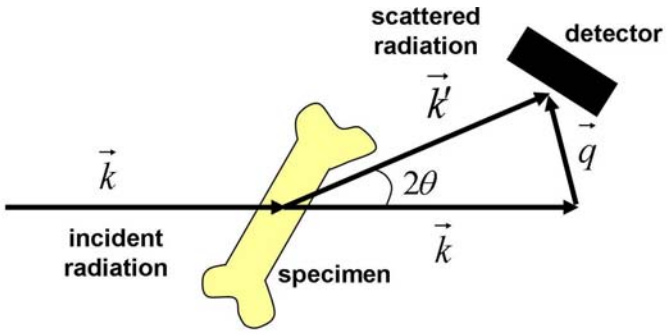

Figure 2-7: Schematic illustration of the elastic scattering principle. The incident beam with wave vector $\vec{k}$ is transmitted though the sample and scattered. The scattered beam with wave vector $\vec{k}'$, scattering angle 2θ and the scattering vector $\vec{q}$ are represented.

For elastic scattering the scattering vector $\vec{q}$ is defined as

$$\vec{q} = \vec{k}' - \vec{k} ,$$

the difference of the wave vectors of the scattered beam ($\vec{k}'$) and the incident beam ($\vec{k}$). Thus, the length $|\vec{q}|$ of the scattering vector $\vec{q}$ is:

$$|\vec{q}| = \frac{4\pi}{\lambda} \sin\theta$$

with a distinct length of the wave vectors:

$$\left|\vec{k}\right| = \left|\vec{k}'\right| = \frac{2\pi}{\lambda}.$$

Periodic structures in the nanometer range within the sample material, such as mineral particles or collagen in bone, lead to periodic reflections. These reflections are called Bragg peaks and are observed in the diffraction pattern. If these crystalline structures are not perfectly ordered, the intensity of the Bragg peaks is diminished, and the width of the peaks increases. The peak position is defined by the crystal lattice of the structure. These reflections can only arise at scattering angles where Bragg's law is valid:

$$n\lambda = 2d \cdot \sin\theta .$$

In this equation n describes an integer, λ the wavelength of the primary beam, d the distance between the lattice planes in the crystal structure and θ is half the scattering angle, called Bragg-angle. The lattice planes can be seen as mirror planes concerning incident and reflected beam, $\vec{n} \| \vec{q}$ (mirror condition) (see **Figure 2-8**).

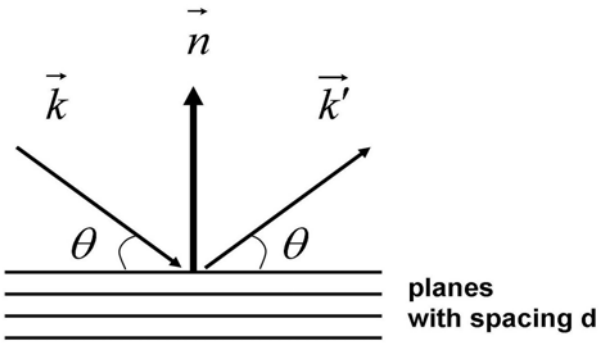

Figure 2-8: Schematic illustration of the lattice planes and the reflected beam. The incident beam with the wave vector $\vec{k}$, the reflected beam with wave vector $\vec{k}'$ and the Bragg-angle θ are shown.

The scattering pattern of an object is the reciprocal "image" of this object. Thus, small distances between scattering centers are influencing the scattering behavior in the range of large angles (WAXD), whereas large distances are influencing the scattering behavior in the range of small angles (SAXS). Any scattering process is characterized by a reciprocity law, which gives an inverse relationship between the particle size and scattering angle [Glatter and Kratky, 1982].

The scattering and diffraction techniques SAXS and WAXD applied to bone give structural information from different length scales. SAXS reveals information on the orientation, size and shape of the mineral particles, whereas WAXD includes information

on the mineral particle length and the degree of crystallinity in the bone sample. Both techniques are described in more detail in the following sections as they play an important role in this study.

2.5.1 Wide-angle X-ray diffraction on bone

Wide-angle X-ray diffraction (WAXD) includes diffraction intensities at scattering angle 2θ larger than 5°. The diffraction peaks result from atoms or molecules ordered in a crystalline lattice. Thus, WAXD includes information about the sub-nanometer range, on the length scale of 0.1 – 1 nm. When X-rays are transmitted through the sample they will diffract in predictable patterns based on the internal structure of the sample (Bragg's law). Bone tissue in general gives characteristic X-ray diffraction patterns containing numerous well-defined wide angle rings. These patterns are derived from the carbonated HA, the mineral component in bone. It has been known for long time that in the patterns of longitudinal bone sections several rings show definite orientation suggesting that the apatite crystals are well oriented in the bone structure [Finean and Engstrom, 1953]. The strongest distinct ring in bone resulting from the diffraction by carbonated HA is that of the (002) lattice planes. The (002) reflection includes information on the orientation of the hexagonal c-axis which in turn allows the determination of the fibril orientation as they are parallel oriented [Landis, Hodgens et al., 1996; Fratzl, Gupta et al., 2004]. Furthermore, the WAXD signals change with crystallinity of the analyzed material. Whereas the WAXD patterns of crystalline materials reveal sharp diffraction peaks, less crystalline materials show broad, diffuse peaks [Olszta, Cheng et al., 2007]. The width of the peaks in the diffraction pattern is dependent on the mineral crystal size, thus the length of the mineral particles can be determined from the WAXD pattern, described by the L-parameter (for more details see chapter 2.5.4 Determination of parameters – T-, Rho- and L-parameter).

2.5.2 Small-angle X-ray scattering on bone

Small-angle X-ray scattering (SAXS) is based on the analysis of the diffuse scattering of the primary X-ray beam at low scattering angles 0.1°-5°. SAXS appears if the irradiated object contains areas in the range of 1 nm to 1 μm, which are different in their electron density. In a two phase system, such as bone, the difference in the average electron density between the particles and the surrounding matrix is leading to X-ray scattering in the typical range of resolution of the SAXS. The difference of the electron densities and thus the scattering length densities of the two phases is referred to as scattering contrast. In bone this contrast arises from the two phases, mineral and collagen, which possess different

electron densities. Besides differing mean electron densities these two phase systems should have sharp interfaces between them [Porod, 1951]. The scattering patterns are depended on the shape and ordering of the mineral particles embedded in the bone matrix resulting in different shaped SAXS signals, mostly ellipses or circles. Anisotropic SAXS signals arise if the analyzed system contains anisotropic inhomogeneities, elongated or flattened, and if they are ordered and show a preferred orientation. The scattering pattern is the reciprocal "image" of the size and the arrangement of the mineral particles in the bone matrix, meaning in case of size, that large dimensions in real space appear small in reciprocal space and vice versa. If the mineral particles in the sample are randomly oriented, the scattering pattern of such a system would be circular, isotropic. SAXS gives information on the mineral thickness, described by the T-parameter, and the orientation of the mineral particles, represented by the Rho-parameter, regardless of whether the sample or particles are crystalline or amorphous (see chapter 2.5.4 Determination of parameters – T-, Rho- and L-parameter for more details) .

2.5.3 Scanning SAXS/WAXD

Due to the hierarchical structure of bone, analyzing this material requires appropriate methods to receive information on different length scales at the same time. Scanning SAXS/WAXD is therefore a powerful approach for detecting local changes in bone material which may vary over the tissue on micrometer length scale [Rinnerthaler, Roschger et al., 1999]. During a scanning SAXS/WAXD measurement the specimen is moved stepwise in x and y, perpendicular to the X-ray beam, while for every step the scattering and diffraction pattern is recorded. By using this technique it is possible to achieve information on two length scales simultaneously. Information in the micrometer range is revealed by scanning an area of the sample, whereas information in the nanometer range can be achieved by analyzing the scattering diffraction measurements at distinct positions in the sample area. For higher resolution experiments than investigations using a laboratory X-ray source, experiments using a synchrotron source with a beam size in the (sub) μm range can be performed [Paris, Zizak et al., 2000]. Furthermore, it is possible to apply additional methods after the measurement since scanning SAXS/WAXD is a non-destructive technique.

2.5.4 Determination of parameters – T-, Rho- and L-parameter

In the following subchapter the state of the art of the determination of different parameters revealed by SAXS and WAXD measurements is explained in detail.

The first step of the data analysis after the SAXS and WAXD measurements is the integration of the two-dimensional (2D) SAXS/WAXD patterns into one-dimensional (1D) data, via binning (summation) of the pixel values from the 2D detector. There are two different standard formats applicable, (i) the radial intensity profile, dependent on the scattering vector $\vec{q}$, and (ii) the azimuthal intensity profile, dependent on the azimuthal angle χ of the 2D data. The radial profile I(q) is calculated by binning all pixels with the same radial distance q to the beam center (see **Figure 2-9**, left). The azimuthal profile I(χ) is determined by binning all pixels with the same azimuthal degree χ with respect to the zero direction (see **Figure 2-9**, right).

From the SAXS measurements two important parameters can be determined. On the one hand the T-parameter, describing the mean mineral particle thickness, and on the other hand the Rho-parameter, describing the degree of alignment of the mineral particles in the irradiated sample volume.

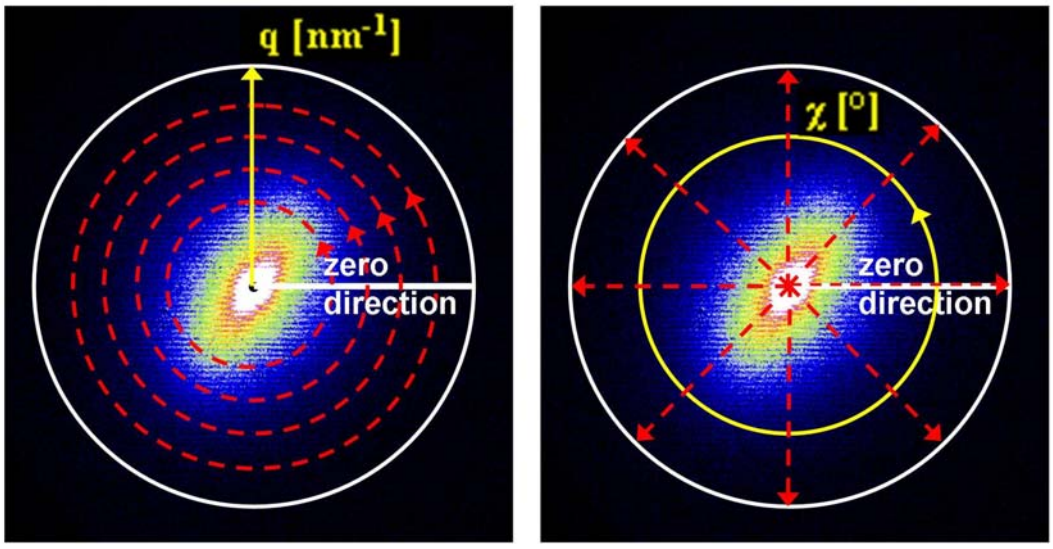

Figure 2-9: Two data integration standards. Left: Radial integration scheme. Pixels with a certain radial distance (q, yellow arrow) from the beam center are depicted by the dashed red circles. Binning of all pixels with the same radial distance, represented by one dashed red circle, was performed with AutoFit. Right: Azimuthal integration scheme. Pixels with a certain azimuthal degree (χ, yellow circle) with respect to the zero direction (white horizontal line) are shown by the dashed red arrows. Binning of all pixels with the same azimuthal degree, represented by one dashed red line, was performed using AutoFit. Adapted from [Zander, Li et al., 2010].

T-parameter: mineral particle thickness

To calculate the T-parameter, the 2D SAXS patterns are radially integrated by a mathematical procedure based on Porod's law. Porod´s law is valid for a two phase system with sharp interfaces between the two phases. This procedure is described in detail previously [Fratzl, Fratzl-Zelman et al., 1991; Rinnerthaler, Roschger et al., 1999].

Porod´s law says that the scattering curve of a two phase system responds always to P/q^4, meaning that the scattering intensity decreases with q^{-4}. This is described by

$$I(q) = \frac{P}{q^4} + B \qquad \text{, for } q \to \infty ,$$

where P represents the Porod constant and B the constant background. These parameters can be determined from the so-called Porod-Plot (see chapter 3.2.3.2 Data evaluation).

One definition of the T-parameter in literature is [Rinnerthaler, Roschger et al., 1999]:

$$T = \frac{4\Phi(1-\Phi)}{\sigma},$$

with Φ describing the total volume fraction of the mineral in the bone tissue and σ displaying the total surface area of the mineral particles per unit volume. From the T-parameter only, it is not possible to get information about the mineral particles shape without additional information. However, since mineral crystals in bone are supposed to be thin platelets [Fratzl, Gupta et al., 2004], T is a measure for their average thickness. In the range of large q values the slope of the logarithmic plot of I(q) should be around -4, if the mineral particles in the sample are platelets (see **Figure 2-10**). In this so-called Porod region of the I(q) curve Porod's law is valid and is used for the data analysis procedure. Furthermore, regions without Bragg reflections have to be used for T-parameter calculation.

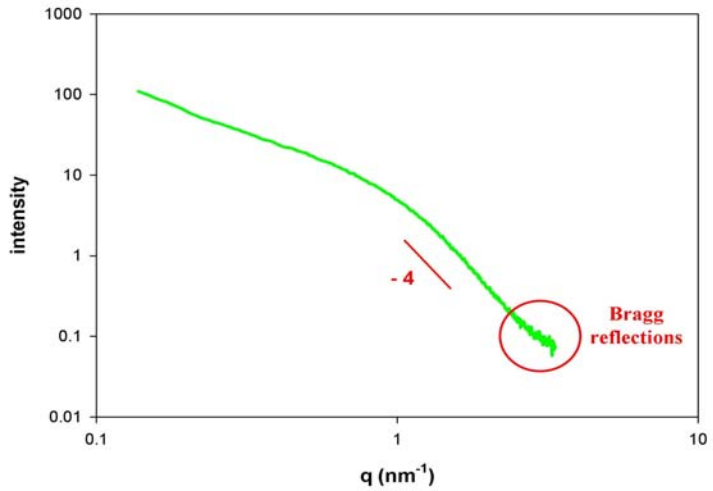

Figure 2-10: Representative log-log plot of a bone sample. log-log plot of I(q), showing the slope of -4, indicating platelet shaped mineral particles, and the Bragg reflections, both highlighted in red.

Another definition of the T-parameter is

$$T = \frac{4}{\pi} \cdot \frac{\bar{I}}{P},$$

with $\bar{I}$ representing the area integration of the $Iq^2(q)$ curve, the so called Kratky-plot, and P displaying the Porod constant, determined from the $Iq^4(q^4)$ curve, the so called Porod-plot (see chapter 3.2.3.2 Data evaluation).

Rho-parameter: mineral particle orientation

The degree of alignment of the mineral particles can be determined after azimuthal integration of the 2D SAXS data [Fratzl, Schreiber et al., 1996; Rinnerthaler, Roschger et al., 1999]. The Rho-parameter characterizes the percentage of aligned particles present in the irradiated sample volume. Depending on the orientation of the mineral particles within the plane perpendicular to the primary beam, the scattering patterns differ qualitatively. If the mineral particles are aligned perfectly parallel, the pattern shows a narrow streak perpendicular to the long axis of the mineral particles. If the particles are oriented randomly, the SAXS pattern is circular, isotropic. Elliptical SAXS patterns are the result of partially aligned mineral particles, already revealing the preferred orientation of the mineral particles with the long axis of the ellipse being perpendicular to the mineral orientation. The azimuthal plot $I(\chi)$ shows two peaks separated by 180° (see chapter 3.2.3.2 Data evaluation). The total area under the $I(\chi)$ curve is the sum of the area under the peaks, which is proportional to the fraction of aligned particles, and the area under the constant background, which is proportional to the fraction of randomly oriented particles in the sample. The ratio of the area under the peaks and the area under the background describes

the Rho-parameter. Rho equals 0 indicates no predominant orientation of the mineral particles, whereas Rho equals 1 indicates perfect parallel alignment of the mineral particles.

Besides the SAXS signal, the WAXD patterns can be used to determine additional information on the mineral particles of the irradiated sample volume. The WAXD pattern of bone includes the (002)-peak resulting from the diffraction by crystalline HA. The intensity of the (002)-peak is proportional to the amount of HA in the sample. Furthermore, analyzing the width of the (002)-peak reveals information about the length of the mineral particles, denoted by the L-parameter.

L-parameter: mineral particle length

The width of the (002)-peak in the diffraction pattern of bone is dependent on the crystal size in the sample. Decreasing crystal sizes lead to a broadening of the peaks (in X-ray diffraction) as is explained by the Scherrer Equation:

$$L = \frac{k\lambda}{B\cos\theta},$$

where L describes the crystal length, B the full width at the half maximum (FWHM) of the (002)-peak, k is constant related to the crystallite shape (in the range of 0.87 - 1.0), called shape factor, and θ represents the Bragg angle.

After radial integration of the 2D WAXD pattern the mean crystallite length, the L-parameter, can be calculated [Klug and Alexander, 1974; Barret, Cohen et al., 1986; Danilchenko, Kukharenko et al., 2002] using Scherrer's equation. The peak width is inversely proportional to the mean crystallite length. The broadening, B, of the HA (002)-peak, fitted by a Gaussian function, which is experimentally measured, is expressed as a squared sum function of two main contributions, according to $B^2 = B_L{}^2 + B_I{}^2$, where B_L represents the crystallite length contribution to the peak broadening while B_I is the instrumental broadening contribution. Therefore, the mean crystallite length contribution is obtained according to

$$B_L = \sqrt{B^2 - B_I{}^2}\ .$$

The instrumental broadening contribution on the HA crystallite is determined by the measurement of HA powder, a calibration standard, on the (002)-peak width. Measured

(002)-peak widths are corrected with respect to the instrumental broadening contribution using the above mentioned equation.

3 Materials and Methods

Microscopically devices and X-ray diffraction methods, both requiring particular sample preparation and specific experimental setups, have been used to analyze and understand the natural and artificially induced bone development. This chapter describes and explains the sample preparation methods, experimental setups and techniques as well as data evaluation procedures.

3.1 Bone samples

In this study different types of developing bone samples have been investigated to analyze bone development under various conditions. On the one hand, long bones of wild type and genetically modified mice have been examined, to understand the natural bone development and the influence of genetic modifications on bone development, respectively. On the other hand, bone formed in scaffolds during healing implanted in pig has been analyzed to understand the artificially induced bone development. The methods used in this study were performed on embedded samples thus a special sample preparation ahead the experiments was carried out as will be described in the following.

3.1.1 Natural bone samples

Natural bone development in growing bones was analyzed using long bones, in particular tibiae and femora, of wild type mice at different developmental stages. Tibiae and femora were obtained from male mice strain C57BL/6, a strain frequently used in bone research and therefore qualified to establish baseline data on bone development in normal (wild type) mice. Mice were kept under standard housing conditions. The sacrificing of transgenic mice was permitted by the "Landesamt für Gesundheit und Soziales" (LAGeSo), Berlin. The animal facility at the Max Planck Institute of Molecular Genetics (MPIMG, Berlin, Germany) possesses an approval for breeding and animal husbandry of laboratory mice. Fetal stages (F), day 14.5, 16.5 and 18.5 after conception, as well as postnatal stages (P), day 1, 7 and 21 after birth, have been investigated, 5 tibiae and femora per age. The different investigated developmental stages in mice are illustrated in **Figure 3-1.** The investigated mouse strain exhibits a 19-day gestation.

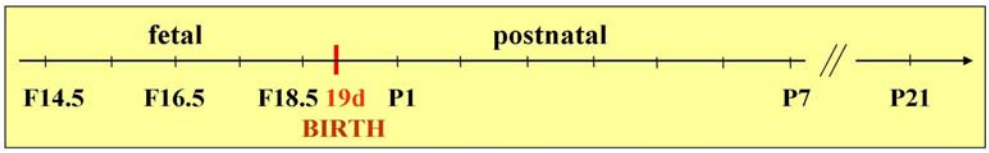

Figure 3-1: Different developmental stages of mice. Time scale illustrating the developmental stages analyzed in this study to investigate the normal bone development in mice from fetal (F) to postnatal (P) stages of bone development.

After dissection at the MPIMG, murine tibiae and femora were fixed in 4% paraformaldehyde (PFA) for 24 hours, washed in phosphate buffered saline and dehydrated in a graded series of ethanol solutions, 70%, 80%, 90% and 100% ethanol for 24 hours each concentration. Thereafter the dehydration was finished by transferring the samples into acetone/ethanol (1:1) and to 100% ethanol for another 24 hours. Subsequently the samples were treated two times for two hours with xylene, followed by the storage in methylmethacrylate (MMA) infiltration solution for two times 24 hours to remove the alcohol. Afterwards the bones were embedded in polymethylmethacrylate (PMMA) at the MPIMG using N,N-Dimethyl-p-toluidine (DMPT) activated MMA solution. Tibiae and femora were arranged and fixed in moulds which were filled with the activated MMA solution containing 50 ml MMA and 200 µl DMPT. The polymerization proceeded at 4°C. For histological investigations 5 µm slices were taken from the blocks, parallel to the longitudinal axis of the bone, using a microtome (RM2255, Leica, Wetzlar, Germany). At the Max Planck Institute of Colloids and Interfaces (MPIKG, Potsdam, Germany) the sample blocks with the embedded bones were cut parallel to the longitudinal axis of the bone to expose a longitudinal section of the entire bone, of both tibia and femur, using a low speed diamond saw (Buehler Isomet, Buehler, Düsseldorf, Germany) under constant water irrigation (see **Figure 3-2**, a). The surface of the sample blocks, containing the truncated bone, was polished to mirror finish (PM5, Logitech, Glasgow, Scotland) to ensure the absence of scratches for further investigations in the environmental scanning electron microscope (ESEM). Therefore, different grades of abrasive paper, 1200 with grading of 15 µm, 2500 with grading of 11 µm and 4000 with grading of 5 µm, were successively used for several minutes, followed by polishing with 3 µm and 1 µm diamond spray on a cotton cloth and a foulard, respectively. For SAXS measurements in the laboratory sections of the bone were cut head on from the sample blocks, using a low speed diamond saw (Buehler Isomet, Buehler, Düsseldorf, Germany) under constant water flow. Afterwards parallel slices of 200 µm thickness containing the whole longitudinal-sectional area of the bone were produced by grinding using 1200 abrasive paper (PM5, Logitech, Glasgow, Scotland). The position of a longitudinal bone section with respect to the X-ray beam in the X-ray scattering and diffraction experiments is shown in **Figure 3-2**,

b. For measurements at the synchrotron facility 50 µm slices were produced. Due to time constraints at the synchrotron facility BESSY II ("Helmholtz-Zentrum Berlin für Materialien und Energie", Berlin, Germany), it was not possible to measure the whole set of samples, investigated with the laboratory equipment. Hence, only tibiae at fetal stage F16.5 and postnatal stages P1, P14 and P42 have been analyzed.

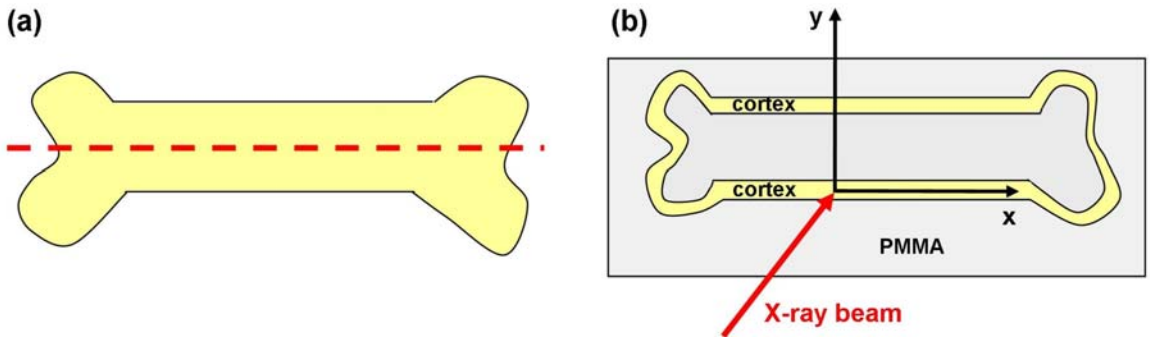

Figure 3-2: Schematic drawing of the cutting and scanning directions of the bone samples. (a) The dashed red line depicts the cutting plane parallel to the longitudinal axis of the bone, side view. (b) Longitudinal section of the bone embedded in PMMA and its geometry in an X-ray experiment with the X-ray beam direction, front view.

3.1.2 Bone samples of NF1 mice

To investigate the influence of genetic modifications on bone development mice of the same strain as the wild type mice, C57BL/6, were used to develop a mouse line with an inactivation of one specific gene, so called knockout of a gene. Mice analyzed in this study exhibit a knockout of the gene for neurofibromin 1, which led to the disease NF1. This knockout of the Nf1 gene function was specifically in the limbs. Due to the fusion of the knee joint as one appearance of the NF1 phenotype, these mice were not able to use their hind limbs properly, they could only move by using their fore limbs. Thus, instead of tibiae and femora we studied humeri of NF1 mice to exclude a bone phenotype, which was maybe only caused by missing mechanical loading and not by genetically modification. Humeri at postnatal stages P15, P42 and 3 month after birth, were dissected and afterwards treated in the same way as tibiae and femora of the wild type mice (see chapter 3.1.1 Natural bone samples). Bones were embedded in PMMA at the MPIMG and investigated using SAXS and the ESEM at MPIKG. Mice exhibiting a knockout of the Nf1 gene function, thus showing characteristics of NF1, are abbreviated NF1 mice in the following.

3.1.3 Artificially induced bone samples

The samples to investigate developing bone during healing were produced at the Institute of Health and Biomedical Innovation at the Queensland University of Technology (QUT, IHBI, Brisbane, Australia). At the QUT, IHBI after anesthesia of the pig two critical size defects (35x17x10 mm^3) were made on either side of the sagittal suture in the calvarial bone (see **Figure 3-3**). Scaffolds of 80wt% polycaprolactone (PCL) and 20wt% tricalcium phosphate (TCP) have been implanted into the defect sites either alone or in combination with bone marrow stem cells (BMSCs), which were added by using fibrin glue (TISEEL kit, Baxter AG). BMSCs were obtained from the same animals under general anesthesia using routine bone marrow extraction. Per scaffold 22 million cells were transferred immediately prior the implantation of the scaffold into the defect site. The pigs were euthanized two years after implantation of the scaffold. The scaffold and the entire surrounding skull were explanted and fixed in 4% PFA for 2 weeks. Afterwards the samples were dehydrated using graded series of ethanol, 70% ethanol for one week, 80%, 95% and 100% ethanol for 3 days each concentration. Subsequently the samples were processed three times in xylene for two days each, under vacuum pumping (400bar), followed by the infiltration with MMA for 2 days and embedding at room temperature in MMA containing 0.25% perkadox and 5% dibutyl phthalate. The resin blocks were sawed in half, directly through the center of the scaffold to facilitate slicing from the center of the scaffold. For histological investigations 6 µm slices were produced using an osteomicrotome (SM2500, Leica Microsystems, Wetzlar, Germany). At the MPIKG the sample blocks were polished to a mirror finish (PM5, Logitech, Glasgow, Scotland), as described in chapter 3.1.1 Natural bone samples, for further investigations with the ESEM. For SAXS investigations in the laboratory sections of the scaffold and the surrounding calvaria, the flat bone of the skull, were cut head on from the resin blocks using a low speed diamond saw (Buehler Isomet, Buehler, Düsseldorf, Germany) under constant water irrigation. These sections were ground (PM5, Logitech, Glasgow, Scotland) to receive parallel slices of 200 µm thickness, containing the entire scaffold and the adjacent calvaria.

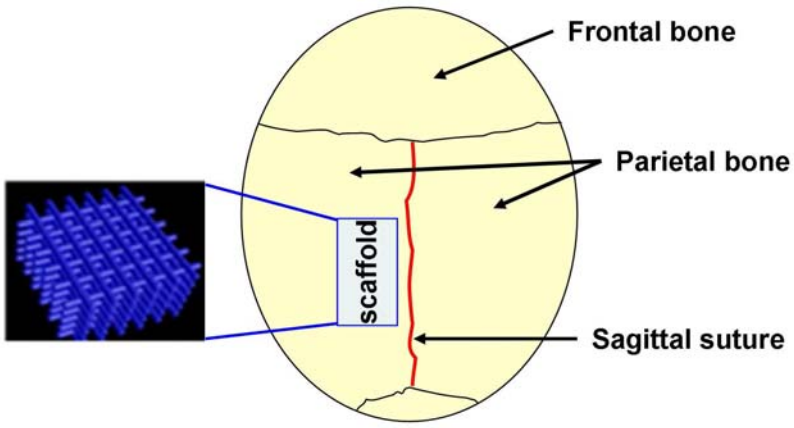

Figure 3-3: Schematic drawing of the skull and the implanted scaffold, top view. The bone of the skull is called calvaria, besides others made up of the frontal and the parietal bone and the sagittal suture. The sagittal suture is depicted in red. On either side of the suture critical size defects were made and PCL-TCP scaffolds were implanted for 2 years. A scaffold implant is depicted by the blue box, demonstrating the position of implantation. The architecture of the scaffold is represented in the black box on the left.

3.2 Characterization

The analysis of bone development was done on the embedded samples using different non-destructive methods to investigate the same sample with various techniques. Thereby, information on different length scales, meaning information on different hierarchical levels of the bone, could be achieved. Analysis of the micrometer level was performed by microscopic techniques and scanning X-ray diffraction experiments facilitating predications on the tissue arrangement and the tissue and cell level of bone. Examinations on the nanometer scale were possible using X-ray diffraction experiments, providing information on the mineral particle level in bone.

3.2.1 Staining protocols for histology

3.2.1.1 Von Kossa/Toluidin

Longitudinal sections of tibiae and femora of mice were histologically investigated using Von Kossa/Toluidin staining at the MPIMG, a standard staining for bone sections revealing mineralized tissue in black and cartilage in purple. Bone slices were deplastified in 2-methoxyethyl-acetate (2-MEA, Merck, Darmstadt, Germany) 3 times for 10 min each, followed by 2 times xylene 3 min each. Afterwards the slices were hydrated using descending concentration of ethanol, 100%, 90%, 80%, 70% and 50% ethanol for 1 min each and following rinsed for 5 min in water and 5 min in distilled water. For Von Kossa staining the slices were stained in 1% silver nitrate solution in distilled water ($AgNO_3$,

Sigma, St. Louis, USA) for 2 min. Thereafter the slices were rinsed with distilled water 3 times for 1 min each, followed by 2 min incubation in 5% sodium carbonate/10% formaldehyde solution, to develop the staining by chemical reduction of the mineral attached silver ions. The sodium carbonate-formaldehyde solution was produced by dissolving 15 g sodium carbonate in 225 ml distilled water and 75 ml 37% formaldehyde solution (Na_2CO_3 water free, Merck; 37% formaldehyde solution, drugstore product). Afterwards the slices were rinsed for 10 min in running tap water and incubated in 5% disodiumthiosulfate solution in distilled water for 10 min, to remove unreduced silver by complexation, followed by 10 min in running tap water. For Toluidin staining the slices were incubated in 0.05% Toluidinblue solution for 5 min. The staining solution was produced by dissolving 0.5g Toluidinblue O (Sigma, St. Louis, USA) in 100 ml distilled water, followed by filtration. Thereafter, the slices were shortly rinsed with distilled water, followed by a graded series of ethanol, 70% and 90% ethanol short and 100% ethanol 2 times for 2 min. During the series of ethanol the slices were little discolored and thereby the staining was differentiated. Finally, the slices were transferred to xylene 2 times for 5 min, mounted with Entellan and photographed using a light microscope (BX60, Olympus, Hamburg, Germany).

3.2.1.2 MacNeal

Slices of the PCL-TCP scaffolds and the adjacent porcine calvaria, explanted 2 years after implantation, were stained using MacNeal's stain at the QUT, IHBI. MacNeal is a staining method suitable for bone sections revealing mineralized tissue in black and non-mineralized collagen and non-collagenous proteins (such as unmineralized bone/osteoid) in a light blue color. Therefore, slices were deplastified in acetone for 1 hour and hydrated in descending ethanol concentration, 100%, 95% and 70% ethanol for 5 min each concentration. Afterwards the slices were rinsed in deionized water for 5 min and stained with silver nitrate solution (Fisher, Schwerte, Germany) for 5 min. The staining solution was prepared by dissolving 20 g of silver nitrate in 400 ml distilled water. Thereafter, the slices were rinsed 3 times in deionized water for 1 min each and the staining was developed in sodium carbonate-formaldehyde solution (Fisher, Schwerte, Germany) via reduction of silver ions. The sodium carbonate-formaldehyde solution was prepared by mixing 22.5 g of sodium carbonate, 112.5 ml formaldehyde and 337.5 ml distilled water. Subsequently, the slices were rinsed 2 times with deionized water for 1 min each and submerged in fresh Farmers diminisher solution (Fisher, Schwerte, Germany). Therefore, 2 g potassium ferricyanide and 40 g sodium thiosulfate were dissolved in 420 ml distilled water. Slices were washed in running tap water for 20 min and stained with MacNeal's

tetrachrome for 5 min. This staining solution consisted of 16 g MacNeal's tetrachrome in 600 ml distilled water. Afterwards the slices were rinsed in deionized water for 30 sec and dehydrated in 70% and 100% ethanol for 30 sec each, followed by two changes of xylene (Fisher, Schwerte, Germany) for 3 min each. Finally, the slices were mounted using Eukitt mounting media (Calibrated Instruments, Singapore).

3.2.2 Microscopy

3.2.2.1 Light microscopy

After histological staining the bone sections were examined using a light microscope (BX60, Olympus, Hamburg, Germany) and photographed with a digital camera (AxioCam HRc, Zeiss, Jena, Germany). The images were processed using suitable software (AxioVision, Zeiss, Jena, Germany). To receive an overview of the entire sample 4 x magnifications was used. For detailed images of regions of interest 20 x magnifications was used.

3.2.2.2 Environmental scanning electron microscopy

The ESEM is a special form of a scanning electron microscope (SEM) that allows a gaseous environment in the sample chamber instead of vacuum in the standard SEM. This change in the experimental environment leads to several advantages compared to the standard SEM, for instance the possibility (i) to examine hydrated specimens or (ii) to investigate electrically non-conductive specimens without coating with gold or carbon. The latter is a main advantage for this study by reason of avoiding the interference of the coating in X-ray diffraction experiments if using the same sample.

In the ESEM the electron beam (primary electron beam) is scanned over the sample and the electrons of the beam are interacting with the sample surface, thereby producing several signals that are collected with appropriate detectors. One possible detector in the ESEM is a secondary electron (SE) detector. Secondary electrons reveal information on the surface topography. In addition it is possible to detect backscattered electrons using a backscattered electron (BSE) detector. In the experimental setup of this study a BSE detector was used in the ESEM. Backscattered electrons are electrons that are scattered back by the primary electron beam in a region close to the surface of the bone sample. The number of electrons backscattered from the sample surface is related to the atomic number of the atoms hit by the beam. The higher the atomic number, the higher is the number of backscattered electrons. In bone the essential components of the organic matrix are

hydrogen, carbon, nitrogen, oxygen, phosphorus and sulfur, the essential constituents in the mineral phase are calcium, phosphorus, oxygen, hydrogen, carbon and magnesium. Therefore, the concentration of calcium, the component with the highest atomic number, dominantly influences the intensity of the backscattered electrons. The higher the calcium concentration in an area of the sample, the higher is the number of electrons scattered back from that area of the sample, detected as brighter gray values [Roschger, Fratzl et al., 1998]. Hence the ESEM image consists of different gray levels correlated with the calcium content. It is thus possible to visualize local changes of the mineral concentration in the sample with the ESEM.

To investigate bone samples with the ESEM (FEI-Company, Oregon, USA) it was necessary to polish the surface to mirror finish to avoid a rough and scratched sample surface. The polished sample blocks were investigated in low vacuum (0.75 Torr) using BSE mode at a working distance of 10 mm. The electron beam energy was set to be 10 kV. A solid state detector (SSD) was used to measure the BSE signal from the sample surface. In the resulting gray level images of the mineralized bone tissue regions of high calcium content appeared bright gray, whereas regions of low calcium content showed up in dark gray, representing high and low mineral concentration in the bone sample, respectively.

3.2.3 Small-angle X-ray scattering – measurement routine

SAXS denotes the diffuse elastic scattering of X-rays at low scattering angles by for example particles or pores. In this study bone has been analyzed, thus in the SAXS experiments the scattering of the mineral particles in bone has been measured. The scattering intensity and the scattering distribution around the incident X-ray beam provided information about the size and the arrangement of the mineral particles in the bone neglecting, whether these particles were crystalline or amorphous. Murine bones and tissue engineered bone in scaffolds, implanted in pig, have been investigated to study natural bone development and artificially induced bone development, respectively. Some embedding materials can cause diffraction peaks and thereby interfere the data analysis. PMMA is not producing an interfering signal in the corresponding q-region and was thus a suitable embedding material for X-ray experiments.

3.2.3.1 Experimental setup

In the laboratory SAXS equipment (see **Figure 3-4**) – a Bruker Nanostar – an X-ray generator (Bruker, AXS, Karlsruhe, Germany) with a rotating copper anode operating at 40 kV / 100 mA was used to produce an X-ray beam with a wavelength of $\lambda = 0.154$ nm. The

Nanostar was optimized for SAXS measurements on bone with a q range between 0.21 nm^{-1} and 3.2 nm^{-1}. The diameter of the beam at the sample was approximately 200 µm and the sample-to-detector distance was 625 mm. Slices of the embedded bone samples with a thickness in the order of the beam size (around 200 µm) were mounted on a sample holder, which could be moved automatically with a precision of 2 µm in the plane perpendicular to the incident beam, thus scanning SAXS experiments over the entire bone sample were possible. The sample chamber was kept under vacuum during the measurements. To image the sample in order to determine the positions of the subsequent SAXS measurements, an X-ray transmission image of the bone samples, called radiography (see **Figure 3-4**), was produced. Therefore, the X-ray absorption of the sample was measured every 100 µm using a diode. The SAXS signal was measured every 300 to 400 µm depending on the sample size using a 2D area detector (Bruker, Karlsruhe, Germany). The obtained SAXS pattern (see **Figure 3-4**) represented the intensity distribution scattered around the primary beam which was passed through the bone sample for 1 hour.

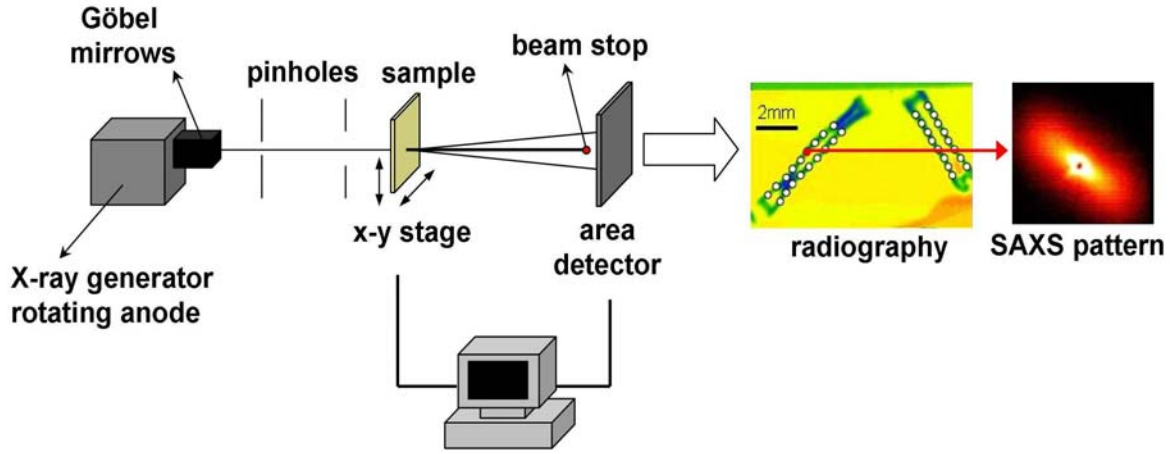

Figure 3-4: Scheme of the experimental setup in the laboratory showing the important elements in an X-ray scattering experiment. On the right side a radiography of a tibia (left) and a femur (right) is shown with selected measuring positions, highlighted by white dots. Aside the SAXS pattern of one measuring position, marked by a red dot in the radiography, is shown.

3.2.3.2 Data evaluation

Data pre-treatment

Before starting a SAXS measurement it was required to measure the SAXS signal of Silver Behenate (AgBh), a standard to calibrate the x and y coordinates of the beam center and the sample-to-detector distance for each measurement using the specially designed softwares Fit2d [Hammersley, 1997] and AutoFit (custom made software developed at the MPIKG), respectively. As a next step prior the SAXS measurement the X-ray transmission of the sample was measured using a diode, leading to an X-ray image of the sample

facilitating the definition of measuring positions of the SAXS measurements. Using the X-ray transmission the transmission coefficient, T_{sample}, at each measuring position could be calculated, by estimating the ratio of the transmission of the sample, I_{t_sample}, and the intensity of the incoming beam without the sample, the empty beam (EB), I_{t_EB}, measured with a diode,

$$T_{sample} = \frac{I_{t\_sample}}{I_{t\_EB}}.$$

Besides the measurement of the SAXS intensity, measured with the detector and without a diode, at the measuring positions of the sample, it was necessary to measure the intensity of the EB, generated without the sample in the beam. This was done after every measurement to correct the SAXS intensities of the sample for background scattering as follows:

$$I_{corr} = \frac{1}{T_{sample}} \cdot I_{sample} - I_{EB}$$

Using this formula the measured intensity of the sample was corrected, with T_{sample} representing the transmission coefficient at a position on the sample, I_{sample} means the measured SAXS intensity of that position on the sample and I_{EB} is the SAXS intensity of the EB. I_{corr} was calculated automatically during the analysis with AutoFit after the input of the transmission coefficients, the SAXS measurements of the sample and the EB.

Data analysis

As described in section 2.5.4 Determination of parameters – T-, Rho- and L-parameter, radial integration of the 2D SAXS patterns into 1D data was used to calculate the mean mineral crystal thickness, the T-parameter, whereas the azimuthal integration of the 2D SAXS patterns was used to estimate the degree of alignment of the mineral particles, the Rho-parameter.

The T-parameter could be calculated with the help of the analysis software AutoFit using the following equation:

$$T = \frac{4}{\pi} \cdot \frac{\bar{I}}{P},$$

where $\bar{I}$ represents the area integration of the Kratky-plot (see **Figure 3-5**, right) and P displays the Porod constant, determined from the Porod-plot (see **Figure 3-5**, left).

Both, the radial integration of the 2D data and the calculation of the T-parameter, were done using AutoFit. However, for a couple of measuring positions the T-parameter was determined using the software Sigma Plot to recheck the software results. To perform an accurate analysis of the T-parameter several parameter had to be assessed. These values, q_{Kratky}^{min}, q_{Porod}^{min} (q_P^{min}), q_{Porod}^{max} (q_P^{max}), had to be defined for every measurement using the Kratky- and the Porod-plot (see **Figure 3-5**). q_P^{max} should be as large as possible but without bad statistics or Bragg reflections, q_P^{min} should be as small as possible but still within the region of a -4 slope in the logarithmic I(q) plot (see **Figure 2-10**). For the laboratory measurements $q_{Kratky\ min}$ should be bigger than 0.2 nm^{-1}, to be outside of the beam stop.

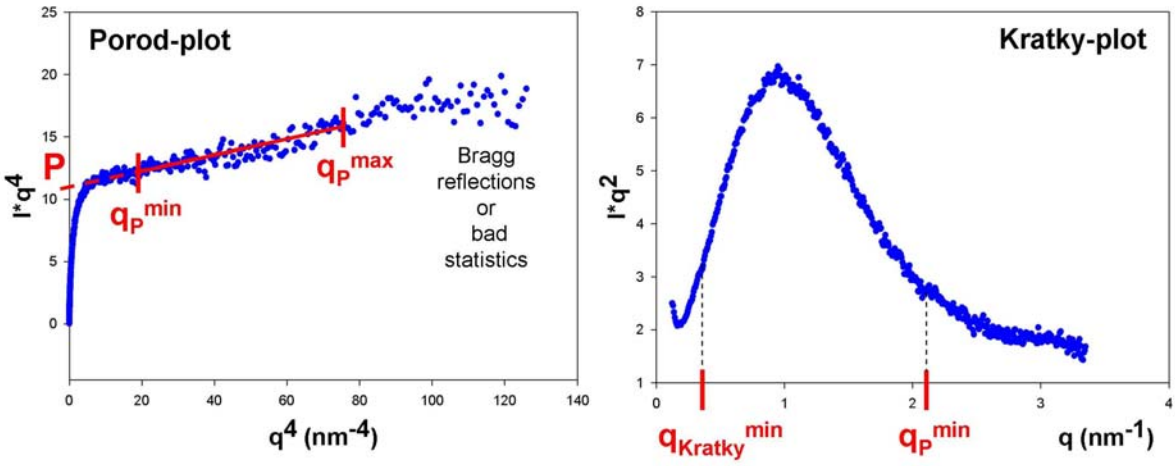

Figure 3-5: Porod- and Kratky-plot of bone. Left: Porod-plot, showing the porod region, defined by red lines representing the parameters for the T-parameter calculation q_P^{min} and q_P^{max}. The Porod constant P is defined by the intercept of the fit of the porod region with the y-axis (dashed red line). Right: Kratky-plot, showing the parameters q_{Kratky}^{min} and q_P^{min}.

The calculation of the Rho-parameter was done after azimuthal integration of the 2D SAXS patterns, as described in chapter 2.5.4 Determination of parameters – T-, Rho- and L-parameter. The azimuthal plot I(χ) showed two peaks separated by 180° (see **Figure 3-6**). The total area under the I(χ) curve is the sum of the area under the peaks, A_1 and A_2, which was proportional to the fraction of aligned particles, and the area under the constant background (baseline), B, which was proportional to the fraction of randomly oriented particles in the sample (see **Figure 3-6**). The Rho-parameter could be calculated by:

$$Rho = \frac{A_1 + A_2}{A_1 + A_2 + B}.$$

The azimuthal integration was done by AutoFit. The Rho-parameter was calculated with the help of an excel macro (developed by M. Rüggeberg, refined by A. Märten, MPIKG, Berlin, Germany) by integrating the area under peaks and the baseline.

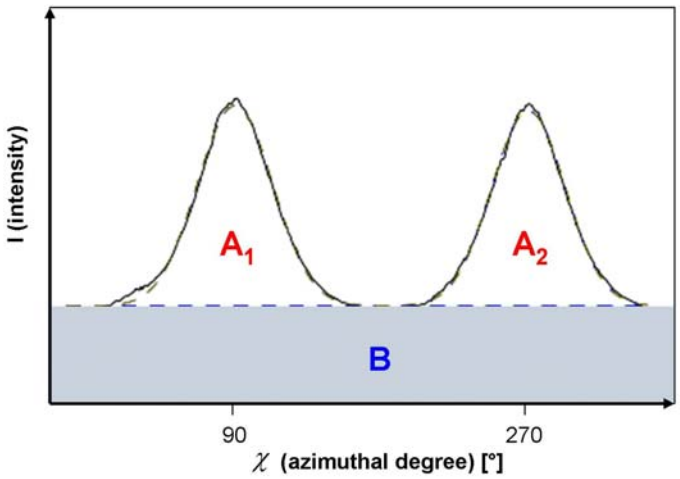

Figure 3-6: Azimuthal plot I(χ). A_1 and A_2 depict the area under the peaks, proportional to the number of aligned mineral particles in the sample. B represents the area under the baseline (dashed blue line), proportional to the number of randomly oriented mineral particles in the sample.

3.2.4 SAXS/WAXD with synchrotron radiation – measurement routine

X-ray diffraction measurements on wild type mice bone were carried out at the synchrotron beam line µ-Spot at BESSY II. Its important advantages compared to the laboratory equipment were, (i) a higher resolution of the measurements due to the small beam size of 30 µm, (ii) the possibility to measure SAXS and WAXD concurrently and (iii) the potential to detect very low amounts of mineral due to the possibility to simultaneously measure the X-ray fluorescence (XRF) of calcium in the sample. Besides the thickness of the mineral particles and their degree of alignment, revealed from the SAXS signal, the calcium content in the sample could be determined from the calcium XRF signal and the amount of carbonated HA in the sample and the length of the mineral particles could be obtained using the (002)-peak of the WAXD pattern of bone resulting from the diffraction by crystalline HA. The WAXD signals of bone can reveal information about the degree of crystallinity of the mineral in the sample. Of special interest was the possibility to directly correlate the amount of calcium of the bone sample with the HA content at one distinct position of the sample due to the possibility of XRF measurements directly during the measurements. This specific setup opened new possibilities of the data analysis.

3.2.4.1 Experimental setup

The experimental setup at BESSY II is simplified shown in **Figure 3-7** and includes a pinhole-defined microbeam, the sample stage, an optical microscope (Infinity Optical, Boulder, USA) with a resolution of 2.2 µm and the 2D position-sensitive CCD-detector (MarMosaic 225, Mar USA Evanston, USA), an area detector with a pixel size of 73.242 x 73.242 μm^2. The beam size at the sample was approximately 30 µm with a wavelength of λ = 0.082656 nm. The sample stage consisted of a xyz translation stage. The sample was moved in x and y direction perpendicular to the incident beam. Thus, scanning measurements of the long bones were possible. The CCD-detector could be moved along the beam direction to maximize the accessible q range. The measurements were carried out in air using a sample-to-detector distance of 314 mm for an optimized q range to determine both SAXS and WAXS concurrently. For simultaneous SAXS, WAXD and XRF measurements, as conducted in this study, there was an additional fluorescence detector (ASAS-SDD, KETEK Germany) with a 100 mm^2 sensitive area and about 167.4 eV energy resolution. In order to detect the bone sample and define regions of interest, a calcium distribution map of the sample was created using the XRF signal of calcium. On 50 µm slices linear scans were performed with a step size of 30 µm between the measuring positions, with a measuring time of 60 sec at each position.

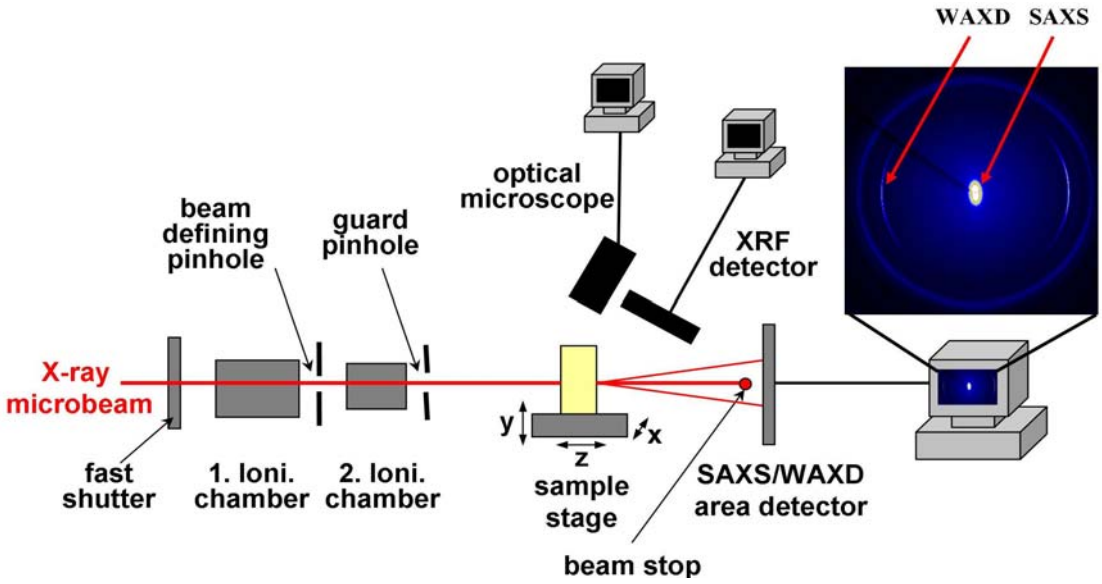

Figure 3-7: Simplified scheme of the experimental setup at the µ-Spot synchrotron beam line at BESSY II (Berlin, Germany), showing the important elements in an SAXS/WAXD/XRF experiment. Aside an example of a scattering pattern of bone is shown, including both SAXS and WAXD signals.

3.2.4.2 Data evaluation

Data pre-treatment

Calibration of the beam center and the sample-to-detector distance was done using Fit2d and AutoFit respectively using the diffraction pattern of HA powder.

After every SAXS measurement, with the detector and without the pin-diode, the EB had to be measured, to correct the measurements for background scattering. Furthermore, between the measurement the dark current (DC) had to be measured, meaning that the beam shutter was closed to measure the electronic noise from the detector. The corrected SAXS intensity for each measuring position could be calculated using:

$$I_{corr} = \frac{1}{T_{sample}} * (I_{sample} - I_{DC}) - (I_{EB} - I_{DC}).$$

I_{corr} was calculated using AutoFit after the input of the transmission coefficients and the measurements of the sample, the EB and the DC.

Data analysis

The analysis of the SAXS signals was done as described in chapter 2.5.4 Determination of parameters – T-, Rho- and L-parameter. But one important difference, compared to the analysis of the laboratory measurements, was that the beam stop and the capillary anchoring it had to be excluded from the region of azimuthal integration by masking. The mask was designed using Fit2d and used in the analysis with AutoFit. Besides the SAXS signal, the XRF signal of calcium and the (002)-peak of the WAXD pattern of HA, have been analyzed.

SAXS

The T-parameter was determined as described for the laboratory SAXS data in section 3.2.3.2 Data evaluation. One difference concerning the T-parameter evaluation was the parameter q_{Kratky}^{min} which should be bigger than 0.3 nm^{-1} for the synchrotron measurements due to the beam stop. The Rho-parameter was calculated with AutoFit using Gaussian fitting of the I(χ) curve.

X-ray fluorescence of calcium

Prior the SAXS/WAXD measurements the calcium XRF signal in the range of 3.32 keV and 4.26 keV was measured using an additional fluorescence detector (ASAS-SDD,

KETEK Germany) to detect even very low amounts of mineral, which were not visible in the radiography. Therefore, the integrated XRF signal of calcium was plotted against the corresponding position. Thus, a calcium distribution map of the sample could be created which was used to select the positions of the following SAXS/WAXD measurements (see **Figure 3-8**). Simultaneously to the SAXS/WAXD measurements, an XRF spectrum was recorded for every scan point and saved as a separated file. Especially the integrated XRF signal of calcium was recorded for every measuring position as a measure of the calcium content of the sample, enabling the correlation with the SAXS/WAXD data at that position.

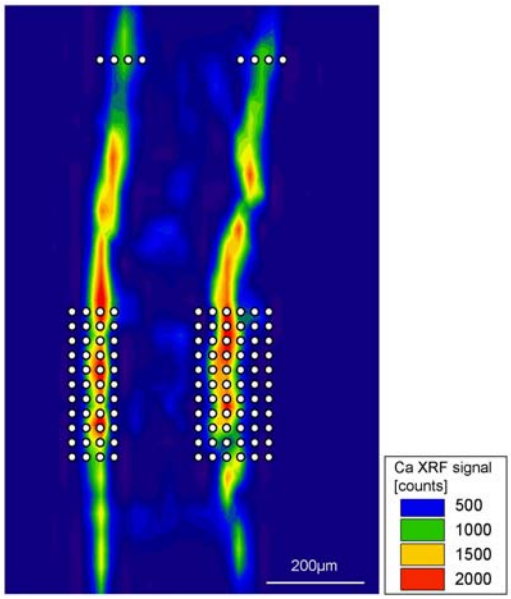

Figure 3-8: Calcium distribution map based on the calcium XRF signal of a fetal bone sample, F16.5. The selected measuring positions are highlighted by white dots, the legend of the calcium values is shown on the right. Both cortices of the long bone are clearly visible.

WAXD

The WAXD patterns of bone include the (002)-peak resulting from the diffraction of HA. Analysis of this peak after the radial integration of the 2D WAXD patterns revealed information on the amount of HA in the irradiated sample volume as the intensity of that peak was proportional to the HA amount. The area under the (002)-peak of each sample was thus used as a measure of the HA content in the irradiated sample volume. Besides this, the width of the (002)-peak revealed information on the mean mineral particle length, named L-parameter. The L-parameter was calculated as described in chapter 2.5.4 Determination of parameters – T-, Rho- and L-parameter using AutoFit.

Texture correction

The HA content and the amount of mineral particles in the samples were investigated by determining the integral intensity of the HA (002)-peak in the WAXD regime and the integral intensity in the SAXS regime, respectively. Accurate determination of this quantitative information implies three-dimensional integration of the data, but the measurement of thin sample slices as performed in this study delivers two-dimensional information. Therefore, the texture of the bone sample at the level of mineral particle orientation influences the results of the measurements leading to misinterpretation depending on the orientation of the bone sample in the experimental setup. Thus, an approach of cylindrical symmetry was used, which enables the three-dimensional integration of the data to exclude the influence of texture.

If the orientation distribution of crystalline grains in a polycrystalline sample shows a preferred direction, the measured diffraction peak intensities depend on this distribution. In our case, the HA crystals were not all aligned with the long axis of the bone. Therefore, a texture correction in order to correct the influence of orientation effects needs to be done. Assuming that the axis of cylindrical symmetry (i.e. the axis of long bone) is oriented into the direction χ_0, the angle of any (002) c-axis of HA with the symmetry direction was defined as Ψ. The sample coordinate system was denoted by (X, Y, Z) = R(sinΨcosΦ, sinΨsinΦ, cosΨ) with the angles Ψ and Φ in spherical coordinates defined in the usual way (see **Figure 3-9**). The Z axis is a unique axis of the cylindrical symmetry. The diffraction coordinate system was denoted by (x, y, z) = R(sinφ cos(χ-χ_0), sinφ sin(χ-χ_0), cos(χ-χ_0)) with the primary X-ray beam pointing into z direction and the area detector in the x–y plane. The Z axis (long bone axis) is tilted by an angle μ with respect to the z axis (primary beam axis). This coordinate rotation could be chosen without restriction of generality around the (common) y axis, i.e. the transformation equation is (x, y, z) = (Xcosμ + Zsinμ, Y, Xsinμ + Zcosμ). According to diffraction theory and the coordinate transformation [Paris and Muller, 2003] the equation cos(χ-χ_0) = (cosΨ + sinθ cosμ)/(cosθ sinμ) could be used. In the experiments the sample was perpendicular to the X-ray beam, set $\mu = 90°$, that's why cosΨ = cosθ cos(χ-χ_0) or

$$\Psi = \arccos(\cos\theta(\chi - \chi_0)).$$

The angle χ_0 could be determined from the XRF image of the longitudinal bone section. The angle θ is half the scattering angle (see **Figure 3-9**).

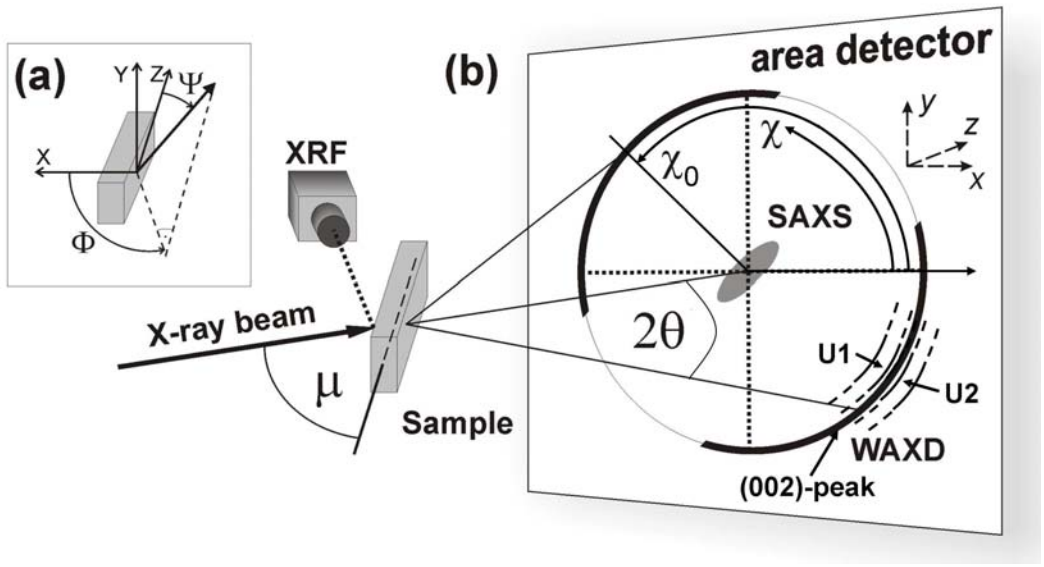

Figure 3-9: Sample coordinate system (a) and diffraction coordinate system (b). Simultaneous measurements of SAXS, WAXD and the XRF of calcium.

Texture correction of the HA (002)-peak

The HA (002) WAXD peak was azimuthally integrated. To correct the intensity of the (002)-peak in the WAXD pattern for background scattering, two regions (first background U1 and second background U2) beside the (002) diffraction ((002)-peak) have been integrated (see **Figure 3-9**). The inner and outer radius for U1 and U2 were defined in units of pixels, thereby the difference in the number of pixels between inner and outer radius for both backgrounds has been the same. The inner radius of the integration of the (002)-peak was equal to the outer radius of the first background U1 and the outer radius of the (002)-peak was equal to the inner radius of the second background U2 (see **Figure 3-9**). After azimuthal integration of the (002)-peak, U1 and U2, the medial background of U1(χ) and U2(χ) was subtracted from the (002)-peak(χ) to calculate the background corrected intensity I(χ):

$$I(\chi) = Peak(\chi) - ((U1(\chi) + U2(\chi))/2).$$

The integral intensity of I(χ) represented the HA content (named HA-002-peak area).

In order to correct the orientation influence, the following relation was used to receive the texture corrected integral intensity:

$$\int_{\theta}^{\pi/2} I(\Psi)\sin\Psi d\Psi = \cos\theta \int_{0}^{\pi/2} I(\chi' + \chi_0)\sin\chi' d\chi',$$

where $\chi' = \chi - \chi_0$. Note that the integration in the left-hand term starts at θ and not 0.
The integral intensity of I·sinΨ(Ψ) represented the HA content after texture correction.

Texture correction of the two-dimensional SAXS pattern

The intensity distribution I(χ) of the SAXS region was determined. The integral intensity of I(χ) represented the amount of mineral particles (named SAXS integral intensity). From the data frame D (scattering pattern), the beam center was determined. A frame S of the same size as the data frame D (3072·3072) was created, inserting the value of $\sin(\chi-\chi_0)$ into the pixel position, where each pixel was identified by its polar coordinate (q, χ). Finally, the product frame (pixel per pixel product) S·D = D´ was calculated using Fit2d. The data frame D´ was azimuthally integrated and the integral intensity of I´(χ) represented the amount of mineral particles after texture correction.

3.2.5 Statistical analysis

For statistical information mean values of different age groups of animals were compared by a one way analysis of variance (ANOVA) test, followed by Holm-Sidak [Walker, 2002]. Differences were considered significant when $P < 0.05$.

4 Results and Discussion

In this chapter information on developing bone in mice as well as on developing bone during healing in pig are presented. Different length scales, investigated by different methods, are described: namely (i) the tissue development and mineral distribution in the bone samples on the 100 μm-level, analyzed by histological staining and ESEM, (ii) the mineral particle orientation in the bone on the μm-level, studied by scanning SAXS and (iii) the mineral particle size on the nm-level, investigated by scanning SAXS and WAXD.

4.1 Natural bone development

The natural bone development was investigated using long bones, tibiae and femora, of wild type mice of strain C57BL/6, a commonly used strain in bone research. Experiments have been carried out using longitudinal sections of PMMA embedded murine long bones at different developmental stages during bone formation, at fetal stages F14.5, F16.5 and F18.5 and postnatal stages P1, P7 and P21. For synchrotron measurements F16.5, P1, P14 and P42 have been investigated.

4.1.1 Mineral distribution – 100 μm-level

Investigations on the 100 μm-level of growing long bones were feasible using conventional histological staining in combination with light microscopy and ESEM on bone samples at different stages during bone development.

Figure 4-1 shows combined Toluidine and Von Kossa staining of longitudinal bone sections of tibiae of different age from fetal stage day 16.5 (F16.5) to postnatal stage day 21 (P21). The bone sections are oriented such that the proximal end of the bone, the proximal epiphysis, is up and the distal end, the distal epiphysis, is down in the represented micrographs. The middle part of the bone is called diaphysis.

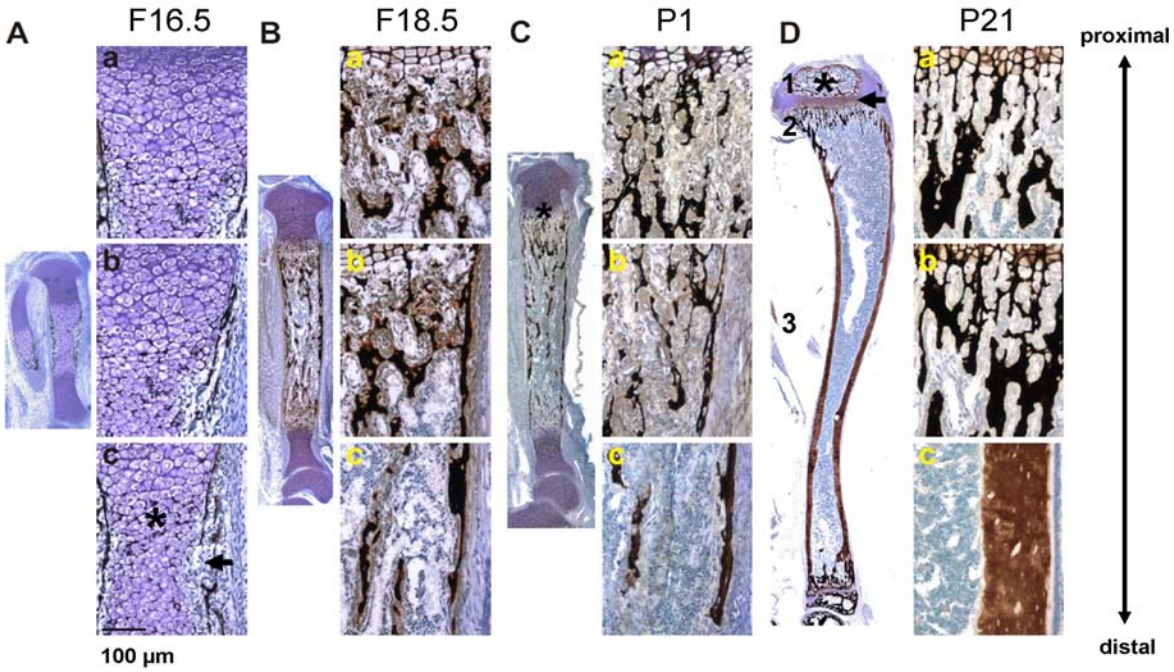

Figure 4-1: Toluidine and Von Kossa staining of longitudinal bone sections of different ages. Overviews of the samples, 4 x magnifications, and detailed images, 20x magnifications, show the transition between growth plate and primary spongiosa (a), cortical bone on the level of primary spongiosa (b) and diaphyseal bone cortex (c). (A) F16.5. The cartilaginous anlage (purple) is composed of hypertrophic chondrocytes in the diaphysis and proliferating chondrocytes at the distal and proximal epiphyses. Additionally, adjacent to the hypertrophic region a mineralized periosteal bone collar (black) and mineralized spots (black) in the cartilaginous matrix are formed, developing the primary ossification center (black asterisk). Vascularization is initiated (black arrow). (B) F18.5. Longitudinal growth occurs. Abundant mineralized trabeculae as well as cortical bone emerge. (C) P1. Ongoing length growth and the former bone collar is almost completely transformed into an integrated cortex. Persisting epiphyseal cartilage is forming the growth plate (black asterisk). (D) P21. The secondary ossification center is observable (black asterisk) and massive longitudinal growth is initiated after birth ending up in a complete long bone characterized by epiphysis (1) and metaphysis (2) at both ends of the bone and the interconnecting diaphysis (3).

At fetal stage F16.5, the earliest developmental stage investigated during bone growth, a cartilaginous model of the later bone, called cartilaginous anlage, is formed by chondrocytes, stained in purple by Toluidin (**Figure 4-1**, A). The chondrocytes appear hypertrophic in the central region of the cartilaginous model, where the primary ossification center is developing (**Figure 4-1**, A, c, black asterisk). Moreover, the cartilaginous matrix shows initial mineralization spots between the chondrocytes and at the periosteal bone collar, visualized in black by Von Kossa staining in **Figure 4-1** (A, a-c). Additionally, at F16.5 vascularization of the developing primary ossification center is initiated, shown in **Figure 4-1**, A, b and c, where a black arrow depicts developing blood vessels and bone matrix. Subsequently at F18.5, after initiation of trabecular bone formation within the primary ossification center and further bone collar development, longitudinal growth occurs (**Figure 4-1**, B). During this process the cartilaginous matrix of the growth plate is gradually added to the developing periosteal bone. Shortly after birth

long bones are characterized by persisting epiphyseal cartilage forming the later growth plate between the developing epiphyses and the diaphysis (**Figure 4-1**, C, black asterisk), increased amounts of mineralized bone matrix with osteoblasts, blood vessels and bone marrow. Bone matrix or blood vessels reveal unstained in the histological images, whereas bone cells are depicted in blue. Within the first weeks after birth massive longitudinal growth is initiated, resulting in continuous cortical bone and increasing numbers of trabeculae within the primary and secondary spongiosa (**Figure 4-1**, D, a-c). Moreover, the secondary ossification center of the proximal epiphysis becomes established, visible in **Figure 4-1**, D marked by a black asterisk in the proximal part of the long bone. Close to the secondary ossification center the proximal growth plate, consisting of cartilaginous matrix, is depicted in purple (see **Figure 4-1**, D, black arrow). At that stage of development, P21, the characteristics of long bones, namely the epiphysis and metaphysis at each end of the bone and the interconnecting diaphysis, are clearly distinguishable (see **Figure 4-1**, D, depicted by 1, 2, 3, respectively).

From these results it becomes obvious that during long bone development endochondral and intramembranous bone formation occur simultaneously, at the growth plate, during formation of the trabeculae, and at the diaphyseal cortex, during formation of the periosteal bone cortex, respectively. This is consistent with results found in literature describing bone development [Karsenty, 2003; Forriol and Shapiro, 2005; Shapiro, 2008].

Besides the tissue development, the mineral deposition and distribution in growing bones of mice at the same developmental stages as examined with histology have been qualitatively investigated using ESEM images made in BSE mode. In these images mineralized tissue is shown in different gray values, in which bright gray levels are corresponding to high mineral content and dark gray levels to low mineral concentration. Overview images including tibia and femur were taken of all developmental stages to visualize the mineralized areas in the samples. One representative sample per age during bone growth is shown in **Figure 4-2**, a. Furthermore, images of higher magnification were taken in the cortical region of longitudinal bone sections at different developmental stages during bone formation, shown in **Figure 4-2**, b, since the investigations on bone development are focused on the cortical bone development of the long bones.

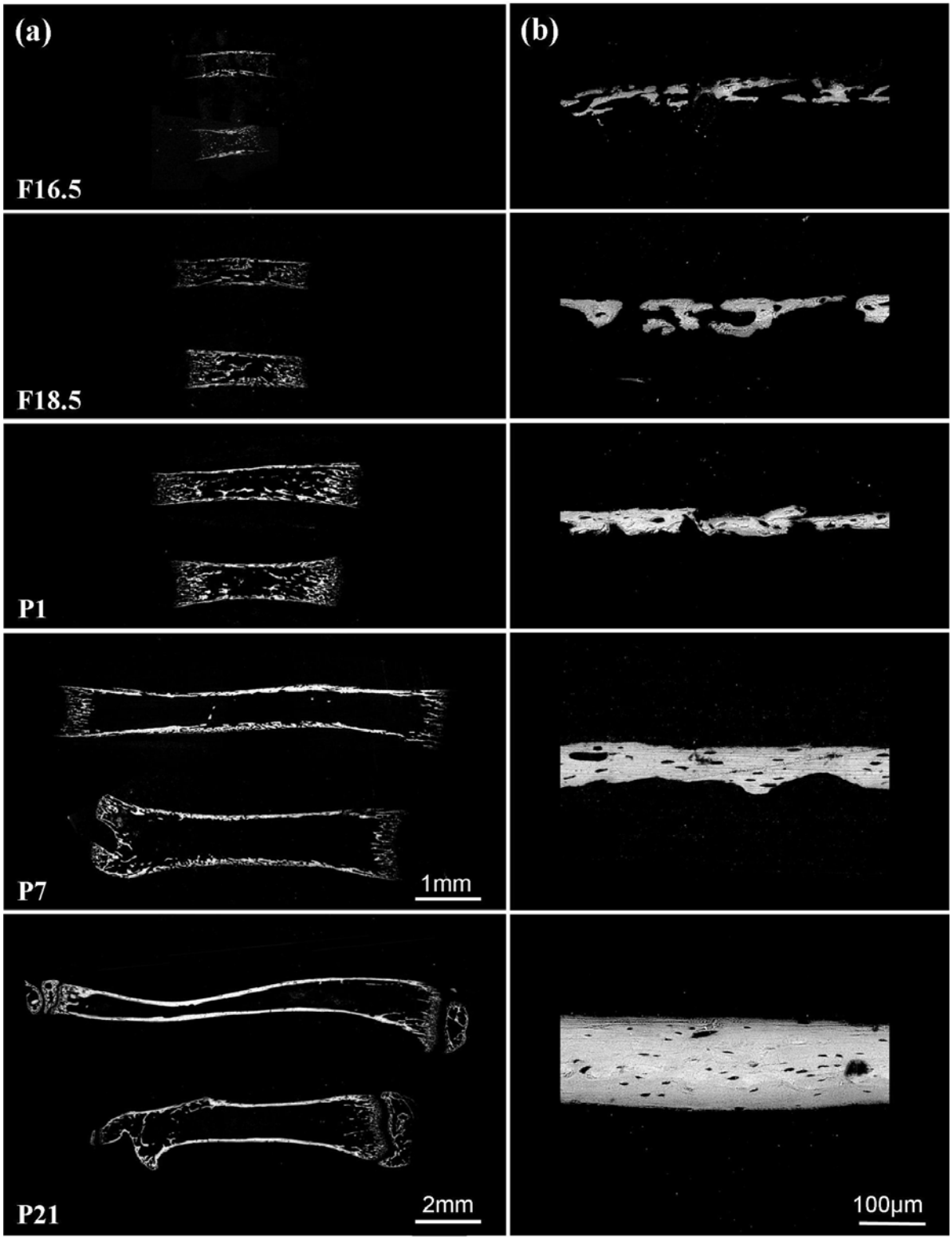

Figure 4-2: ESEM images in BSE mode visualizing the mineralized areas in gray, (a) overview images, 35x magnification, showing tibia (up) and femur (down) of different developmental stages, (b) cortical region, 260x magnifications, of longitudinal bone sections of different ages. Lighter gray regions display areas of higher electron density, meaning higher mineral concentration (calcium). Note the spotty mineralization at the fetal stages of bone development with a highly porous bone structure remaining until one day after birth, changing to a compact bone structure first at 7 days after birth.

By using this imaging technique it was possible to examine that there is no mineral formation at the fetal stage F14.5. The mineralization process of long bones in mice starts after F15.5 since the first mineral can be detected at F16.5, revealing spotty mineralization at that early stage of bone development (see **Figure 4-2**, F16.5, a). Mineral formation occurs at several spots in the bone matrix and in the periosteal region resulting in a highly porous bone structure (see **Figure 4-2**, F16.5, b), forming the periosteal bone collar. Shortly before birth, at F18.5, the amount of mineral and the size of the mineralized spots slightly increase (see **Figure 4-2**, F18.5, a). The bone still reveals no compact cortex structure, contrary there are only separate mineralized areas in the periosteal region (see **Figure 4-2**, F18.5, b). Interestingly, the bone one day after birth is still highly porous (see **Figure 4-2**, P1, a). Whereas the mineralized areas increase in size, large unmineralized regions remain resulting in a perforated bone structure (see **Figure 4-2**, P1, b). A compact bone cortex is first visible 7 days after birth, revealing continuous mineralization (see **Figure 4-2**, P7, a). The thickness of the cortex is increased at 7 days after birth compared to P1 and there are holes in the bone tissue visible which could correspond to osteocyte lacunae or developing blood vessels (see **Figure 4-2**, P7, b, red asterisk). At P21 the compact bone is fully developed showing a dense bone structure (see **Figure 4-2**, P21, a) with small holes, possibly osteocyte lacunae, aligned parallel to the longitudinal axis of the bone (see **Figure 4-2**, P21, b, yellow asterisk) and possibly blood vessels, shown by the big holes (see **Figure 4-2**, P21, b, green asterisk). The presented ESEM images support the results of the histological investigations. The bone development starting from mineralized spots in the bone matrix and the periosteal bone collar at the fetal stages of bone formation, continuing with length growth and increasing mineralization at the early postnatal stages and ending with a completed bone revealing a compact bone cortex at P21 can be clearly observed.

Concerning locomotion of mice it is known that new born mice one day after birth show no motion (animal facility at the MPIMG). According to the ESEM images of bones at that stage of development one can assume that it is maybe not feasible for mice to weight the bones strongly as in case of walking due to the porous bone structure and thus mice are not able to move one day after birth. Around 7 days after birth young mice start to move and locomotion is increasing with age after that stage of bone development. This behavior could be explainable by the results on bone structure from the ESEM images, discovered in this study. Whereas the bones of one day old mice are still highly porous and thin, thus possibly too instable to bear the weight of the mouse, the cortex of the bones of 7 days old mice is thicker and shows a compact bone structure thus enabling movement.

Beside the investigations on the 100 µm-level, revealing information on the tissue development and the mineral distribution by using histological staining and the ESEM,

studies on the next lower level, the µm-level, revealing information on the mineral particle orientation examined by SAXS, are reported in the following.

4.1.2 Mineral particle orientation – µm-level

The mineral arrangement in bone was investigated using the SAXS signal, resulting from the diffuse scattering of the mineral particles in bone. ESEM images and radiographies were used to visualize the mineralized areas in the bone sample and to hence select regions of interest for subsequent investigations. The analysis of SAXS patterns provided information about the degree of mineral particle alignment in the illuminated sample volume at that position of the analyzed long bone of wild type mice. Radiographies of one representative bone sample of each developmental stage during bone formation and corresponding 2D SAXS patterns are shown in **Figure 4-3**.

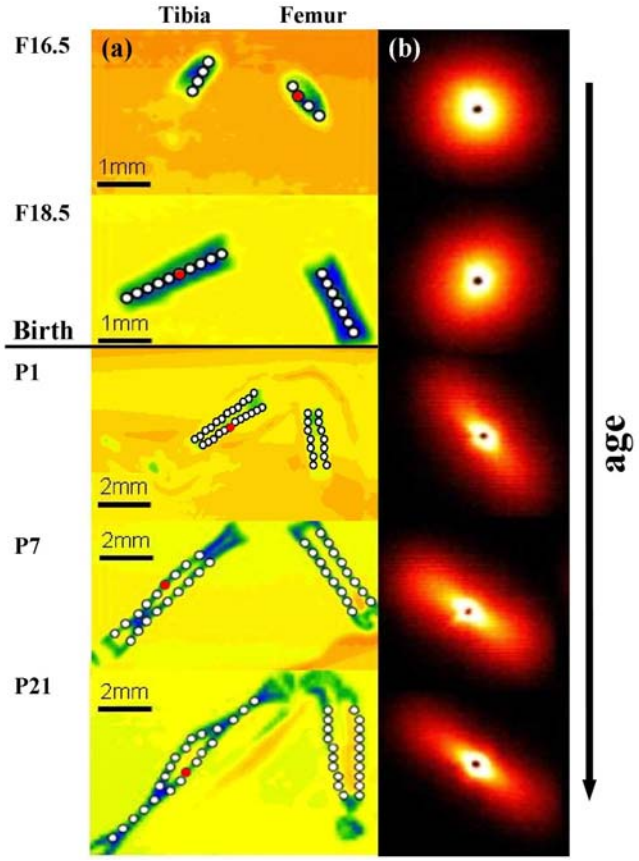

Figure 4-3: (a) Radiographies of tibia and femur of all developmental stages during bone formation vertically ordered by increasing age. Blue is showing areas of high X-ray absorption, representing the bone sample. SAXS data were obtained at positions along the diaphyseal cortex of tibiae and femora as depicted by white dots. (b) 2D SAXS patterns of one representative position in the bone samples, highlighted by the red dot in the radiographies. Circular SAXS patterns – random orientation of the mineral particles; elliptical SAXS patterns – aligned mineral particles, oriented perpendicular to the long axis of the ellipse. Note that the mineral particles in the fetal bone are randomly oriented whereas the mineral particles in the postnatal bone are aligned parallel to longitudinal axis of the bone.

Radiographies were produced by measuring the absorption of the incident X-ray beam by the sample, whereas in the SAXS experiment the scattering of the incident X-ray beam was measured. Since mineralized tissue shows higher absorption of the X-ray beam than the unmineralized tissue or the embedding material around, mineralized areas in the sample are clearly visible in the radiographies (see **Figure 4-3**, a, blue – high X-ray absorption). Thus, the radiography enables the selection of measuring positions in the mineralized tissue for the SAXS experiment (see **Figure 4-3**, a, white dots). The measurements of the SAXS signal using the laboratory equipment have been performed along the cortex of the entire diaphysis, from the proximal part of the diaphysis (close to the proximal growth plate) to the distal part of the diaphysis at different developmental stages (see **Figure 4-3**, a, white dots). From the 2D SAXS patterns (see **Figure 4-3**, b) qualitative information on the mineral arrangement in the irradiated sample volume of the bone sample can be estimated. A circular SAXS pattern indicates that the mineral particles in the illuminated sample volume are randomly oriented, as shown for the fetal bone, whereas an elliptical SAXS pattern indicates that the mineral particles are aligned in a preferred orientation, namely perpendicular to the long axis of the ellipse, as presented for the postnatal bone (see **Figure 4-3**, b). The SAXS patterns shown in **Figure 4-3**, b clearly demonstrate that the mineral particles in postnatal bone are oriented parallel to the longitudinal axis of the long bone, already on day after birth (P1). Moreover, the mineral orientation includes information about the mineral/collagen architecture in bone as the main axis of the mineral crystals is known to be oriented in the same direction as the collagen fibrils in bone [Tesch, Vandenbos et al., 2003; Fratzl and Weinkamer, 2007].

By analyzing the SAXS measurements along the cortex concerning mineral orientation it becomes obvious that the mineral alignment in long bones, tibia and femur, is dependent on the position in the cortex along the diaphysis (see **Figure 4-4**).

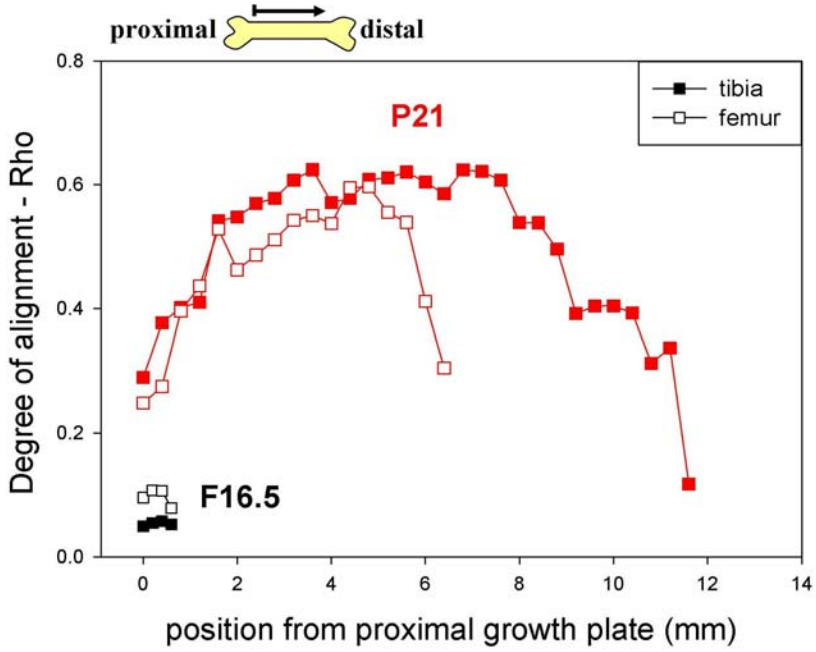

Figure 4-4: Degree of alignment of the mineral particles, Rho, as a function of the measuring position of the SAXS signal from the proximal diaphysis over the midshaft region to the distal diaphysis (left end to the right end of the curves). Data of the earliest stage of bone development, F16.5 (■ tibia, □ femur), and the latest postnatal stage P21 (■ tibia, □ femur) are shown. Note the position depending differences in the mineral arrangement, especially in the postnatal bone. Mineral particles in the midshaft region of the cortex of long bones are much higher aligned than the mineral particles in the proximal and distal diaphyseal regions.

Interestingly, even though the mineral particles in fetal bones, F16.5, show very low values of the degree of alignment, thus being randomly oriented, there is already a trend of little higher values of the mineral orientation in the center of the periosteal bone collar observable for both tibia and femur (see **Figure 4-4**). At F18.5, tibia and femur still reveal very low Rho values, about 0.1, but exhibiting little higher values in the midshaft region of the diaphysis, about 0.2, as well (data not shown). Strong differences in the mineral arrangement depending on the measuring position in the cortex become obvious in the postnatal stages of bone development, P1, P7 and P21, in both tibiae and femora (see **Figure 4-4**, only P21 shown). The mineral particles in the midshaft region of the postnatal long bones are much higher oriented than the mineral particles in the proximal and distal parts of the diaphysis, as represented for P21 in **Figure 4-4**. It can be illustrated that the mineral particle orientation increases from the proximal diaphyseal end to the midshaft region of the bones and decreases again from the midshaft region to the distal diaphyseal end of the long bones. For P1 an increase of the degree of mineral alignment from the parts close to the joints to the midshaft of the bone by about 100% can be observed, from Rho values of about 0.2 to about 0.4 (data not shown). P7 and P21 bones exhibit even higher rates of increase of Rho. For P7 an increase from about 0.3 in the proximal and distal parts of the diaphysis to about 0.5 in the midshaft region can be measured (data not shown). P21

bone reveals an increase of Rho from about 0.2 to about 0.6 in the midshaft (see **Figure 4-4**). Thus, the mineral particle arrangement in tibiae and femora of P21 mice increases by about 200%. Tibia and femur reveal the same trend of the position dependent mineral arrangement (see **Figure 4-4**). These results are in good agreement with the results of Tesch and his coworkers who investigated the position dependent mineral particle arrangement in postnatal murine tibiae and femora [Tesch, Vandenbos et al., 2003].

The position dependent differences in the mineral orientation may be due to differing stages of development within the bone. Whereas the bone in the midshaft region of the diaphysis is formed first starting from the periosteal bone collar, the bone away from the center of the diaphysis is formed later during length growth of the bone [Zoetis, Tassinari et al., 2003; Shapiro, 2008]. Thus, the mineral particles in the midshaft region are aligned to a greater extend compared to the proximal and distal parts of the diaphysis. Another reason may be ongoing remodeling processes in the bone, resulting in a higher ordered mineral/collagen matrix in the midshaft region, being remodeled earlier than the proximal and distal parts of the diaphysis.

Besides the analysis of the mineral arrangement dependent on the position in the cortex, the mineral arrangement dependent on age has been examined. Therefore, the SAXS measurements at positions in the midshaft region of the cortex of tibiae and femora in mice at the different developmental stages from fetal to postnatal bone have been analyzed. The degree of the mineral alignment dependent on the age of the bone samples is shown in **Figure 4-5**.

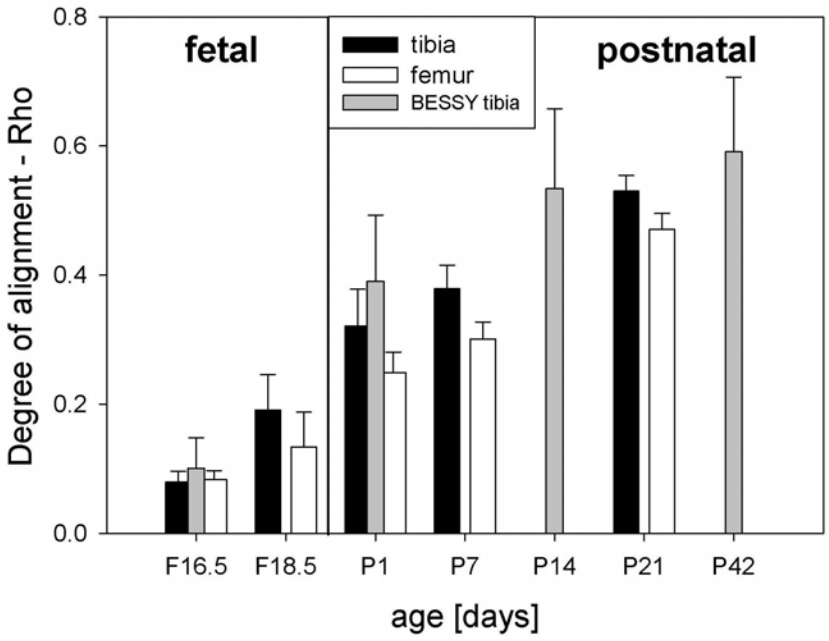

Figure 4-5: Degree of mineral crystal alignment (mean ± standard deviation), Rho-parameter, as a function of age. Laboratory SAXS data are shown for tibiae in black and femora in white. Additionally, BESSY II data of tibiae are shown in gray. The vertical black line is representing the time point of birth. Note the significant increase in mineral orientation after birth and with age as well as the significant difference in the degree of alignment between postnatal tibiae and femora (P1 and P7, $p<0.001$).

The analysis of the mineral orientation dependent on age clearly point out that the mineral particles at the fetal stages of bone development reveal a complete lack of orientation, meaning that these mineral particles are randomly oriented (see **Figure 4-5**). Rho-parameter values below 0.2 in the fetal bone display that less than 20% of the mineral particles are aligned in a preferred orientation. Even though there is an increase in mineral orientation from F16.5 to F18.5, the degree of mineral alignment remains still very low, with less than 20% of the mineral particles being aligned in a preferred orientation (see **Figure 4-5**). Interestingly, the degree of mineral particle arrangement in bone strongly changes within less than 2 days, from half a day before birth, F18.5, to one day after birth, P1 (see **Figure 4-5**). The degree of alignment of the mineral particles significantly increases after birth ($p<0.001$). Whereas before birth the mineral particles are randomly oriented, there are about 30% of the mineral particles aligned in a preferred orientation, revealed by Rho values of about 0.3 (see **Figure 4-5**). Furthermore, a significant increase of the mineral alignment with age becomes obvious ($p<0.001$). The arrangement of the mineral particles from P1 to P42 increases by a factor of 2, from Rho values of about 0.3 to 0.6 in 6 weeks. Thus, at P42 about 60% of the mineral particles are aligned in a preferred orientation, representing a value of mineral alignment in mature bone, where on average 50% to 60% of the mineral particles are aligned in a preferred orientation [Grabner, Landis et al., 2001]. Mineral particles in postnatal bone are predominantly aligned parallel to the longitudinal

axis of the bone, as represented by the SAXS patterns in **Figure 4-3**. The results from the laboratory are confirmed by the synchrotron measurements at BESSY II, where the earliest fetal stage, F16.5, the earliest postnatal stage P1, and two additional older developmental stages, P14 and P42, have been investigated (see **Figure 4-5**).

Interestingly, these data demonstrate that the mineral arrangement in the two types of long bones, analyzed in this study, is considerably different at the postnatal stages of bone development. The mineral particles in the tibiae are significantly higher oriented than the mineral particles in the femora within the first week of bone growth (P1 and P7, $p<0.001$). Whereas in femora of P7 mice about 30% of the mineral particles are aligned in preferred orientation, revealed by Rho values of about 0.3, there are already about 40% aligned in the tibia of P7 mice, represented by Rho values of about 0.4 (see **Figure 4-5**).

The significant increase of the mineral alignment from half a day before birth to only one day after birth leads to the assumption that the environmental changes occurring at birth may provide a mechanical stimulus, which subsequently influences the growth and arrangement of the collagen/mineral composite dramatically. A mechanical stimulus could initiate higher muscle contraction after birth than before and thus effect the mineral development and organization. Former studies have emphasized the regulating role of mechanical stimuli on skeletal development by demonstrating that the mineralization process only starts after the first muscle contraction, hence suggesting that the mineralization is stimulated by mechanical loads [Burger, Klein-Nulend et al., 1991; Tanck, Van Donkelaar et al., 2004]. Mechanical loading seems to be important not only for maintenance but also during development of the fetal skeleton [Ruff, Holt et al., 2006]. The remarkable difference in the mineral arrangement between tibia and femur could result from the different size of these bones and therefore different loads they are subjected to. Specifically, the tibia is smaller in diameter and longer than the femur and is hence assumed to receive higher loads which could lead to higher alignment of the collagen/mineral composite. Akhter et al. [Akhter, Fan et al., 2004] determined that the hardness of tibiae is higher than that of femora. The difference in hardness between the two long bones is possibly due to the difference in mineral alignment. A higher orientation of the mineral particles in the tibia could be the reason for the increase in hardness as the mechanical properties of bone are influenced by the structure at all hierarchical levels [Fratzl, Gupta et al., 2004].

Additionally to the analysis of the µm-level, revealing information on the mineral particle orientation examined by SAXS, the investigations on the nm-level, revealing information on the mineral particle size in the bone studied by SAXS and WAXD, are described in the following.

4.1.3 Mineral particle size – nm-level

Besides the mineral arrangement in bone, the mineral particle thickness has been investigated using SAXS, revealing information on the nanometer level of the hierarchical structure of bone. Mineral particles in bone are supposed to be platelet shaped. The T-parameter describes the mean thickness of the mineral platelets in the irradiated sample volume. Laboratory SAXS measurements along the entire diaphyseal cortex of the long bones, tibiae and femora, of mice of different age (radiographies and measuring positions shown in **Figure 4-3**) have been analyzed for the mean mineral particles thickness. The mineral thickness dependent on the position in the cortex is shown in **Figure 4-6** for the same developmental stages (F16.5, P21) of bone development as for the mineral arrangement (see **Figure 4-4**).

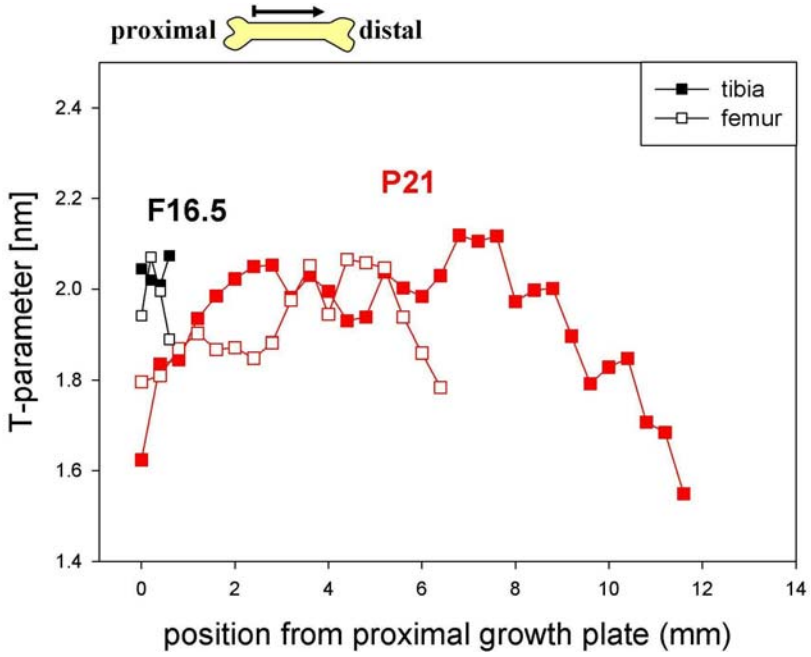

Figure 4-6: Mineral particle thickness as a function of the measuring position on the cortex. Data for fetal stage F16.5 (■ tibia, □ femur) and postnatal stage P21 (■ tibia, □ femur) are shown from the proximal diaphysis (left end of the curve) over the midshaft region to the distal diaphysis (right end of the curves). Note the increase of the mineral particle thickness in the midshaft region of the cortex.

Interestingly, the mineral particle thickness at the earliest investigated stage of bone development is about 2 to 2.1 nm, being similar to the T-parameter values of older bone (see **Figure 4-6**). The data on the mineral particle thickness at the earliest stage of bone development, F16.5, indicate that the mineral particles exhibit high thicknesses but rather independent on their position in the cortex of the diaphysis. From F18.5 on it is observable that the mineral particle thickness increases in the midshaft region compared to the distal and proximal ends of the diaphysis (data not shown). As already shown for the mineral

orientation, there is also a position dependency of the mean mineral thickness clearly illustrated for postnatal tibiae and femora (see **Figure 4-6**, only P21 shown). Even though there is a higher variability of the mineral thickness along the cortex present this trend of the mineral thickness is clearly visible. The mineral particles in the distal and proximal region of the diaphysis are thinner than the mineral particles in the midshaft region of the cortex. It can be illustrated that the mineral particle thickness increases from the proximal part of the diaphysis to the midshaft region and decreases from the midshaft region of the diaphysis to the distal part in both tibiae and femora. Tibiae of P21 mice show an increase in the mineral particle thickness from about 1.6 nm to 2.1 nm in the midshaft and femora from about 1.8 nm to about 2.1 nm (see **Figure 4-6**).

As already discussed for the differences in the mineral alignment, the differences in the mineral particle thickness, depending on the position in the postnatal bone, could be explained due to the assumption that the midshaft region is formed first and remodeled first, resulting in thicker mineral particles in that region corresponding to "older" bone [Zoetis, Tassinari et al., 2003; Shapiro, 2008].

Additionally to the position dependent changes of the mineral particle thickness the dependency on age during bone development has been investigated. Equally to the examination of the mineral orientation, the SAXS measurements performed in the midshaft region of longitudinal bone sections at different developmental stages have been analyzed regarding the mean mineral thickness. These results are shown in **Figure 4-7**.

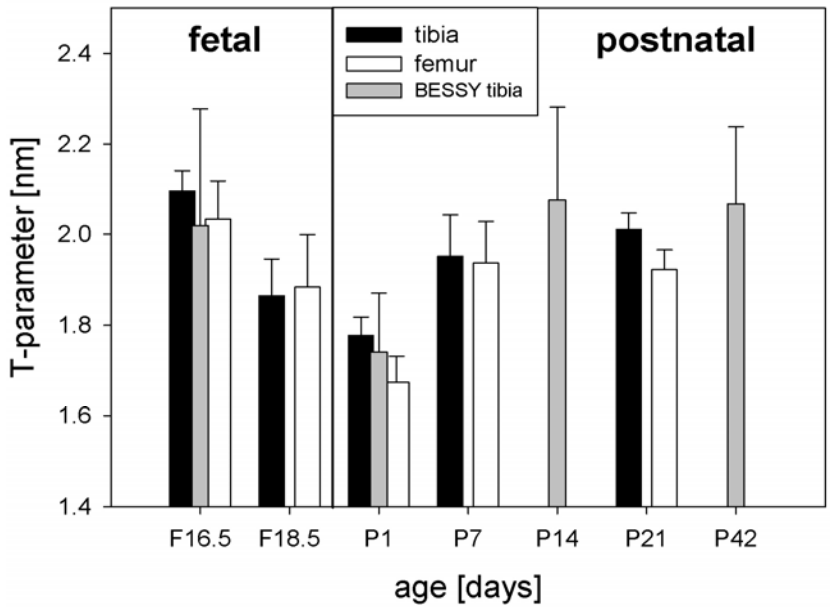

Figure 4-7: Mineral particle thickness (mean value ± standard deviation), T-parameter, grouped by age. Laboratory SAXS data are shown for tibiae in black and femora in white. Additionally, BESSY II data of tibiae are shown in gray. The vertical black line is representing the time point of birth. Note the decrease in particle thickness between the fetal stages of bone development and the significant increase with age ($p<0.001$).

Surprisingly, the thickness of the mineral particles in tibiae and femora strongly decreases during the fetal stages of bone development (F16.5 and F18.5). The mean mineral particle thickness decreases remarkably before birth, from about 2 to 2.1 nm at F16.5 to about 1.85 at F18.5 (see **Figure 4-7**). Furthermore, a considerable decrease of the mineral particle thickness from half a day before birth, F18.5, to one day after birth can be observed, from about 1.85 nm to about 1.7 nm (see **Figure 4-7**). Besides the thinning of the mineral particles in the early bone development, **Figure 4-7** clearly shows that the mineral thickness increases significantly with age ($p<0.001$), but only after birth during postnatal bone development. Mineral particles in bone one day after birth, P1, are about 1.7 nm in thickness whereas mineral particles of 3 weeks (P21) or 6 weeks (P42) old bones are about 2 nm in thickness. These results are confirmed by the synchrotron measurements at BESSY II on four developmental stages, F16.5, P1, P14 and P42 (see **Figure 4-7**). Moreover, the comparison of both types of long bones, tibia and femur, reveals no significant difference in the mineral thickness between these two bones in contrast to the mineral arrangement.

The decrease of the mineral thickness before birth from T-parameter values about 2 to 2.1 nm to values about 1.85 nm could indicate that at the earliest stage of bone development, F16.5, a precursor mineral phase is deposited and subsequently transformed into mature HA crystals with a lower thickness. Since the SAXS signal is not dependent on the crystallinity of the analyzed bone sample it is not possible to make any assumption concerning the degree of the crystallinity of the early mineral using SAXS.

In addition to the SAXS signal of the bone samples, measured with the laboratory equipment and at the synchrotron beam line μ-Spot at BESSY II, the WAXD signal of bone was measured at the synchrotron beam line along with the SAXS signal. Furthermore, the XRF signal of calcium was measured at BESSY II enabling the detection of very low amounts of mineral such as in the fetal bone samples. Calcium distribution maps of regions of interest in the sample, defined by the ESEM images, were created based on the XRF signal of calcium. These calcium maps were used to select measuring positions for SAXS/WAXD/XRF measurements. **Figure 4-8** shows the calcium distribution maps of the samples investigated at BESSY II with selected measuring positions.

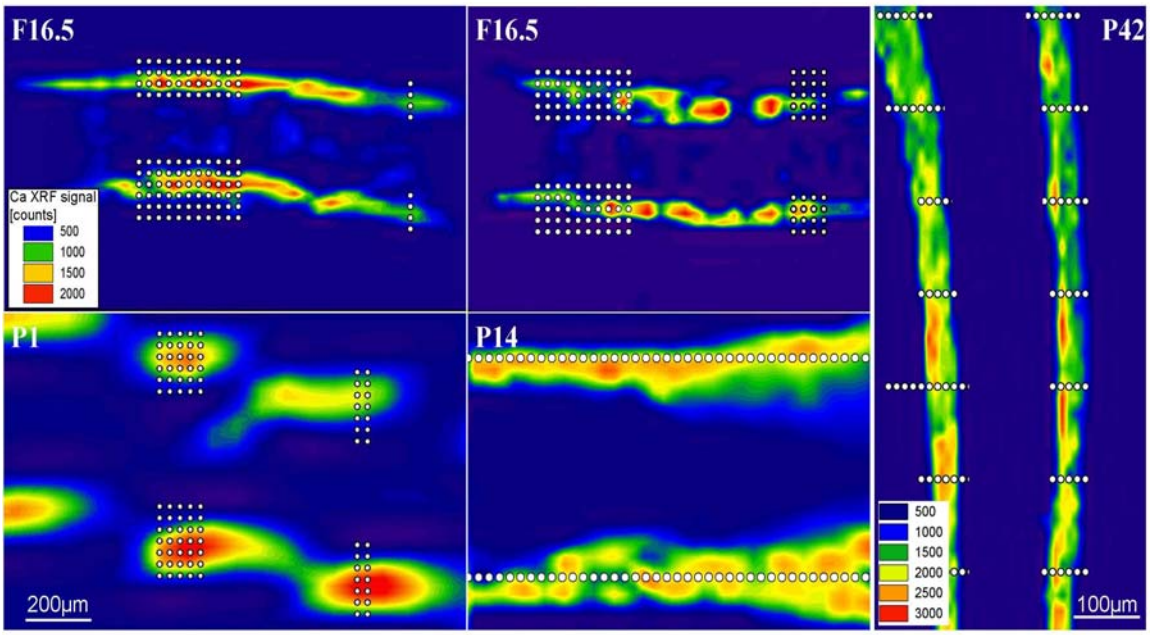

Figure 4-8: Calcium distribution maps based on the XRF signal of calcium for different developmental stages of tibiae investigated at the synchrotron beam line BESSY II. Positions for SAXS/WAXD/XRF measurements are indicated by white dots. The scale for the calcium counts of the XRF signal of F16.5 and P1 are shown in the upper left and the scale for P14 and P42 are shown in the lower right.

The calcium distribution maps clearly show the mineral in the sample, due to higher calcium content, and it was thus possible to visualize the mineralized areas in the bone sample (see **Figure 4-8**). Especially for the fetal stages of bone development it was not possible to detect the mineral by only producing a radiography. Both cortices of the tibiae could be seen separately even at the earliest fetal stage of bone development, F16.5 (see **Figure 4-8**). Measuring positions for the SAXS/WAXD/XRF measurements could be defined either across both cortices (see **Figure 4-8**, white dots, F16.5, P1, P42) or along the cortex (see **Figure 4-8**, white dots, P14). The calcium distribution maps of the fetal stages of bone development show small amounts of mineral with spots being already higher mineralized at the periosteal bone collar. At P1 the calcium distribution map shows an inhomogeneous mineralization (calcium distribution) as well. First the calcium distribution map of the tibia at P14 reveals continuous mineralization, just as for P42. These calcium distribution maps of different developmental stages during bone formation confirm the results of the histological investigations and the ESEM imaging concerning the spotty and inhomogeneous mineralization at F16.5 and P1, respectively, and the continuous mineralization at P14 and P42.

In the following, the results observed from the WAXD signal of the measurements are described. By analyzing the width of the (002)-peak the average length, the L-parameter, of the mineral particles in the irradiated sample volume of bone samples of differing age could be determined. The correlation of the mean mineral thickness, T-parameter, and the

mean mineral length, L-parameter, of tibiae at different developmental stages during bone development is shown in **Figure 4-9**.

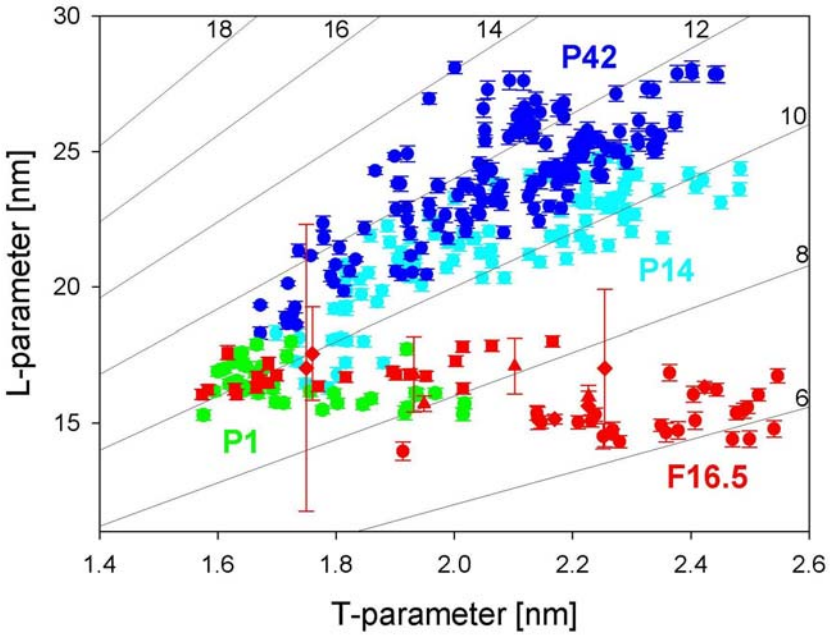

Figure 4-9: Length of the mineral particles (mean ± standard deviation), L-parameter, against the mean mineral crystal thickness, T-parameter. Different colors indicate different developmental stages of the bone, hairlines represent different aspect ratios, L/T. Note that fetal mineral particles are short and thick whereas mineral particles after birth are thinner initially but getting longer and thicker with age with a correlation between length and thickness. Furthermore, fetal and older bone tissue exhibit totally different aspect ratios L/T.

The mineral particles at the fetal stage of bone development show a high variation of the T-parameter values, reaching very high thicknesses up to 2.5 nm, but display low L-parameter values, always about 17 nm (see **Figure 4-9**, red symbols, different symbols represent different samples). Thus, the fetal mineral particles are bulky particles, thick and short. After birth the mean mineral particle thickness increases, as already represented in **Figure 4-7**, from F18.5 to P1, revealing T-parameter values ranging from 1.6 nm to 2 nm, but the L-parameter is still low, displaying values below 20 nm (see **Figure 4-9**, green symbols). With increasing age of the bones during bone development, both thickness and length of the mineral particles are increasing. Several mineral particles in mature bone are reaching T-parameter values up to 2.4 nm and L-parameter values close to 30 nm. Thereby a correlation between the T- and the L-parameter becomes obvious, namely the thicker the mineral particles the longer they are (see **Figure 4-9**, cyan and blue symbols). These results demonstrate that in postnatal bone the length of the mineral particles increases with age after birth at the same time as the thickness, while in the fetal bone mineral particles are thick but much shorter.

From **Figure 4-9** it becomes obvious that mineral particles in fetal bone are totally different from older bone mineral particles concerning their size. While the T-parameter in fetal bone varies in a broad range, reaching very high values, the L-parameter is low, always about 17 nm, but increases with age. The mineral particles in bone are embedded in a collagen matrix built up of staggered collagen fibrils including gap- and overlap-zones (see chapter 2.1.1 Bone composition and structure). Former studies revealed that gap-zones in wet mineralized collagen are about 20 nm in size and supposed to be the nucleation sites for the mineralization [Bonar, Lees et al., 1985; Landis, 1995]. Thus, the size of the fetal mineral particles of about 17 nm in length, determined in this study, fits perfectly with the size of the gap-zones in wet mineralized collagen and is therefore supporting the idea of the nucleation of mineralization in the gap-zones of the collagen network. The length growth of the mineral particles during bone development up to almost 30 nm leads to the assumption that the mineral particles in the gap-zones extend into the overlap-zones in the collagen network with increasing mineralization. Another interesting size development during mineral growth is the much stronger increase of the mineral length compared to the mineral thickness. Hence, the aspect ratio length to thickness of the mineral particles, L/T, changes dramatically from fetal to mature bone (see **Figure 4-9**, hairlines represent different aspect ratios L/T). Fetal mineral particles exhibit an aspect ratio L/T about 6, whereas the older bone mineral particles display much higher aspect ratios of about 12. The aspect ratio L/T of the mineral particles is correlated with the mechanical properties of the bony tissue [Gupta, Schratter et al., 2005]. Values for the aspect ratio of low mineralized cartilage are about 5 and of higher mineralized bone tissue about 10 to 15 [Gupta, Schratter et al., 2005]. Comparing literature values of different bony tissues, like bovine tibia, fallow deer tibia, reindeer antler, human femur, polar bear femur and fin whale bulla [Currey, 2002] in the way Gupta et al. did it for their data reveals aspect ratios L/T for bony tissues in the range between 10 to 15 as well. Thus, the values of the aspect ratios determined in this study for low mineralized, fetal bone and highly mineralized, postnatal bone are perfectly fitting in that range. Furthermore, the data of Gupta et al. demonstrate that the mechanical properties of the bone tissue increase by increasing the aspect ratio L/T during maturation of the bone [Gupta, Schratter et al., 2005]. It is thus reasonable that the mineral particles exceed the size of the gap-zones during bone development from fetal to mature bone to achieve increased mechanical properties.

Beside the analysis of the mineral particle properties, such as mineral orientation and size during bone development, the composition of the mineral phase at the fetal stage F16.5 and the postnatal stage P1 of bone development has been investigated to further characterize and compare the fetal and the postnatal mineral particles.

4.1.4 Mineral particle composition

Besides the information on the arrangement and size of the mineral particles in bone from the SAXS and WAXD data, information on the mineral particle content, the amount of HA and the calcium content can be received from the SAXS, WAXD and XRF data. The integral intensity of the SAXS data is a measure of the amount of mineral particles in the illuminated bone sample volume, the area under the HA-002-peak is proportional to the HA content in the bone sample and the calcium XRF signal represents the amount of calcium in the irradiated sample volume. The possibility to directly correlate the SAXS, WAXD and XRF data at distinct positions of the bone sample is a fundamental new approach in data analysis (**Figure 4-10**).

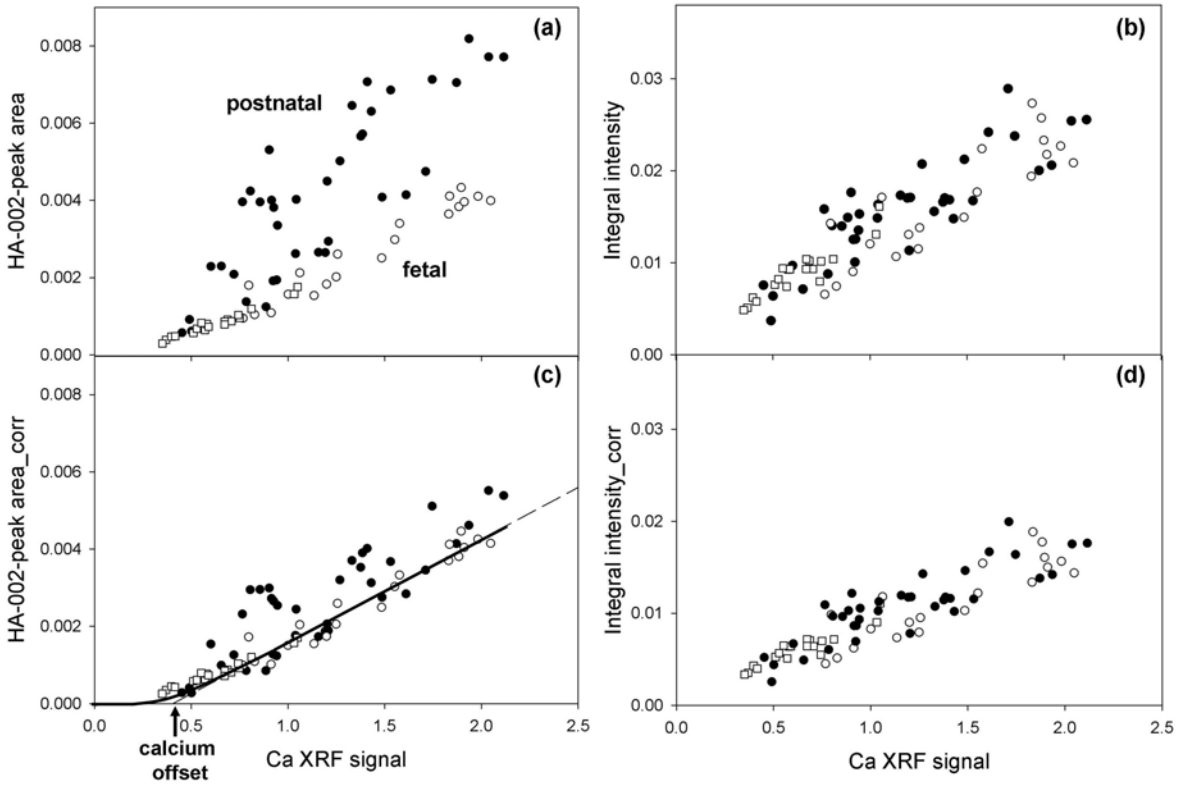

Figure 4-10: Comparison of the SAXS, WAXD and XRF data for two representative fetal samples and one representative postnatal bone sample. (a) HA-002-peak area as a function of the calcium XRF signal. Fetal data are shown with open symbols (□, ○), postnatal data in black (●). Note the lower intensities of the (002)-peak in fetal bone, indicating less HA. (b) SAXS integral intensity as a function of the calcium XRF signal. Note that the data for fetal and postnatal samples are well overlaying. (c) HA-002-peak area corrected for texture effects as a function of the calcium signal. Note that there is no difference between fetal and postnatal bone and that the correlation between HA and calcium is not linear (black line – guide to the eye) and a linear fit of the fetal data (dashes line) reveals a calcium offset. (d) SAXS integral intensity corrected for texture effects as a function of the calcium signal, still revealing no difference between fetal and postnatal bone.

In a first step, the HA-002-peak area of the fetal bones was compared with the postnatal bone in a plot against the calcium XRF signal, shown for two representative fetal bone samples (F16.5) and one postnatal bone sample (P1) in **Figure 4-10**, a. It becomes obvious that the HA-002-peak area is much higher in the postnatal bone than in the fetal bone, representing a higher HA content in the postnatal bone. Furthermore, it can be observed that both fetal bone samples match, even though exhibiting highly different amounts of HA and calcium. The comparison of the SAXS integral intensity of fetal and postnatal bone again plotted against the calcium XRF signal reveals no difference between postnatal and fetal bone, indicating no difference in the mineral particle content in both bone samples (see **Figure 4-10**, b). That overlay lead to the assumption that in the same range of calcium content there is the same amount of mineral particles present in both fetal and postnatal bone. In a second step the influence of the orientation of the mineral particles in bone is excluded. The mineral particle orientation in fetal and postnatal bone is different; having highly oriented mineral particles in the postnatal bone but randomly oriented mineral particles in the fetal bone. The difference in texture can influence the results and thus lead to misinterpretation of the quantitative data. After the correction of the HA-002-peak area for texture effects there is no remaining difference between the HA-002-peak area in fetal and postnatal bone (see **Figure 4-10**, c). Interestingly, the correlation between HA amount and calcium content is not linear (see **Figure 4-10**, c, see guide to the eye), since the theoretical origin of the curve is at zero HA content and zero calcium content, but a linear fit of the fetal data points reveals an offset of calcium. This indicates that there is calcium present in the bone but no HA. This calcium offset is even observable in the postnatal bone, whereas the offset value of calcium in fetal bone is higher than in postnatal bone. The SAXS integral intensity against the calcium XRF signal still reveals no difference between fetal and postnatal bone after texture correction, representing the same amount of mineral particles in fetal and postnatal bone in the same range of calcium (see **Figure 4-10**, d).

These results clearly point out that the differences in the HA-002-peak area between fetal and postnatal bone without texture correction raised due to differences in the mineral arrangement of the bone tissue, namely the lack of orientation in the mineral particles in the fetal bone and not due to different amounts of HA. However, the calcium offset in the fetal bone determined after texture correction could indicate that there is calcium present which is not bound in HA, but maybe in a precursor mineral phase. But from these data it is not possible to conclude whether this precursor mineral phase is amorphous. The calcium offset is possibly a minimum calcium concentration necessary to form HA. A calcium offset even in the postnatal bone leads to the assumption that the precursor mineral phase and mature mineral particles seem to be coexistent in mature bone. This finding is

consistent with observations of small spherical particles besides the crystal platelets in mature bone of fish fins or baboon bone [Mahamid, Sharir et al., 2008; Wang and Nancollas, 2008]. The value of the calcium offset in fetal bone is higher than that in postnatal bone, indicating a higher amount of calcium not bound in HA but maybe in a precursor mineral phase in the fetal bone. Even though both fetal samples match, they reveal totally different amounts of HA, possibly indicating that the formation of HA proceeds very rapidly and can be thus highly different in different animals of the same age.

The following section represents the investigations on bone development in genetically modified mice exhibiting a severe bone phenotype. Since the strain of the transgenic mice is the same as for mice used for the investigations on normal bone development, these data can be compared.

4.2 Bone development in NF1 mice

To study the effect of the deficiency of neurofibromin 1, resulting in Neurofibromatosis type 1 (NF1), mice of 15 days, 42 days and 3 month postnatal of strain C57BL/6 have been investigated (P15, P42, 3M). Therefore, longitudinal sections of the humerus, as the hind limbs are not used (not mechanically loaded) by the mice, embedded in PMMA, were studied with ESEM and SAXS.

4.2.1 Analysis of the osteocyte network

The analysis of the organization of the osteocyte network in bones of NF1 mice in comparison to normal wild type mice, both strain C57BL/6, was feasible using the ESEM.

Figure 4-11 shows an overview of one representative humerus of a 3 month old wild type mouse and NF1 mouse together with enlargements of different regions of interest.

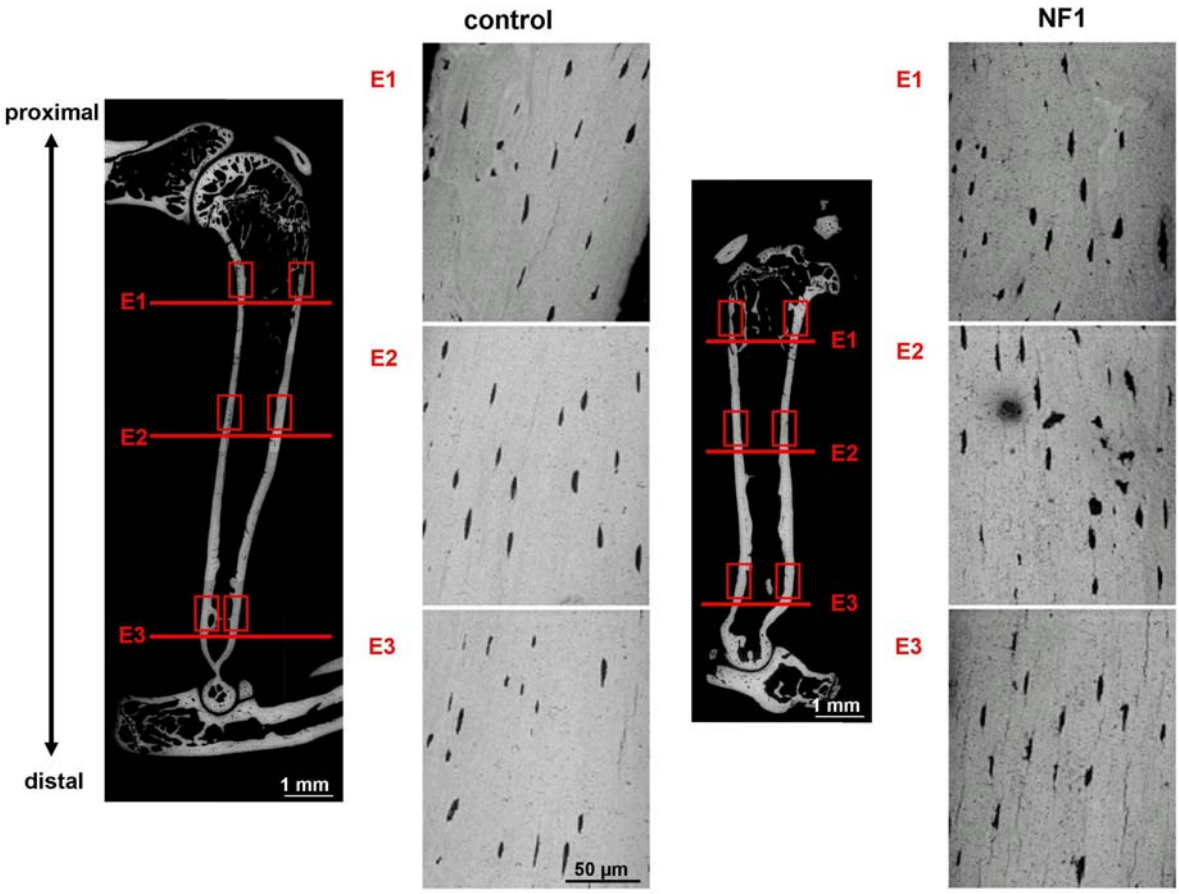

Figure 4-11: ESEM images. On the left, the overview image and 800x magnifications of one of the regions marked with the red boxes of the humerus of a wild type mouse (control) is represented. On the right, the humerus of a NF1 mouse is depicted, imaged under the same conditions as the wild type mouse bone, both 3 month old.

The investigations with the ESEM in BSE mode have been carried out on 5 samples of wild type and NF1 mice, respectively. To study the distribution and the morphology of the osteocyte lacunae in the long bones, different regions of interest have been selected. These regions of interest were located at both sides of the truncated cortex at the proximal end of the humerus (E1), close to the shoulder, in the midshaft region (E2) and at the distal end of the humerus (E3), close to the elbow. Three images per side thus six images per region have been analyzed. Comparing both sides of the truncated cortex of the humeri revealed no differences in the osteocyte lacunae. Thus, **Figure 4-11** shows only one representative image as the enlargements per region of interest. The overview images in **Figure 4-11** clearly show that the outer shape of the humerus of the NF1 mouse is altered compared to the wild type humerus. NF1 results in a bowing of the humerus. Furthermore, a smaller bone size of the humerus in the NF1 mouse can be observed in the overview images in **Figure 4-11**. The humerus of the NF1 mouse is about 20% smaller than that in the wild type mouse. Comparing the magnification images of the different regions between NF1 and wild type mice in **Figure 4-11** reveals strong differences in the morphology and the number of osteocyte lacunae, already visible by the naked eye. The osteocyte lacunae in NF1 mice

can be described as disrupted, less uniform and not that strongly arranged parallel to longitudinal axis of the bone compared to the wild type mice. The results of the quantitative analysis are shown in **Table 4-1**.

parameter	E1 – wt	E1 – NF1	E2 – wt	E2 – NF1	E3 – wt	E3 – NF1
Osteocyte area per bone (%)	2.398 ±0.797	3.506** ±0.975	1.897 ±0.519	3.4** ±0.945	1.891 ±0.492	3.042** ±1.248
Osteocyte number	21.6 ±7.7	26.7** ±11.4	16.4 ±3.6	22.4** ±6.5	21.6** ±5.5	22.4 ±6.1
Osteocyte ellipse longest axis [µm]	5.169 ±2.213	4.507** ±2.489	5.709 ±2.023	6.329** ±2.616	5.142 ±1.925	5.934** ±2.383
Osteocyte ellipse shortest axis [µm]	1.608 ±0.672	1.658** ±0.683	1.54 ±0.581	1.674** ±0.603	1.354 ±0.484	1.612** ±0.583

Table 4-1: Quantitative analysis of the osteocyte lacunae in wild type (wt) and NF1 mice. Statistical significance is calculated by a t-test, with ** representing $p \leq 0.01$, where NF1 is compared with wild type mice. 5 animals per group are included in the analysis.

In the proximal region (E1) the analysis of the osteocyte lacunae in the NF1 mice reveals a significant higher osteocyte area per bone (%), a significant higher osteocyte number and a lower aspect ratio (osteocyte lacuna length/width), meaning shorter but thicker osteocyte lacunae in NF1 mice (see **Table 4-1**). The midshaft region (E2) shows a similar trend. Osteocyte area per bone (%) and osteocyte number are significantly higher in the humeri of NF1 mice compared to wild type mice (see **Table 4-1**). Surprisingly the osteocyte lacunae in this region are longer and thicker, thus exhibiting a little higher aspect ratio than the osteocyte lacunae in wild type bone (see **Table 4-1**). Quantitative analysis of the distal region (E3) reveals strong differences in the osteocyte lacunae between the NF1 bone and the wild type bone as well (see **Table 4-1**). The area of the osteocytes per bone (%) and osteocyte number is higher in the NF1 mice than in the wild type mice. Furthermore, the osteocyte lacunae reveal a lower aspect ratio.

Investigations of Kolanczyk et al. showed a higher porosity in the bone of NF1 mice [Kolanczyk, Kossler et al., 2007]. The presented results of this study indicate that the osteocytes may be involved in this material level defect in NF1 mice as their morphology and number is strongly altered compared to wild type mice.

4.2.2 Analysis of the mineral properties

Mineral properties in bone of wild type and NF1 mice have been investigated using SAXS. In the same measurement routine as for the studies on normal bone development, the longitudinal sections of humeri were first imaged by ESEM and in the radiography to define measuring positions along the bone cortex.

The results on the mineral arrangement in the bone determined by SAXS measurement in the midshaft region of humeri of wild type and NF1 mice at three different postnatal developmental stages are shown in **Figure 4-12**.

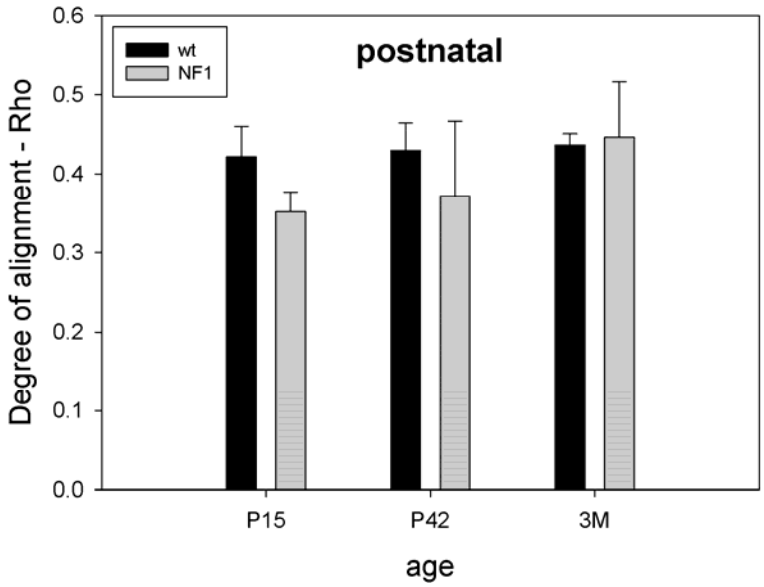

Figure 4-12: Degree of mineral crystal alignment (mean ± standard deviation), Rho-parameter, as a function of age. Laboratory SAXS data are shown for wild type mice (wt) in black and NF1 mice (NF1) in gray. All developmental stages are postnatal stages (after birth). Note that there is no significant difference between wild type and NF1 in the mineral particle arrangement.

Figure 4-12 shows preliminary SAXS results as there was only one sample per time point measured. Thus, this graph can be used to get an impression of the mineral arrangement in wild type and NF1 humeri but statistical relevance is missing. These initial measurements show no significant differences in the mean mineral particle arrangement, the Rho-parameter, between NF1 and wild type mice bone. The Rho values of wild type and NF1 bone are very similar, namely 0.42 in wild type and 0.35 in NF1 mouse at P15, 0.43 for wild type and 0.37 for NF1 mice at P42 and 0.44 in wild type and 0.45 in NF1 mouse at 3 month. These results show a little increase of Rho with age as shown for normal bone development in tibiae.

The mean mineral particle thickness in dependency on age is represented in **Figure 4-13**. Only one sample per time point was measured in these experiments.

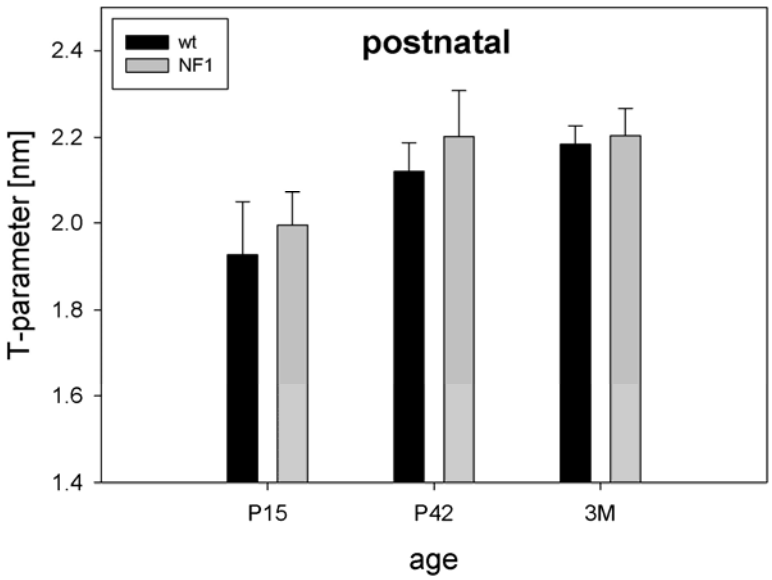

Figure 4-13: Mineral particle thickness (mean value ± standard deviation), T-parameter, grouped by age. Laboratory SAXS data are shown for wild type mice (wt) in black and NF1 mice (NF1) in gray. All developmental stages are postnatal stages (after birth). Note that there is no significant difference between wild type and NF1. There is a little increase of the T-parameter with age observable.

The comparison between wild type mice and NF1 mice revealed similar values for the T-parameter as well. In wild type mice 1.9 nm and 2 nm in NF1 mice at P15, 2.1 nm in wild type and 2.2 nm in NF1 mice at P42 and 2.2 nm for both at 3 month. Furthermore, these results show that there is an increase of the T-parameter with age, consistent with the findings for natural bone development.

These initial SAXS measurements already indicate that there is no characteristic difference in the mineral particle arrangement and the mineral particle thickness between wild type and NF1 bone. Thus, the mineral level itself seems not be affected by the Nf1 knockout. It can be rather assumed that there is a matrix or cell defect present in NF1 mice leading to the bone phenotype.

In the following section bone development during healing induced by polymer composite scaffolds implanted in porcine calvaria for 2 years is represented. Tissue engineered bone formed in scaffolds is compared to native bone in the surrounding calvaria.

4.3 Artificially induced bone development

The following section deals with the analysis of tissue engineered bone formed in polycaprolactone-tricalcium phosphate (PCL-TCP) scaffolds to study artificially induced bone development. Bone regeneration within degradable composite scaffolds, as the artificially induced bone formation, as well as the native bone surrounding the scaffold, as

the natural bone development, were investigated and both types of bone formation have been compared. Therefore, sections cut through the center of the embedded PCL-TCP scaffolds, implanted in pig for 2 years, have been used for histological investigations and studies with the ESEM and SAXS.

4.3.1 Qualitative analysis of the bone

By using histological staining of sections of the explanted scaffold and the surrounding bone, photographed with a light microscope and the imaging of the samples with an ESEM in BSE mode, the tissue formed in the scaffolds after 2 years implantation could be investigated qualitatively.

Figure 4-14 shows light microscopy images of one representative scaffold with the adjacent calvaria, naturally (see **Figure 4-14**, a) and after histological staining using MacNeal's stain (see **Figure 4-14**, b and c). The presented PCL-TCP scaffold was implanted in combination with BMSCs.

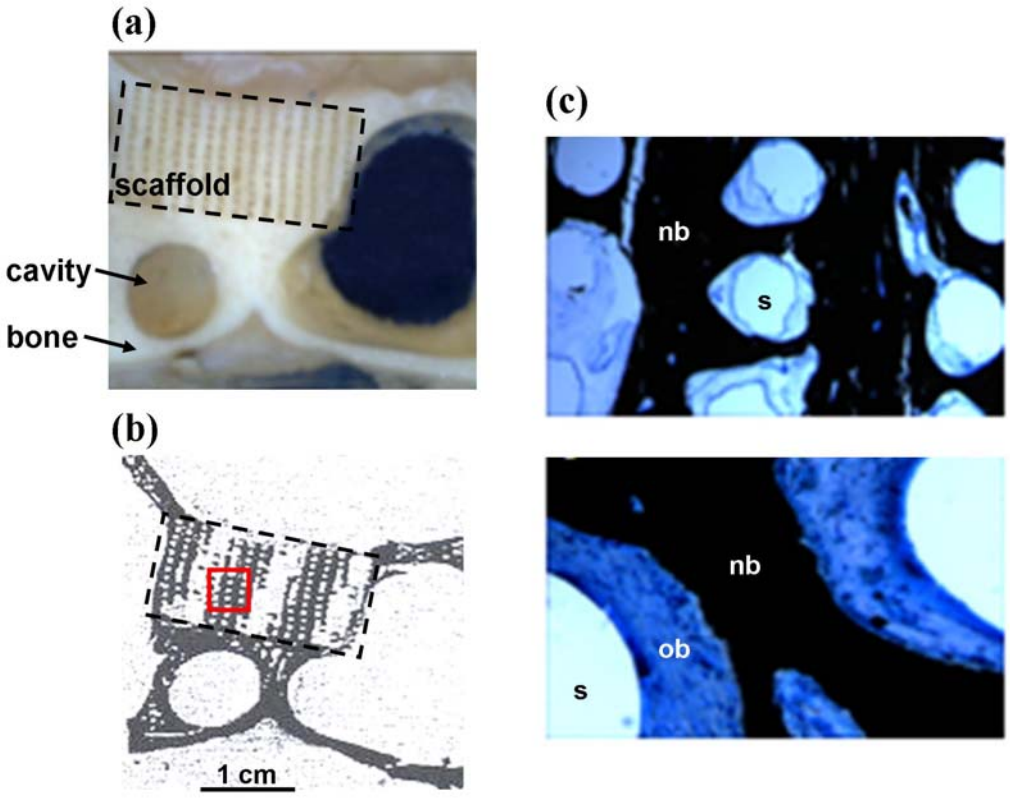

Figure 4-14: (a) Light microscopy image of the explanted PCL-TCP scaffold (marked by the dashed line), containing BMSCs, and the surrounding bone, (b) Overview of the mineralized areas in the sample after MacNeal's staining, showing mineralized tissue in black (scaffold area – dashed line), (c) Higher magnification of MacNeal's stained sections, showing the region marked with the red box in (b), s – marks the scaffold strut, nb – highlights the newly formed bone stained in black, ob – marks the osteoblasts, representing unmineralized regions/osteoid in blue.

The PCL-TCP scaffold is still present after 2 years implantation (see **Figure 4-14**, a) and the pores of the scaffold are filled with tissue. Using MacNeal's stain the tissue formed in the scaffold can be identified as mineralized tissue, stained in black (see **Figure 4-14**, b-c), and low amounts of unmineralized bone, called osteoid, stained in purple (see **Figure 4-14**, c). The circular areas in the micrographs (see **Figure 4-14**, c – marked with s) represent the positions where the scaffold struts have been before, they have been dissolved during the histological processing. Around the struts of the scaffolds there are osteoblasts forming a thin layer of tissue, which is unmineralized bone tissue, called osteoid (see **Figure 4-14**, c – marked with ob). These results are found for several samples thereby clearly demonstrating that the PCL-TCP scaffolds are filled with bone tissue after 2 years implantation. Moreover, bone formation occurs in the PCL-TCP scaffolds with BMSCs and in the PCL-TCP scaffolds alone.

Thus, for effective bone regeneration it seems to be important that the degradation time of the scaffolds fits into the range of bone formation. Since not all scaffolds are completely filled with bone tissue, it has to remain longer than the 2 years in this long-term study. As the scaffold material needs 4 to 5 years to fully resorb, these scaffolds seem to be a suitable choice supporting bone regeneration of the critical sized defect area.

To further investigate the mineralized tissue formed in the scaffolds, ESEM images in BSE mode have been taken. The electron micrographs of the same sample presented for the histological investigations, containing a PCL-TCP scaffold implanted with BMSCs, are shown in **Figure 4-15**.

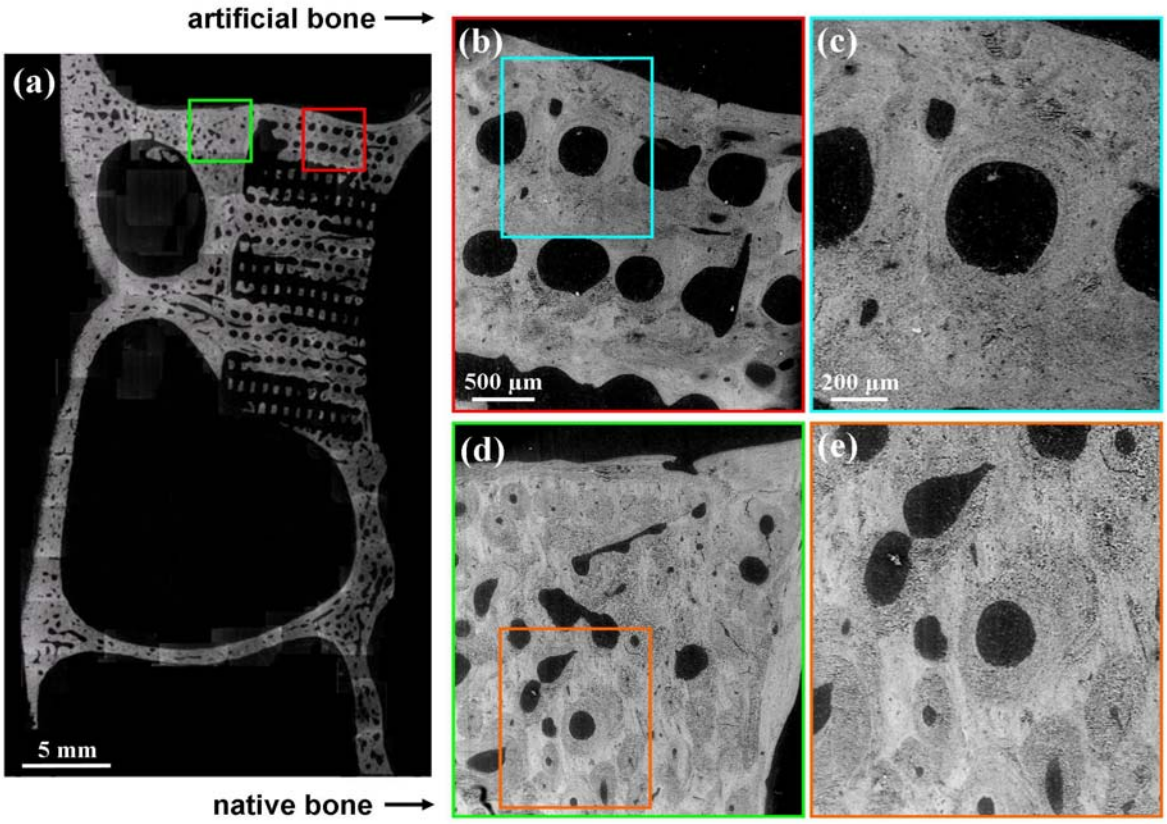

Figure 4-15: Comparison of tissue engineered bone (red box) with native calvarial bone (green box) in the vicinity of the implant. (a) Overview image after assembly of single images of 35 x magnification, (b) and (c) enlargements of the regions in the tissue engineered bone marked with a red box in (a) and with a cyan box in (b), respectively. The holes correspond to the location of struts in the implanted scaffold. (d) and (e) enlargements of regions of normal bone next to the implant marked with a green box in (a) and with a orange box in (d), respectively.

The ESEM images of the scaffold explanted with the surrounding skull indicate that the bone tissue in the scaffold has been formed around and in-between the struts of the scaffold (see **Figure 4-15**, a-c), as reinforced using histological assessment. It becomes obvious that the regions of the native calvarial bone show some porosity, which may correspond to marrow space or blood vessels surrounded by bone material often exhibiting a lower mineral content, represented by dark gray (see **Figure 4-15**, d and e). This could indicate high remodeling activity, since lower mineral content usually means younger bone. Interestingly, the bone material surrounding the struts of the implanted PCL-TCP scaffold does not show a lower mineral density (see **Figure 4-15**, b and c). These results can be observed for different areas in two samples (not shown).

An explanation for the difference in the mineral density around the pores in the calvarial bone and around the struts of the scaffolds could be that the pores in the native calvaria gradually decrease by new bone formation at the inside of the pore, whereas tissue engineered bone starts to grow on the surface of the struts of the scaffold and expands from

there. As a consequence, the bone material around pore spaces in the skull is the youngest, whereas around the struts it is the oldest compared to the surroundings.

Besides the comparison of the bone tissue in the calvaria and the tissue engineered bone, the bone formation in a PCL-TCP scaffold containing BMSCs as well as in a scaffold without adding BMSCs has been investigated. **Figure 4-16** shows the ESEM image of a sample containing a PCL-TCP scaffold, a PCL-TCP scaffold plus BMSCs and the surrounding calvaria in the same animal.

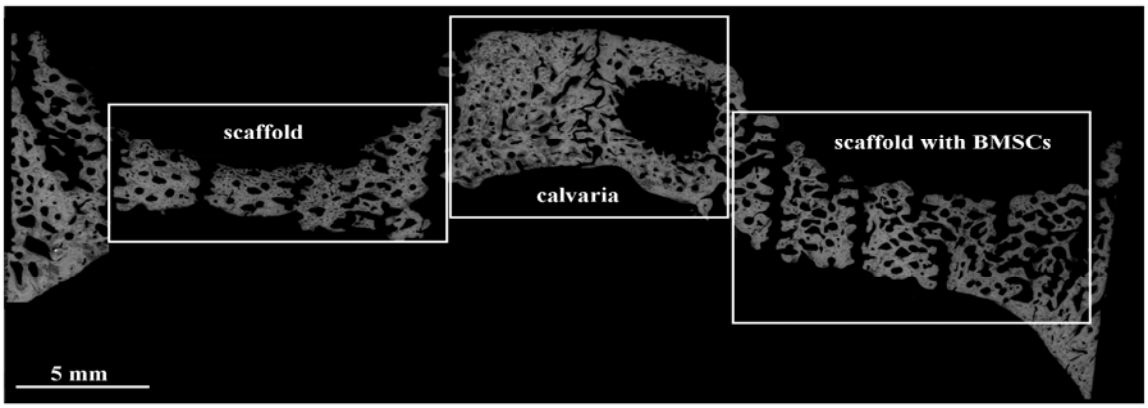

Figure 4-16: ESEM image showing a sample containing a PCL-TCP scaffold (left), a PCL-TCP scaffold plus BMSCs (right) and calvarial bone (middle) in the same animal. Note that the higher amount of mineral is formed in the scaffold with BMSCs.

The implantation of both the PCL-TCP scaffold alone and with BMSCs leads to good results in bone regeneration depicted by the mineralized areas within both of the scaffolds (see **Figure 4-16**). However, there appears higher bone formation in the scaffold plus BMSCs, demonstrated by the larger mineralized areas in the ESEM image (see **Figure 4-16**, right). Thus, the addition of BMSCs shortly prior the implantation of the PCL-TCP scaffold seems to support the bone formation in the scaffold. At the QUT μ-computer-tomography-experiments have been performed to quantify the bone formation in the scaffolds. They show higher bone volume fraction within the PCL-TCP scaffold implanted with BMSCs (48%) compared to the scaffold alone (32%).

These results indicate that the scaffold only is not enough to support tissue formation to optimal extent, as the scaffold with cells clearly reveals increased bone regeneration. Thus, the combination of a slowly degradable scaffold with BMSCs seems to be a good approach for the regeneration of bone tissue in critical sized defects in a large animal model.

Additionally to the investigation of the μm-scale, including the mineral deposition and distribution, the analysis of the nm-scale, determined by SAXS, including mineral particle properties, is described in the following.

4.3.2 Analysis of the mineral properties

Besides the tissue characterization and the analysis of the mineral distribution in the PCL-TCP scaffolds, the mineral phase was characterized concerning mineral particle thickness and mineral orientation using SAXS. Therefore, measuring positions in the tissue engineered bone as well as in the calvarial bone have been selected to analyze the mineral particles in both types of bone present in the samples, to compare artificially induced bone formation with normal bone formation directly. The results of one representative sample are summarized in **Figure 4-17**.

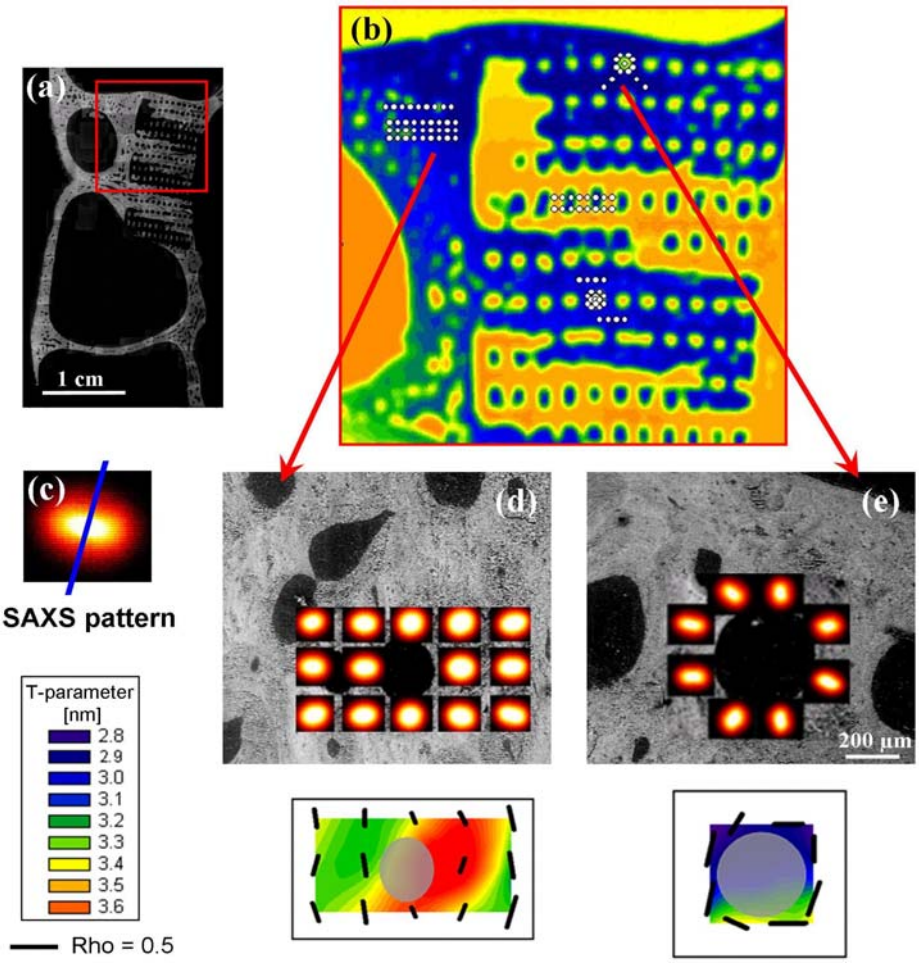

Figure 4-17: (a) Overview of the scaffold and the surrounding calvaria with the region of interest marked in red. (b) X-ray radiography image of the same specimen (blue areas correspond to high absorption – mineralized tissue), measuring positions are displayed by white dots. (c) SAXS patterns were collected at certain positions in the specimen. The asymmetry of the pattern is due to the alignment of the mineral particles in the volume illuminated by the X-ray beam. The blue line shows the typical orientation of the mineral platelets. (d) and (e) show SAXS patterns in the vicinity of a hole in normal bone (c) or a scaffold strut in tissue engineered bone (d). The mineral orientation and thickness are illustrated in color maps, representing the orientation of the mineral particles by the orientation of the black lines where the length demonstrates the degree of alignment of the mineral particles and the mineral thickness by differing colors (values are shown in the scale). Note that newly formed tissue is aligned parallel to the surface of the strut and the mineral particles in the tissue engineered bone exhibit lower T-parameter values than the mineral particles in normal bone.

By using ESEM images regions of interest in the sample could be defined to subsequently produce the radiography, necessary to select the positions of the SAXS measurement (see **Figure 4-17**, a, b). Morphologically similar regions around circular cavities were characterized with SAXS. The SAXS signal was measured in the calvarial bone around the pores (see **Figure 4-17**, d) and in the tissue engineered bone around the struts of the PCL-TCP scaffold with BMSCs (see **Figure 4-17**, e) and analyzed concerning the thickness and the degree of alignment of the mineral particles. The color maps (see **Figure 4-17**, d and e, right) are illustrating the mineral orientation by black lines and the degree of mineral alignment by the length of these lines, the mean mineral particle thickness is depicted by the color. **Figure 4-17** d and e show a dramatic difference in the bone ultrastructure between normal and tissue engineered bone. While the mineral particles in the calvarial bone show no preferential orientation around the pores, indicated by the SAXS pattern and illustrated in the color maps (see **Figure 4-17**, d), the mineral particles in the tissue engineered bone show a strong preferential orientation around the scaffold struts (see **Figure 4-17**, e). Already the shape of the scattering pattern indicates that the elongated mineral particles are typically aligned with the surface of the strut. Moreover, the thickness of the mineral particles in the tissue engineered bone and the normal bone is found to be different. Mineral particles in the tissue engineered bone are thinner than the mineral particles in the calvaria. The mean thickness of the mineral particles is 3.37 ± 0.16 nm near the pore (see **Figure 4-17**, d) and 3.04 ± 0.25 nm near the scaffold strut (see **Figure 4-17**, e). These results, concerning mineral arrangement and thickness in tissue engineered bone and calvarial bone, are observed for different regions corresponding to these two types of bone in two samples (only one region shown in **Figure 4-17**).

Furthermore, the bone formed in a PCL-TCP scaffold containing BMSCs and in a PCL-TCP scaffold alone has been analyzed by SAXS to investigate the influence of the addition of BMSCs on the artificially induced bone formation in the scaffolds. Therefore, implantations of a PCL-TCP scaffold plus cells and a PCL-TCP scaffold alone in a side by side critical sized defect created in the same animal have been investigated along with the surrounding calvaria to compare the tissue engineered bone again with normal bone. The results, including ESEM images, SAXS patterns and color maps, of the different regions of interest within the sample are presented in **Figure 4-18**.

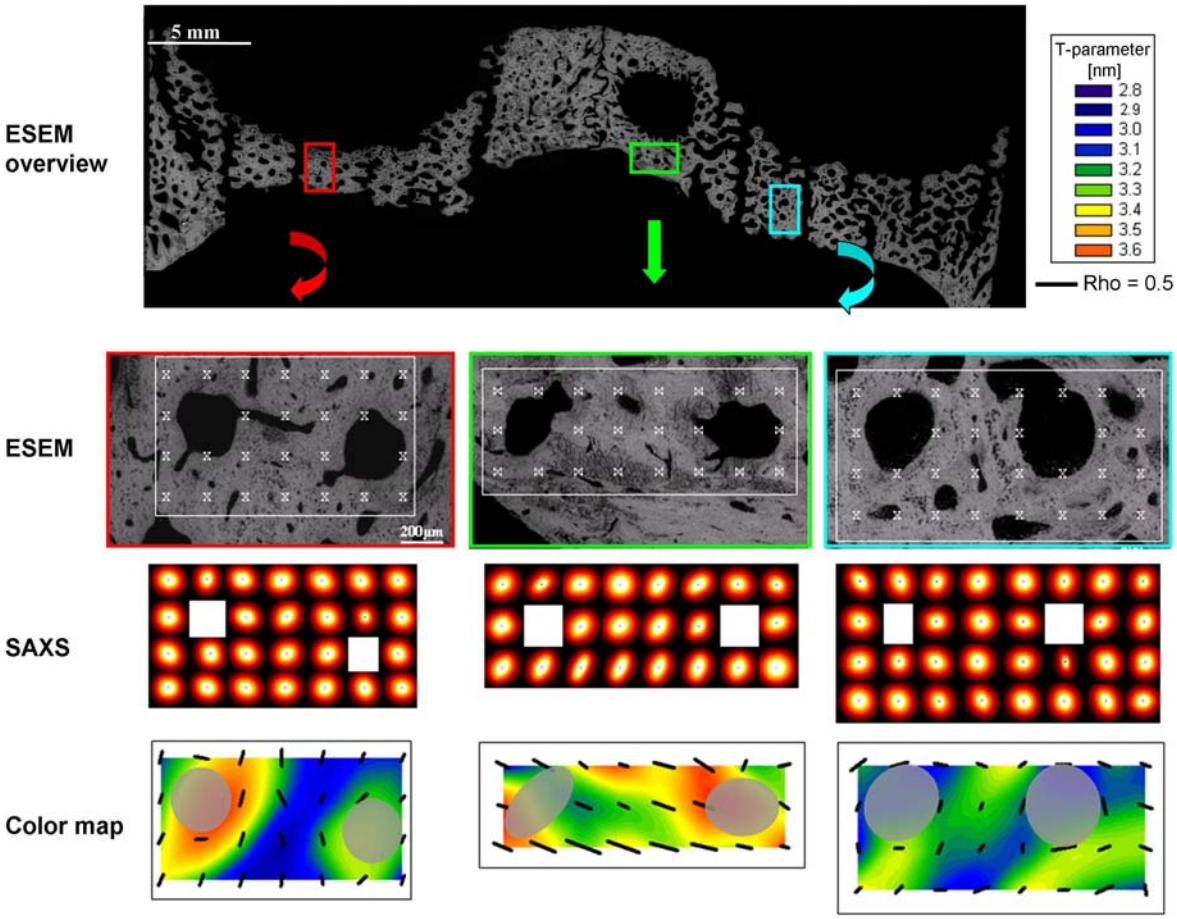

Figure 4-18 Results of an implantation of a PCL-TCP scaffold plus BMSCs (cyan box), a PCL-TCP scaffold alone (red box) and the adjoining calvaria (green box) in the same animal. The ESEM images of the three areas of interest with the measuring positions of the SAXS measurements, highlighted by white crosses, the corresponding SAXS patterns and the color maps depicting the mineral orientation and thickness are shown. Note that the mineral particles in the tissue engineered bone are highly aligned around the struts of the scaffold and thinner than the mineral particles in the calvaria.

The presentation of the results of the SAXS analysis of distinct regions in the sample in **Figure 4-18** is similar to **Figure 4-17**. The ESEM images were used to defined the regions interest to make the radiography (not shown), which is needed to select the measuring positions for the SAXS measurements (see **Figure 4-18,** white crosses). The color maps are again illustrating the mineral orientation and thickness in the region of the interest. Comparing the mineral orientation and the thickness in the tissue engineered bone in the scaffold plus BMSCs (see **Figure 4-18,** cyan box) and in the scaffold alone (see **Figure 4-18**, red box) with the calvarial bone (see **Figure 4-18**, green box) confirms the results shown before (see **Figure 4-17**). The mineral particles in the tissue engineered bone are highly aligned around the struts of the scaffold with and without cells, whereas the mineral particles in the calvarial bone are not aligned around the pores. Additionally, the mean mineral thickness depicted by the color maps indicates that the mineral particles in the tissue engineered bone are thinner than the mineral particles in the calvaria. There is no

difference in the mineral properties between bone formed in scaffold with BMSCs and bone formed in scaffolds without addition of BMSCs.

The difference in the mineral particle thickness between the calvarial and the tissue engineered bone could be due to a difference in the developmental stage of the bone investigated. The tissue engineered bone in the scaffolds is later formed, thus younger, than the calvarial bone in the skull of the pig and is hence exhibiting thinner mineral particles. The orientation around the scaffold struts is maybe explainable by the geometry of the scaffolds, which seems to guide the tissue formation. The elongated mineral crystals in calvarial bone are known to be mostly oriented within the plane of the calvaria, but with no preferential alignment within this plane [Fratzl, Fratzl-Zelman et al., 1991]. These findings are in good agreement with the observations presented in this study. The mineral particles in the tissue engineered bone show a totally different architecture. In **Figure 4-19** the different mineral arrangement is schematically illustrated.

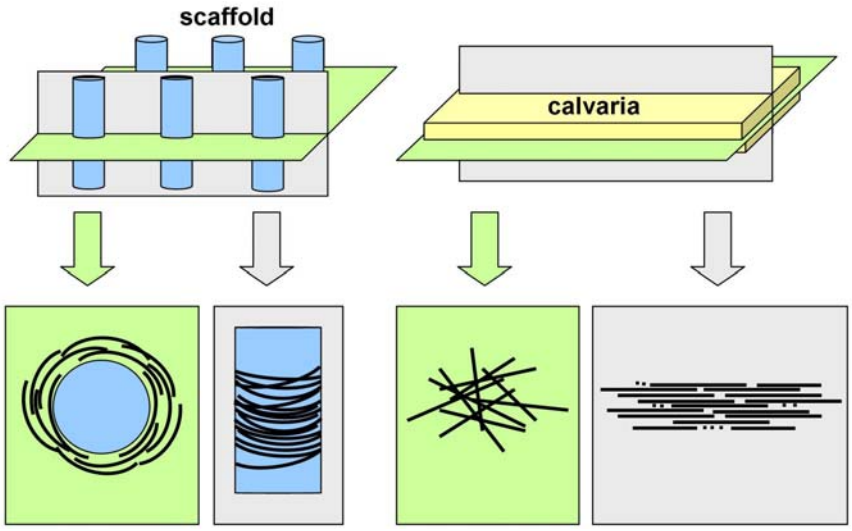

Figure 4-19: Schematic drawing of the mineral arrangement in the scaffold and the calvaria with two different planes. On the left, the scaffold architecture is schematically illustrated (top), with the planes representing a top view in green and a side view in gray. The arrangement of the elongated mineral particles is depicted by black lines for both planes (bottom). On the right, the calvarial plate is schematically drawn with the two planes, representing top and side view in green and gray, respectively (top) and the mineral arrangement by black lines (bottom). Note the dramatically different mineral arrangement in the calvaria, with mineral particles randomly oriented in the plane of the calvaria, and the tissue engineered bone, with mineral particles highly aligned around the struts of the scaffold.

The scheme demonstrates the differences in the mineral particle arrangement between the two types of bone investigated in this part of the study, tissue engineered bone and normal bone of the calvaria. Mineral particles in the calvaria, a flat bone, are arranged in the plane of the calvaria (see **Figure 4-19**, right, gray), but exhibit no preferential orientation within

the plane (see **Figure 4-19**, right, green). The arrangement of the mineral particles in the artificially induced bone formation is totally different from that in the calvaria. Mineral particles in the PCL-TCP scaffold with and without BMSCs are highly oriented around the struts, which seem to guide the bone formation (see **Figure 4-19**, left).

It is interesting that the mineral particles in the tissue engineered bone are highly oriented, thus revealing a totally different structure than the mineral particles in the calvaria. This architecture is also different from early tissue found in the callus of a fracture during the healing process, which is much less organized [Liu, Manjubala et al., 2010]. Furthermore, no indications of primary woven bone can be found in the scaffolds, possibly indicating that highly organized bone (lamellar) is directly formed on the surface of the scaffold struts.

5 Conclusion and Outlook

The main purpose of studying developing bone was to determine how mineral particles organize and grow, especially at the early stages of bone development, and with age, to get a more complete understanding of the mineralization process in mammalian systems.

In conclusion, the presented results on natural bone development in mice revealed strong differences in the shape and the arrangement of the mineral particles between fetal and postnatal bone in mice, indicating two different types of bone tissue, appearing successively and possibly coexisting in mature bone. Fetal bone tissue is characterized by (i) spotty mineralization, (ii) short but relatively thick mineral particles, and (iii) no preferred orientation of the mineral particles. Whereas postnatal bone tissue can be identified by (i) continuous mineralization, (ii) long and slender mineral particles where length and thickness increase simultaneously with age, and (iii) highly oriented mineral particles. The formation of highly ordered bone tissue seems to occur after the initial development of a less ordered bony substrate. The changes in the mineral arrangement lead to the suggestion that the environmental changes at birth seem to provide a mechanical stimulus, strongly influencing the mineral particle organization. Furthermore, the decrease of the mineral particle thickness before birth, between the two fetal stages of bone development, F16.5 and F18.5, could indicate that the earliest mineral phase formed during long bone development in mice may be a precursor phase of HA. Another hint for the theory of a precursor mineral phase is the calcium offset, meaning the presence of calcium but without HA, which could be due to calcium which is not bound in HA but maybe in a precursor phase. But it was not possible to conclude, whether this precursor mineral phase is amorphous. The presence of a calcium offset even in the postnatal bone led to the assumption that the precursor mineral phase and mature mineral particles seem to be coexistent in mature bone. To further proof these findings and to investigate possible differences concerning the degree of crystallinity in the mineral particles, Raman experiments and high resolution cryo SEM measurements are recommended. The present data can be used as baseline data on the mineral particle properties during natural bone development. Thus, the influence on the mineral level due to for instance genetically modifications can be investigated. Furthermore, bone development and fracture healing in the same animal model can be compared on that level of hierarchy.

The motivation of investigating bone development in NF1 mice was the aim to determine the hierarchical level of influence of NF1 leading to the characteristic bone phenotype. Due to differences in the porosity and the mechanical properties between bones of NF1 mice and normal mice [Kolanczyk, Kossler et al., 2007], it was interesting to investigate

whether an alteration of the mineral properties is attributing to these changes. The preliminary investigations on the mineral properties of bones of NF1 mice, described in the present doctoral thesis, revealed no differences in the mineral particle properties between NF1 bones and normal bones. These results lead to the assumption that the mineral particle level is not influenced by the knockout of the Nf1 gene and is thus not the reason for the bone phenotype of NF1. However, the investigations in the next higher level of hierarchy, the quantification of the osteocyte lacunae in NF1 and normal bone, clearly pointed out that there are strong morphological differences. The NF1 bone showed less uniform, frayed and bigger osteocyte lacunae compared to the normal mice bone. These results could indicate that the osteocytes are concerned with the bone defect in NF1 mice. Future studies in this field are necessary to address an array of open questions. It is still not fully understood, where the basis of the NF1 bone defects is located, which is affecting specific skeletal regions, such as the tibia or humerus.

Additionally, the present doctoral thesis focuses on the development of tissue engineered bone during healing formed in resorbable composite scaffolds implanted in porcine calvaria compared to native calvaria, to understand the bone remodeling and regeneration guided by a scaffold. The bone formed in a degradable scaffold to close a critical sized defect, was examined to improve the knowledge on how bone is remodeled and regenerated in a tissue engineered construct over a long period of time. For this purpose, it is important to find out to what extent tissue engineered bone is comparable to native bone. The comparison of the tissue engineered bone with native calvaria demonstrated strong differences between these two types of bone. Whereas the mineral particles in the calvaria show no preferential orientation around cavities, the mineral particles in the tissue engineered bone are strongly oriented around the struts of the 3D scaffold. These results lead to the suggestion that the artificially induced bone development is guided by the structure of the scaffold. The bone was formed around the struts. The present study gives inside in how bone is formed in scaffolds over a long period of time, which is of special interest for developing biomaterials for bone tissue engineering. It could be demonstrated that a 3D scaffold architecture combined with a slow degradation of the composite material leads to the long-term regeneration and remodeling of functional and highly organized bone. Furthermore, it could be reported that a scaffold alone is not enough to support tissue regeneration of bone to optimal extent. The addition of BMSCs was strongly increasing the amount of regenerated bone in the scaffold. As this is the first long term study on calvarial bone regeneration in large animals, there are more studies needed to proof the interesting findings. These investigations are crucial for future development and optimization of tissue engineered bone constructs.

6 References

Aichmayer B. and Fratzl P. (2010). "Vielseitige Biominerale." Physik Journal 9: 33-38.

Akhter M. P., Fan Z., et al. (2004). "Bone intrinsic material properties in three inbred mouse strains." Calcif Tissue Int 75(5): 416-20.

Alberts B. B., D.; Lewis, J.; Raff, M.; Roberts, K.; Watson J.D., Ed. (1995). Molekularbiologie der Zelle, VCH.

Baron R. (1993). Anatomy and ultrastructure of bone. Primer on the metabolic bone diseases and disorders of mineral metabolism, Second edition, Raven Press {a}**:** 3-9.

Barret C. S., Cohen J. B., et al. (1986). Advances in X-ray analysis. New York, Plenum Press.

Bartl R. "Die Knochenbiopsie in der klinischen Osteologie." http://www.roche.com/pages/facetten/11/oestdef.htm Retrieved December 1st 2010.

Beniash E., Metzler R. A., et al. (2009). "Transient amorphous calcium phosphate in forming enamel." J Struct Biol 166(2): 133-43.

Betts F., Blumenthal N. C., et al. (1981). "Bone Mineralization." Journal of Crystal Growth 53(1): 63-73.

Bonar L. C., Lees S., et al. (1985). "Neutron diffraction studies of collagen in fully mineralized bone." J Mol Biol 181(2): 265-70.

Bonar L. C., Roufosse A. H., et al. (1983). "X-Ray-Diffraction Studies of the Crystallinity of Bone-Mineral in Newly Synthesized and Density Fractionated Bone." Calcified Tissue International 35(2): 202-209.

Boskey A. L. (1997). "Amorphous calcium phosphate: The contention of bone." Journal of Dental Research 76(8): 1433-1436.

Boskey A. L. and Posner A. S. (1984). "Bone-Structure, Composition, and Mineralization." Orthopedic Clinics of North America 15(4): 597-612.

Brodt M. D., Ellis C. B., et al. (1999). "Growing C57Bl/6 mice increase whole bone mechanical properties by increasing geometric and material properties." J Bone Miner Res 14(12): 2159-66.

Brown W. E. (1962). "Crystal structure of octacalcium phosphate " Nature (London) 196: 1048-1055.

Burger E. H. and Klein-Nulend J. (1999). "Mechanotransduction in bone - role of the lacuno-canalicular network." Faseb Journal 13: S101-S112.

Burger E. H., Klein-Nulend J., et al. (1991). "Modulation of osteogenesis in fetal bone rudiments by mechanical stress in vitro." J Biomech 24 Suppl 1: 101-9.

Cashman K. D. (2002). "Calcium intake, calcium bioavailability and bone health." British Journal of Nutrition 87: S169-S177.

Chow L. C. (2001). Calcium phosphate cements. Monographs in Oral Science. Octacalcium phosphate, S. Karger Publishers Inc.; S. Karger AG**:** 148-163.

Crane N. J., Popescu V., et al. (2006). "Raman spectroscopic evidence for octacalcium phosphate and other transient mineral species deposited during intramembranous mineralization." Bone 39(3): 434-42.

Currey J. D. (2002). Bones : structure and mechanics. Princeton [N.J.], Princeton University Press.

Danilchenko S. N., Kukharenko O. G., et al. (2002). "Determination of the bone mineral crystallite size and lattice strain from diffraction line broadening." Crystal Research and Technology 37(11): 1234-1240.

Finean J. B. and Engstrom A. (1953). "The Low-Angle Scatter of X-Rays from Bone Tissue." Biochimica Et Biophysica Acta 11(2): 178-189.

Forriol F. and Shapiro F. (2005). "Bone development - Interaction of molecular components and biophysical forces." Clinical Orthopaedics and Related Research(432): 14-33.

Fratzl P. (2008). Collagen: Structure and mechanics, an introduction. Collagen: Structure and Mechanics, Springer**:** 1-13.

Fratzl P., Fratzl-Zelman N., et al. (1991). "Nucleation and growth of mineral crystals in bone studied by small-angle X-ray scattering." Calcif Tissue Int 48(6): 407-13.

Fratzl P., Groschner M., et al. (1992). "Mineral Crystals in Calcified Tissues - a Comparative-Study by Saxs." Journal of Bone and Mineral Research 7(3): 329-334.

Fratzl P., Gupta H. S., et al. (2004). "Structure and mechanical quality of the collagen-mineral nano-composite in bone." Journal of Materials Chemistry 14(14): 2115-2123.

Fratzl P., Schreiber S., et al. (1996). "Characterization of bone mineral crystals in horse radius by small-angle X-ray scattering." Calcif Tissue Int 58(5): 341-6.

Fratzl P. and Weinkamer R. (2007). "Nature's hierarchical materials." Progress in Materials Science 52(8): 1263-1334.

Freemont A. J. (1993). "Basic Bone Cell Biology." International Journal of Experimental Pathology 74(4): 411-416.

Frost H. M. (1987). "Bone Mass and the Mechanostat - a Proposal." Anatomical Record 219(1): 1-9.

Fuller K., Gallagher A. C., et al. (1991). "Osteoclast Resorption - Stimulating Activity Is Associated with the Osteoblast Cell-Surface and or the Extracellular-Matrix." Biochemical and Biophysical Research Communications 181(1): 67-73.

Glatter O. and Kratky O. (1982). Small angle x-ray scattering. London, Academic Press Inc.

Glimcher M. J. (1984). "Recent Studies of the Mineral Phase in Bone and Its Possible Linkage to the Organic Matrix by Protein-Bound Phosphate Bonds." Philosophical Transactions of the Royal Society of London Series B-Biological Sciences 304(1121): 479-508.

Gower L. B. and Odom D. J. (2000). "Deposition of calcium carbonate films by a polymer-induced liquid-precursor (PILP) process." Journal of Crystal Growth 210(4): 719-734.

Grabner B., Landis W. J., et al. (2001). "Age- and genotype-dependence of bone material properties in the osteogenesis imperfecta murine model (oim)." Bone 29(5): 453-7.

Gronthos S., Zannettino A. C. W., et al. (2003). "Molecular and cellular characterisation of highly purified stromal stem cells derived from human bone marrow." Journal of Cell Science 116(9): 1827-1835.

Gross T. S., Poliachik S. L., et al. (2010). "The effect of muscle dysfunction on bone mass and morphology." Journal of Musculoskeletal & Neuronal Interactions 10(1): 25-34.

Grynpas M. D. (2007). "Transient precursor strategy or very small biological apatite crystals?" Bone 41(2): 162-164.

Gupta H. S., Schratter S., et al. (2005). "Two different correlations between nanoindentation modulus and mineral content in the bone-cartilage interface." J Struct Biol 149(2): 138-48.

Hammersley A. P. (1997). Fit2d: An Introduction and Overview. internal report, ESRF.

Hill P. (1998). "Bone remodelling." British Journal of Orthodontics 25: 101-107.

Hodge A. J. (1989). "Molecular models illustrating the possible distributions of 'holes' in simple systematically staggered arrays of type I collagen molecules in native-type fibrils." Connect Tissue Res 21(1-4): 137-47.

Hodge A. J. and Petruska J. A. (1963). Recent studies with the electron microscope on ordered aggregates of the tropocollagen macromolecule. G. N. Ramachandran,

Editor. Aspects of Protein Structure. Proceedings of a Symposium, Academic Press, Inc.**:** p. 289-300.

Hutmacher D., Kirsch A., et al. (1998). Processing and fabrication of bioresorbable implants and devices - State of the art and future perspectives. Processing and Fabrication of Advanced Materials Vi, Vols 1 & 2. K. A. Khor, T. S. Srivatsan and J. J. Moore. London, Iom Communications Ltd**:** 1645-1660.

Hutmacher D. W. (2000). "Scaffolds in tissue engineering bone and cartilage." Biomaterials 21(24): 2529-2543.

Jaschouz D., Paris O., et al. (2003). "Pole figure analysis of mineral nanoparticle orientation in individual trabecula of human vertebral bone." Journal of Applied Crystallography 36: 494-498.

Karsenty G. (2003). "The complexities of skeletal biology." Nature 423(6937): 316-318.

Klug H. P. and Alexander L. E. (1974). X-ray diffraction procedures for polycrystallite and amorphous materials. New York, Wiley.

Kolanczyk M., Kossler N., et al. (2007). "Multiple roles for neurofibromin in skeletal development and growth." Hum Mol Genet 16(8): 874-86.

Kolanczyk M., Kuhnisch J., et al. (2008). "Modelling neurofibromatosis type 1 tibial dysplasia and its treatment with lovastatin." BMC Med 6: 21.

Landis W. J. (1995). "The strength of a calcified tissue depends in part on the molecular structure and organization of its constituent mineral crystals in their organic matrix." Bone 16(5): 533-44.

Landis W. J. and Glimcher M. J. (1978). "Electron-Diffraction and Electron-Probe Microanalysis of Mineral Phase of Bone Tissue Prepared by Anhydrous Techniques." Journal of Ultrastructure Research 63(2): 188-223.

Landis W. J., Hodgens K. J., et al. (1996). "Structural relations between collagen and mineral in bone as determined by high voltage electron microscopic tomography." Microscopy Research and Technique 33(2): 192-202.

Landis W. J., Song M. J., et al. (1993). "Mineral and Organic Matrix Interaction in Normally Calcifying Tendon Visualized in 3 Dimensions by High-Voltage Electron-Microscopic Tomography and Graphic Image-Reconstruction." Journal of Structural Biology 110(1): 39-54.

Langer R. and Vacanti J. P. (1993). "Tissue Engineering." Science 260(5110): 920-926.

Liu Y. F., Manjubala I., et al. (2010). "Size and Habit of Mineral Particles in Bone and Mineralized Callus During Bone Healing in Sheep." Journal of Bone and Mineral Research 25(9): 2029-2038.

Lowenstam H. A. and Weiner S. (1985). "Transformation of Amorphous Calcium-Phosphate to Crystalline Dahllite in the Radular Teeth of Chitons." Science 227(4682): 51-53.

Lowenstam H. A. and Weiner S. (1989). On biomineralization, Oxford University Press, New York & Oxford**:** i-ix, 1-324.

Lutz M. and Knaus P. (2002). "Integration of the TGF-beta pathway into the cellular signalling network." Cellular Signalling 14(12): 977-988.

Mahamid J., Aichmayer B., et al. (2010). "Mapping amorphous calcium phosphate transformation into crystalline mineral from the cell to the bone in zebrafish fin rays." Proceedings of the National Academy of Sciences of the United States of America 107(14): 6316-6321.

Mahamid J., Sharir A., et al. (2008). "Amorphous calcium phosphate is a major component of the forming fin bones of zebrafish: Indications for an amorphous precursor phase." Proceedings of the National Academy of Sciences of the United States of America 105(35): 12748-12753.

Mann S. (2001). Biomineralization - Principles and Concepts in Bioinorganic Materials Chemistry, Oxford University Press.

Meikle M. C., Bord S., et al. (1992). "Human Osteoblasts in Culture Synthesize Collagenase and Other Matrix Metalloproteinases in Response to Osteotropic Hormones and Cytokines." Journal of Cell Science 103: 1093-1099.

Miller A. (1984). "Collagen - the Organic Matrix of Bone." Philosophical Transactions of the Royal Society of London Series B-Biological Sciences 304(1121): 455-477.

Miller L. M., Little W., et al. (2007). "Accretion of bone quantity and quality in the developing mouse skeleton." J Bone Miner Res 22(7): 1037-45.

Nohe A., Keating E., et al. (2004). "Signal transduction of bone morphogenetic protein receptors." Cellular Signalling 16(3): 291-299.

Nudelman F., Pieterse K., et al. (2010). "The role of collagen in bone apatite formation in the presence of hydroxyapatite nucleation inhibitors." Nature Materials 9(12): 1004-1009.

Nylen M. U., Scott D. B., et al. (1960). "Mineralization of turkey leg tendon. II. Collagen-mineral relations revealed by electron and X-ray microscopy." Publ Amer Assoc Advancement Sci 64: 129-142.

Olsen B. R., Reginato A. M., et al. (2000). "Bone development." Annual Review of Cell and Developmental Biology 16: 191-220.

Olszta M. J., Cheng X. G., et al. (2007). "Bone structure and formation: A new perspective." Materials Science & Engineering R-Reports 58(3-5): 77-116.

Omelon S., Georgiou J., et al. (2009). "Control of Vertebrate Skeletal Mineralization by Polyphosphates." Plos One 4(5): 16.

Orgel J., Irving T. C., et al. (2006). "Microfibrillar structure of type I collagen in situ." Proceedings of the National Academy of Sciences of the United States of America 103(24): 9001-9005.

Paris O. and Muller M. (2003). "Scanning X-ray microdiffraction of complex materials: Diffraction geometry considerations." Nuclear Instruments & Methods in Physics Research Section B-Beam Interactions with Materials and Atoms 200: 390-396.

Paris O., Zizak I., et al. (2000). "Analysis of the hierarchical structure of biological tissues by scanning X-ray scattering using a micro-beam." Cellular and Molecular Biology 46(5): 993-1004.

Patton J. T. and Kaufman M. H. (1995). "The Timing of Ossification of the Limb Bones, and Growth-Rates of Various Long Bones of the Fore and Hind Limbs of the Prenatal and Early Postnatal Laboratory Mouse." Journal of Anatomy 186: 175-185.

Pittenger M. F., Mackay A. M., et al. (1999). "Multilineage potential of adult human mesenchymal stem cells." Science 284(5411): 143-147.

Porod G. (1951). "Die Rontgenkleinwinkelstreuung Von Dichtgepackten Kolloiden Systemen .1." Kolloid-Zeitschrift and Zeitschrift Fur Polymere 124(2): 83-114.

Price R. I., Lees S., et al. (1997). "X-ray diffraction analysis of tendon collagen at ambient and cryogenic temperatures: role of hydration." Int J Biol Macromol 20(1): 23-33.

Quarles L. D., Yohay D. A., et al. (1992). "Distinct Proliferative and Differentiated Stages of Murine Mc3t3-E1 Cells in Culture - an Invitro Model of Osteoblast Development." Journal of Bone and Mineral Research 7(6): 683-692.

Rho J. Y., Kuhn-Spearing L., et al. (1998). "Mechanical properties and the hierarchical structure of bone." Medical Engineering & Physics 20(2): 92-102.

Rinnerthaler S., Roschger P., et al. (1999). "Scanning small angle X-ray scattering analysis of human bone sections." Calcif Tissue Int 64(5): 422-9.

Roodman G. D. (1999). "Cell biology of the osteoclast." Experimental Hematology 27(8): 1229-1241.

Roschger P., Fratzl P., et al. (1998). "Validation of quantitative backscattered electron imaging for the measurement of mineral density distribution in human bone biopsies." Bone 23(4): 319-326.

Roschger P., Grabner B. M., et al. (2001). "Structural development of the mineralized tissue in the human L4 vertebral body." J Struct Biol 136(2): 126-36.

Ruff C., Holt B., et al. (2006). "Who's afraid of the big bad wolff? "Wolff is law" and bone functional adaptation." American Journal of Physical Anthropology 129(4): 484-498.

Schindeler A. and Little D. G. (2008). "Recent insights into bone development, homeostasis, and repair in type 1 neurofibromatosis (NFI)." Bone 42(4): 616-622.

SEER. "Introduction to the skeletal system." http://training.seer.cancer.gov/anatomy/skeletal/. Retrieved December 8th, 2010.

Shapiro F. (2008). "Bone development and its relation to fracture repair. The role of mesenchymal osteoblasts and surface osteoblasts." Eur Cell Mater 15: 53-76.

Stevens M. M. (2008). "Biomaterials for bone tissue engineering." Materials Today 11(5): 18-25.

Stevens M. M. and Khademhosseini A. (2010). "Emerging materials for tissue engineering and regenerative medicine: themed issue for Journal of Materials Chemistry and Soft Matter." Journal of Materials Chemistry 20(40): 8729-8729.

Tanck E., Van Donkelaar C. C., et al. (2004). "The mechanical consequences of mineralization in embryonic bone." Bone 35(1): 186-90.

Termine J. D. and Posner A. S. (1967). "Amorphous/crystalline interrelationships in bone material." Calcified Tissue Res 1((1)): 8-23.

Termine J. D. and Robey P. G. (1996). Bone matrix proteins and the mineralization process. Primer on the metabolic bone diseases and disorders of mineral metabolism, Third edition, Lippincott-Raven Publishers {a}**:** 24-28.

Tesch W., Vandenbos T., et al. (2003). "Orientation of mineral crystallites and mineral density during skeletal development in mice deficient in tissue nonspecific alkaline phosphatase." J Bone Miner Res 18(1): 117-25.

Traub W., Arad T., et al. (1992). "Growth of Mineral Crystals in Turkey Tendon Collagen-Fibers." Connective Tissue Research 28(1-2): 99-111.

Tuli R., Tuli S., et al. (2003). "Characterization of multipotential mesenchymal progenitor cells derived from human trabecular bone." Stem Cells 21(6): 681-693.

Veis A. (2003). "Amelogenin gene splice products: potential signaling molecules." Cellular and Molecular Life Sciences 60(1): 38-55.

Walker G. A. (2002). Common statistical methods for clinical research with SAS examples. Cary, NC, SAS institute inc.

Wang L. J. and Nancollas G. H. (2008). "Calcium Orthophosphates: Crystallization and Dissolution." Chemical Reviews 108(11): 4628-4669.

Weiner S. (2006). "Transient precursor strategy in mineral formation of bone." Bone 39(3): 431-433.

Weiner S. and Dove P. M. (2003). An overview of biomineralization processes and the problem of the vital effect. Biomineralization. P. M. Dove, J. J. DeYoreo and S. Weiner. Washington, Mineralogical Soc America. 54**:** 1-29.

Weiner S. and Traub W. (1986). "Organization of Hydroxyapatite Crystals within Collagen Fibrils." Febs Letters 206(2): 262-266.

Weiner S. and Traub W. (1992). "Bone-Structure - from Angstroms to Microns." Faseb Journal 6(3): 879-885.

Weiner S. and Wagner H. D. (1998). "The material bone: Structure mechanical function relations." Annual Review of Materials Science 28: 271-298.

Weiss I. M., Tuross N., et al. (2002). "Mollusc larval shell formation: Amorphous calcium carbonate is a precursor phase for aragonite." Journal of Experimental Zoology 293(5): 478-491.

Woodruff M. A. and Hutmacher D. W. (2010). "The return of a forgotten polymer-Polycaprolactone in the 21st century." Progress in Polymer Science 35(10): 1217-1256.

Wu X. H., Estwick S. A., et al. (2006). "Neurofibromin plays a critical role in modulating osteoblast differentiation of mesenchymal stem/progenitor cells." Human Molecular Genetics 15(19): 2837-2845.

Wuthier R. E., Rice G. S., et al. (1985). "Invitro Precipitation of Calcium-Phosphate under Intracellular Conditions - Formation of Brushite from an Amorphous Precursor in the Absence of Atp." Calcified Tissue International 37(4): 401-410.

Yasuda H., Shima N., et al. (1998). "Identity of osteoclastogenesis inhibitory factor (OCIF) and osteoprotegerin (OPG): A mechanism by which OPG/OCIF inhibits osteoclastogenesis in vitro." Endocrinology 139(3): 1329-1337.

Zander T., Li C., et al. (2010). Evaluation of X-ray scattering data sets, collected with a 2-D detector. manuscript.

Zoetis T., Tassinari M. S., et al. (2003). "Species comparison of postnatal bone growth and development." Birth Defects Research Part B-Developmental and Reproductive Toxicology 68(2): 86-110.

7 Acknowledgements

Special thanks go to my doctoral supervisor PETER FRATZL, head of the Biomaterials department at the Max Planck Institute of Colloids and Interfaces (MPIKG, Potsdam), for giving me the opportunity to work for my thesis in his group and to use the excellent research facilities. Furthermore, I highly appreciate that he always found the time for inspiring and supporting discussions.

I am very grateful to my research group leader WOLFGANG WAGERMAIER for the excellent support, fruitful discussions and encouragement during my work on this thesis. Moreover, I want to thank MANJUBALA INDERCHAND for her encouragement and helping scientific discussions.

Big thanks go to CHENGHAO LI for expert advice concerning beam line experiments and strong support in BESSY data evaluation.

I want to thank Prof. Dr. PETRA KNAUS (FU, Berlin) for scientific support and feedback on the work of this thesis and for taking over the supervision of my thesis.

Huge thanks go to SUSANN WEICHOLD, INGRID ZENKE and ANNEMARIE MARTINS for their help in the lab and in sample preparation. Moreover, I want to thank KERSTIN GABBE for organizational assistance at the MPIKG.

I want to thank my collaboration partners Prof. Dr. STEFAN MUNDLOS, JIRKO KÜHNISCH, NADINE KOSSLER and Dr. MATEUSZ KOLANCZYK for fruitful discussions and expert advice on the NF1 part of this thesis and I highly appreciate the help in sample preparation for my work as well as Prof. Dr. DIETMAR HUTMACHER and Dr. MIA WOODRUFF for inspiring scientific discussions and expert advice on the bone healing part of this thesis and for providing the samples for the investigations presented in the tissue engineering part of the thesis.

Big thanks go to all members of the Biomaterials department, especially ANNA, SUSANN, FRIEDERIKE, STEFFI, MICHA, MURIEL, MARKUS, CHRISTOPH, STEPHAN, NICOLE … who offered a warm, pleasant and inspiring atmosphere, making the time at the institute very enjoyable. Thanks!

Huge thanks go to KATHARINA KRÄGE for her incessantly support and proof reading. Moreover, special thanks go to my PARENTS for their love, encouragement and patience.

8 Appendices

8.1 List of abbreviations

ACP	amorphous calcium phosphate
AgBh	silver behenate
ALP	alkaline phosphatase
ATP	adenosine triphosphate
AutoFit	SAXS/WAXD analysis software, custom made software developed at the MPIKG
BESSY	"Berliner Elektronen-Speicherring-Gesellschaft für Synchrotronstrahlung m.b.H."
BMPs	bone morphogenetic proteins
BMSCs	bone marrow stem cells
BSE	backscattered electron
DC	dark current
DMPT	N,N-Dimethyl-p-toluidine
EB	empty beam
ECM	extracellular matrix
ESEM	environmental scanning electron microscope
F	fetal
Fit2d	SAXS/WAXD analysis program, [Hammersley, 1997]
FWHM	full width at the half maximum
GAP	GTPase activating protein
GDP	guanosine diphosphate
GTP	guanosine triphosphate
GTPase	guanosine triphosphate phosphatase
HA	hydroxyapatite
L	mean length of mineral particles
LAGeSo	"Landesamt für Gesundheit und Soziales"
MAPK	mitogen-activated protein kinase
MMA	methylmethacrylate

MPIKG	Max Planck Institute of Colloids and Interfaces
MPIMG	Max Planck Institute of Molecular Genetics
MSCs	mesenchymal stem cells
NCPs	non-collagenous proteins
NF1	neurofibromatosis type 1
Nf1	gene, encoding for neurofibromin 1
OCN	osteocalcin
OCP	octacalcium phosphate
OPN	osteopontin
P	postnatal
PCL	polycaprolactone
PFA	paraformaldehyde
PMMA	polymethylmethacrylate
PILP	polymer-induced liquid precursor
QUT, IHBI	Queensland University of Technology, Institute of Health and Biomedical Innovation
Rho	degree of alignment of mineral particles
SAXS	small-angle X-ray scattering
SE	secondary electron
SEM	scanning electron microscope
SSD	solid state detector
T	mean thickness of mineral particles
TEM	transmission electron microscopy
TCP	tricalcium phosphate
TGF-β	transforming growth factor β
WAXD	wide-angle X-ray diffraction
XRF	X-ray fluorescence
1D	one-dimensional
2D	two-dimensional
3D	three-dimensional

8.2 List of publications

Conference abstracts:

Osteologie 2008, Hannover - Three-dimensional tissue formation is influenced by substrate stiffness and pore size (talk)

European calcified tissue society (ECTS) 2009, Vienna - Mineral deposition and growth during embryonal bone development in mice (poster)

Bioamorphys summer school 2009, Neuhardenberg – Mineral deposition and growth during embryonal bone development in mice (poster)

Deutsche Tagung für Forschung mit Synchrotronstrahlung, Neutronen und Ionenstrahlen an Großgeräten (SNI) 2010, Berlin – Mineral deposition and growth during bone development in mice studied by small angle X-ray scattering (poster)

Osteologie 2010, Berlin - Mineral deposition and maturation during embryonal bone development in mice (poster, talk)

Publications:

Kommareddy, K., C. Lange et al. (2010). "Two stages in three-dimensional *in vitro* growth of tissue generated by osteoblastlike cells." Biointerphases 5 (2): 45-52

Lange, C., Li C. et al. "Differences in mineral size and orientation between fetal and postnatal bone tissue in mice" in preparation

Woodruff, M., C. Lange et al. "Characteristics of tissue engineered calvarial bone after two years *in-vivo*" in preparation

8.3 Curriculum vitae

For reasons of data protection,
the curriculum vitae is not included in the online version

For reasons of data protection,
the curriculum vitae is not included in the online version

8.4 Eidesstattliche Erklärung

Potsdam, 30 Januar 2011

Hiermit versichere ich, dass ich meine Dissertation mit dem Titel “Mineral deposition and maturation during bone development“ selbständig angefertigt habe und keine anderen, als die von mir angegebenen Hilfsmittel und Quellen verwendet habe.

Ich versichere, dass ich bisher an keiner Universität, weder im In- noch im Ausland, einen Promotionsversuch unternommen habe.

Claudia Lange